Feature-based Level Set Topology Optimization and Its Multidisciplinary Applications

by

Jikai Liu

A thesis submitted in partial fulfillment of the requirements for the degree of

Doctor of Philosophy

in
Engineering Management

Department of Mechanical Engineering
University of Alberta

Abstract

When parts are designed and manufactured, considerations for their geometry, material, function, and manufacturability need to be taken into account, and it would be efficient to address all these aspects concurrently. From this perspective, topology optimization is useful and gaining the popularity, especially for complex and multidisciplinary design problems which can be difficult to solve by experience-based methods. Extensive research efforts have been reported on enhancing the problem solving capability of topology optimization, but its relationship with feature-based design is rarely explored which leads to a gap between different stages of design activities.

Therefore, the generic research problem is the limited involvement of feature technology in topology optimization. To be specific, a tedious post-treatment is mandatory to transform the freeform topological design into a geometry feature-based CAD model to support the following feature-based design activities. This issue hurdles the effective application of topology optimization and has a negative impact on the overall design efficiency and quality. In addition, the feature attached semantic information is rarely considered by the topology optimization algorithms. Because of this, some practical measures such as manufacturing time and cost cannot be optimally designed.

To fix the problems, the generic research theme is to realize the feature-based level set topology optimization. The research activities are divided into two stages: develop geometry feature-based topology optimization approaches, and then gradually involve the feature-attached semantic information in the optimization algorithms. Specifically, essence of these research activities is presented in the following paragraphs.

First, several geometry feature-based topology optimization approaches have been developed targeting at different types of design problems. To be specific, the implicit feature-based approach realizes the predefined geometry pattern in the topological design, and an application example is the constant rib thickness design of the injection molding parts. Compared to the existing methods, this implicit feature-based approach is simpler and more efficient in numerical implementation. The explicit feature based approach realizes the geometry feature based design in the explicit form, and an application example is the 2.5D machining part design. According to the literature survey result, the explicit feature insertion capability is a novel contribution. Then, the B-rep geometry-based approach facilitates the topology optimization implementation in CAD systems and this is of great engineering significance from the integration perspective.

Second, the feature-attached semantic information is gradually involved to further enhance the geometry feature-based topology optimization approaches. Taking a machining feature for example, the attached semantic information can facilitate the quantitative evaluations of the part's manufacturing processes, tooling, machining time, costs, etc. If these evaluations could be analytically expressed based on the level set function, they can be configured into the topology optimization problem under the level set framework. Then, through the proper solution, both the part's functionality and manufacturability can be designed. Apparently, the multi-stage design requirements are concurrently addressed during the early conceptual design, which definitely shortens the product development process and improves the product's profitability and competitiveness. On this basis, a new scheme - optimization-for-manufacture (OFM), is proposed, which is an extension of the conventional design-for-manufacture (DFM) for better material use efficiency and design quality for manufacture.

For the research outcome, they are summarized into six chapters. All these contributions are built based on a common methodology of level set topology optimization, and they are presented in a progressive order from pure geometry feature-based approaches to the semantic information involvement. At the end, the novel industrial applications are demonstrated.

Preface

This thesis is an original work by Jikai Liu, and the research is performed under the supervision of Dr. Yongsheng Ma and Dr. Kajsa Duke. The contents of the chapters are partially from the published/submitted papers listed as follows:

Chapter 2:

- Liu JK, Ma YS (2015) 3D level-set topology optimization: a machining feature-based approach, Structural and Multidisciplinary Optimization 52:563-582.
- Liu JK, Ma YS, A survey of manufacturing oriented topology optimization methods, Computers and Structures, submitted.
- Liu JK, Duke K, Cheng ZR, Ma YS, Automation of cyclic CAD/CAE integration, Advances in Engineering Software, submitted.

Chapter 3:

- Liu JK, Ma YS, Fu JY, Duke K (2015) A novel CACD/CAD/CAE integrated design framework for fiber-reinforced plastic parts, Advances in Engineering Software 87:13-29.

Chapter 4:

- Liu JK, Ma YS (2015) 3D level-set topology optimization: a machining feature-based approach, Structural and Multidisciplinary Optimization 52:563-582.

Chapter 5:

- Liu JK, Duke K, Cheng ZR, Ma YS, Automation of cyclic CAD/CAE integration, Advances in Engineering Software, submitted.

Chapter 6:

- Liu JK, Li L, Ma YS, Optimization-for-manufacture through level set topology optimization and single-sided curvature flow, Journal of Intelligent Manufacturing, submitted.

Chapter 7:

- Liu JK, Ma YS, Fu JY, Duke K (2015) A novel CACD/CAD/CAE integrated design framework for fiber-reinforced plastic parts, Advances in Engineering Software 87:13-29.
- Liu JK, Duke K, Ma YS, CAD-CAE associative feature-based heterogeneous object modeling, Advances in Mechanical Engineering, accepted.

Chapter 8:

- Liu JK, Ma YS, Design of pipeline opening layout through level set topology optimization, Structural and Multidisciplinary Optimization, revised.

Acknowledgements

First, I would sincerely thank my supervisors Dr. Yongsheng Ma and Dr. Kajsa Duke for their advice, expertise and support. Also, I would thank Dr. Will Tian and Dr. Samer Adeeb for their support and encouragement.

I would also like to thank my fellow PhD students for their helpful discussions and suggestions, particularly, Dr. Yanan Xie, Mr. Zhengrong Cheng, Mr. Lei Li and Mr. Junyu Fu.

My PhD study has been funded by the China Scholarship Council, Canada Pump & Power, MITACS Accelerate and NSERC Discovery programs. Their supports are gratefully acknowledged.

Also, I would thank Professor Jinyuan Tang from Central South University for his encouragement and kind suggestions.

At last, I would thank my family for always supporting and caring for my life and studies.

Publications

Papers:

(1) Liu JK, Ma YS, Fu JY, Duke K (2015), A novel CACD/CAD/CAE integrated design framework for fiber-reinforced plastic parts, Advances in Engineering Software, vol. 87, pp.13-29

(2) Liu JK, Ma YS (2015), 3D level-set topology optimization: a machining feature-based approach, Structural and Multidisciplinary Optimization, vol. 52, pp.563-582

(3) Liu JK, Duke K, Ma YS, CAD-CAE associative feature based heterogeneous object modeling, Advances in Mechanical Engineering, **accepted**.

(3) Liu JK, Ma YS, Design of pipeline opening layout through level set topology optimization, Structural and Multidisciplinary Optimization, **revised**.

(5) Liu JK, Duke K, Ma YS, Multi-material plastic part design via the level set topology optimization method, Engineering Optimization, **revised**.

(6) Liu JK, Ma YS, A survey of manufacturing oriented topology optimization methods, Computers and Structures, **submitted**.

(7) Liu JK, Duke K, Cheng ZR, Ma YS, Automation of cyclic CAD/CAE integration, Advances in Engineering Software, **submitted**.

(8) Liu JK, Li L, Ma YS, Optimization-for-manufacture through level set topology optimization and single-sided curvature flow, Journal of Intelligent Manufacturing, **submitted**.

Chapters:

(9) Liu JK, Ma YS, Design history retrieval based structural topology optimization, Lecture Notes in Computer Science, vol. 9426, pp. 262-270.

(10) Xie YN, Liu JK, Liu HY, Ma YS (2013), Feature and interoperability of computer aided engineering systems, in Semantic modeling and interoperability in product and process engineering (Ma Ed.), Springer, London, pp. 143–191.

Contents

List of tables

List of figures

Chapter 1 Introduction

In this chapter, related background knowledge is introduced first. Starting from structural optimization, the related optimization methods and the categorization are discussed. Then, with the introduction of conventional Design-For-Manufacture (DFM) scheme, the novel Optimization-For-Manufacture (OFM) scheme is proposed. At the end, the contributions of this thesis are summarized.

1.1 Structural optimization

Structural optimization is the process of optimizing certain structural performance while satisfying all the constraints. It is applied in a variety of engineering fields, including vehicle body design, aircraft structure design, and building structure design, etc. The benefit is clear that, high-performance and light-weight structural design could be achieved while satisfying all design constraints; additionally, design automation is realized which improves the efficiency compared to the conventional trial and error method.

1.1.1 Optimization method

Structural optimization can be implemented by various methods, e.g. surrogate modeling based methods, heuristic methods, and deterministic method, etc. All these methods are effective and popular given certain scenarios, and some basic discussions are presented below:

Surrogate modeling rely on DoE (design of experiments) to perform test experiments and accordingly construct the surrogate model. It in fact replaces the accurate model by an empirical one, because the accurate model is non-trivial or even impossible to be derived [Wang et al. 2001; Gu et al. 2012]. Based on the constructed surrogate model, an optimization process is performed to find the design optimum, for which both the heuristic and deterministic methods could be applied. The advantage of using the surrogate model is that, it replaces the computationally expensive objective function evaluation by the approximated solution from the surrogate model [Younis and Dong 2010]. For the popular surrogate models, RSM (response surface method) employs low-order polynomial function to build the surrogate model and is suitable to simple

design space; Kriging and RBF (radial basis function) based methods could be applied to highly-nonlinear and multi-modal problems. In structural optimization field, surrogate modeling based methods are mainly applied to sizing and shape optimization problems [Park and Dang 2010; Cho et al. 2011; Wang et al. 2014].

Heuristic methods apply nature-inspired probabilistic approaches to search the optimum, such as the popular genetic algorithm, simulated annealing, and ant colony algorithm, etc. The advantages are that, a global optimum (at least close to) can be obtained and these methods are universally applicable [Younis and Dong 2010]. However, enormous calls of the numerical codes may be involved to repeatedly evaluate the objective function, which makes the process computationally expensive. Especially for the continuous and smooth non-linear problems, the heuristic methods are less efficient compared to other optimization methods. Therefore, heuristic methods are rarely applied to solve structural optimization problems, especially for the topology optimization problems.

Compared to the former two methods, deterministic methods are widely adopted by structural optimization activities, e.g. the popular adjoint sensitivity analysis [Choi and Kim 2005a, 2005b]. This is because deterministic methods rely on the rigorously derived sensitivity result to guide the search directions; therefore, the search efficiency is much higher than heuristic methods. Additionally, the number of calls of the numerical codes is not sensitive to the scale of design variables, and therefore, it is suited to large scale optimization problems. Even though there is the limitation that the process may be trapped at local optimum, the optimization results are generally accepted as close-to-optimal solutions given the large scale nature of topology optimization problems [Wang et al. 2003; Allaire et al. 2004].

1.1.2 Categories of structural optimization

, structural optimization can be classified into three categories: sizing optimization, shape optimization, and topology optimization, according to the different optimization targets.

Sizing optimization employs design changes only to the intuitive shape parameters, and therefore, no shape and topological changes could happen. Shape optimization is one step further, with which the structural boundary segments can freely evolve; however, no new frontiers would arise, in other words, no topological changes would happen. Then, in addition to the shape

deformations, topology optimization also allows the topological changes like boundary merging and splitting. Therefore, it has the greatest design freedoms and is the most creative. These days, topology optimization has been actively engaged in challenging design problems.

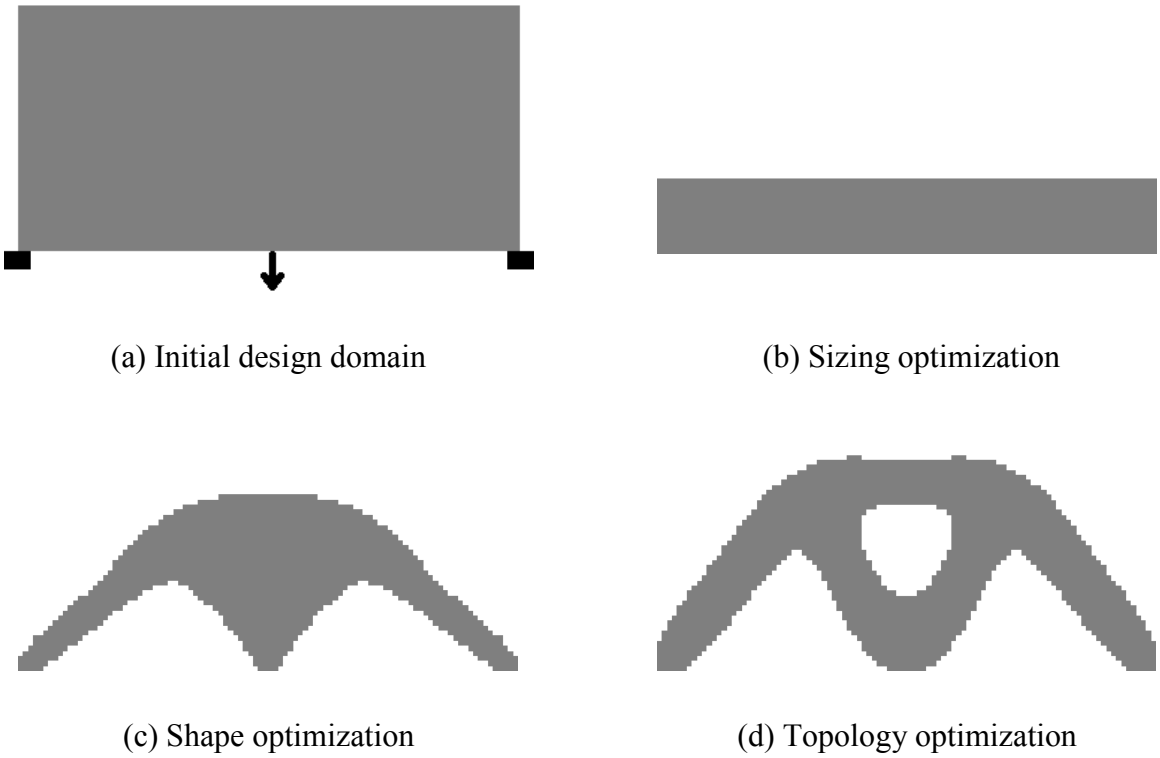

(a) Initial design domain (b) Sizing optimization

(c) Shape optimization (d) Topology optimization

Fig. 1.1 Categories of structural optimization

Currently, SIMP (Solid Isotropic Material with Penalization) [Bendsoe and Sigmund 2003], ESO (Evolutionary Structural Optimization) [Xie and Steven 1993], and level set [Wang et al. 2003; Allaire et al. 2004] are the main topology optimization methods. Each of these methods have its unique characteristics and comprehensive reviews can be found in [Eschenauer and Olhoff 2001; Rozvany 2001, 2009; Sigmund and Maute 2013; van Dijk et al. 2013; Deaton and Grandhi 2014; Munk et al. 2015].

1.2 Design-for-Manufacture (DFM)

In response to the fierce market competition and the quick product upgrade, various design-for-X (DFX) methodologies have been developed to simultaneously address functional and downstream engineering requirements during the product design process, which shortens the product development process and increases the product profitability and competitiveness.

Among the DFX methodologies, design-for-manufacture (DFM), the methodology which simultaneously addresses design objectives and manufacturing constraints, attracts a great deal of attention. According to [O'Driscoll 2002] approximately 80% of the manufacturing cost is determined by the product design, while manufacturing engineers can only influence a small portion of 20%. Therefore, there is a great potential of large amount of manufacturing cost saving by taking manufacturing into consideration during the product design process.

As the basis of DFM, engineering features, including both design feature and manufacturing feature, play a significant role in evaluating the product's functionality and manufacturability. Shah and Mantyla [1995] gave feature the definition that "Stereotypical knowledge structures embedded in cognitive process in design, analysis, planning, and all other engineering activities and that features are necessarily view point and application dependent". Compared to pure geometry, it is semantically a higher level, and the attached semantic information enables the product interpretation from different engineering perspectives.

Design feature defines the association between functionality evaluation (FE) and geometry parameters, and these associations can be constructed from the initial conceptual design stage by applying some classic methodology, e.g. FBS (Function-Behavior-Structure) [Gero 1990]. In this way, the design functionality can be timely and quantitatively tracked during the entire design process.

Manufacturing feature defines the volume of material to be removed by the manufacturing process, such as pocket, slot, and profile, etc. [Srikumaran and Sivaloganathan 2005] and simultaneously involves the full set of manufacturing information, including machine tool, cutting tools, cutting direction, recommended tolerances and surface finishing values, etc. [Hoque et al. 2013]. Normally, manufacturing features are not directly available. They are interpreted from the design feature model through feature recognition or other approaches, and a well-defined manufacturing feature library is mandatory [Miao et al. 2002]. Additionally, it is significant to develop or select the appropriate manufacturability evaluation (ME). Three categories of ME are popular [Kerbrat et al. 2011]: binary, qualitative, and quantitative. Binary ME is simple, which evaluates the overall product or local manufacturing features either manufacturable or non-manufacturable, according to the available manufacturing resources. Qualitative ME makes conclusions such as "good", "bad", or "intermediate". The standard is

blurred and depends heavily on specific expert knowledge. The last category makes quantitative ME (such as manufacturing time and cost) based on certain formulas or algorithms. It is concrete and intuitive to designers, but other technologies are needed such as feature-based manufacturing cost estimation [Liu et al. 2013].

The overall design flow of DFM is demonstrated in Fig. 1.2a [Gupta and Nau 1995]. It can be seen that cyclic design process is employed to repeatedly evaluate the product's functionality and manufacturability. However, because the number of repetitions is unpredictable and designers are closely involved in the loops, the overall design flow is time-consuming and labor-costly, and the product delivery cannot be guaranteed within certain time frame.

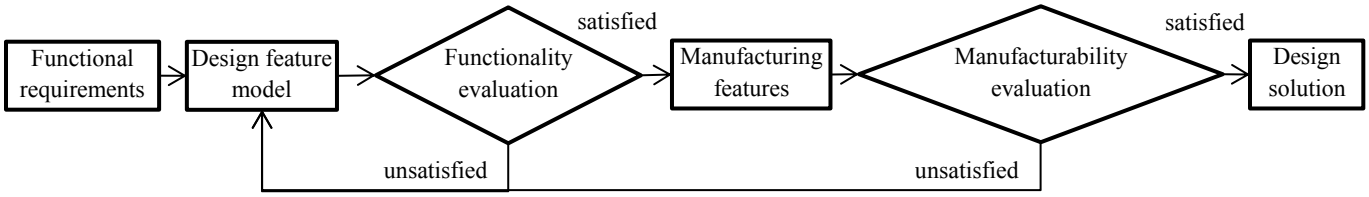

(a) Design flow of DFM

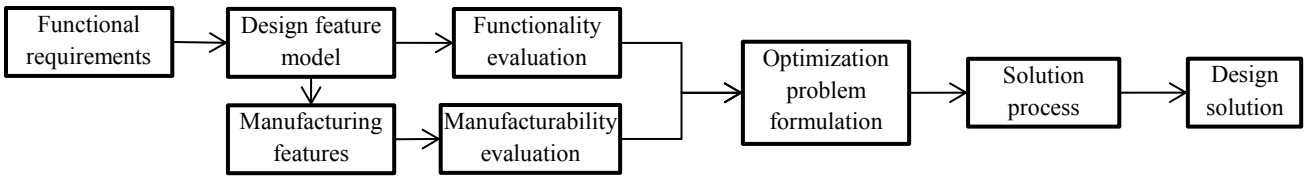

(b) Design flow of OFM

Fig. 1.2 Design flow comparison between DFM and OFM

The research presented in this thesis proposes a new concept, named optimization-for-manufacture (OFM), in order to fix the low-efficiency issue of DFM. Design flow of OFM is presented in Fig. 1.2b. In contrast to DFM, the sequential design flow of DFM has been transformed into a parallel one. An multi-objective optimization problem is constructed and solved to concurrently satisfy the functionality and manufacturability requirements, and of course, both FE and ME are involved in the problem formulation. For superior characteristics of OFM, design automation is realized which relieves the close designer interaction and shortens the product development process, and design optimality is guaranteed especially compared to the trial and error method employed by DFM.

1.3 Contribution of this research

The research effort described in this thesis is mainly performed with the given industrial problems of machining and injection molding. The main methodology is level set topology optimization. The author has made efforts to further develop the methodology to better support the manufacturing-oriented product design.

To be specific, geometry feature-based level set topology optimization is comprehensively studied, and the innovative implicit (**Chapter 3**) and explicit (**Chapter 4**) feature-based level set topology optimization methods are developed, which could produce directly manufacturable designs given the injection molding and machining processes, respectively. Additionally, the B-rep (Boundary representation) geometry based topology optimization realizes the explicit feature-based design in B-rep format (**Chapter 5**), which greatly simplifies the post-processing from the topological design to a solid-oriented CAD model, and also promotes the automation of CAD/CAE integration. Moreover, the semantic information embedded in manufacturing features is incorporated into the optimization problem to concurrently optimize the product's functionality and manufacturability (**Chapter 6**). This is a big breakthrough of the topology optimization development. For injection molding parts, the two-scale extension of level set topology optimization has been made, which addresses the fiber-reinforced plastic part design (**Chapter 7**).

At the end, the author applies the multi-material level set topology optimization to the slotted liner design (**Chapter 8**), which is an important device applied in the SAGD (steam assisted gravity drainage) process for oil recovery. This is a novel industrial application and contributes to the local oil industry.

Throughout the **Chapters 3-7**, it can also be summarized that a new concept of OFM is proposed in this research; and the contents in these chapters can be regarded as preliminary implementations. The author believes that this OFM scheme can partially replace the conventional DFM in the near future.

In summary, the generic research scheme is to realize the feature-based level set topology optimization.

Chapter 2 Background and literature review

2.1 Level set topology optimization

2.1.1 Development of level set topology optimization

Level set method was initially developed as a mathematical tool for velocity field based interface track [Osher and Sethian 1988]. Guided by the iteratively calculated velocity information, the implicitly represented interface can properly evolve, merge, and split, with which both shape and topological changes could happen. Because of this characteristic, in the past decades, level set method has been developed into a powerful topology optimization tool to perform innovative and efficient conceptual design activities [Sethian and Wiegmann 2000; Wang et al. 2003, Allaire et al. 2004; van Dijk et al. 2013].

It is powerful because level set topology optimization has been applied to solve a broad range of design problems governed by different physical disciplines, i.e. solid mechanics [Wang et al. 2003; Allaire et al. 2004], fluid dynamics [Zhou and Li 2008; Deng et al. 2013a, 2013b], and thermal dynamics [Ha and Cho 2005; Zhuang et al. 2007; Yamada et al. 2011] etc. It is innovative because it helps the engineers to think out of the box to generate innovative design ideas and even create new designs of already highly engineered products [Zhou et al. 2011].

2.1.2 Basic principles

Definition of the level set function is presented in Eq. (2.1), as:

$$\begin{cases} \Phi(\boldsymbol{X}) > 0 & \forall \boldsymbol{X} \in \Omega \ \ (material\ domain) \\ \Phi(\boldsymbol{X}) = 0 & \forall \boldsymbol{X} \in \Gamma \ \ (interface) \\ \Phi(\boldsymbol{X}) < 0 & \forall \boldsymbol{X} \in D \backslash \Omega \ \ (void) \end{cases} \tag{2.1}$$

and the schematic plot is show in Fig. 2.1.

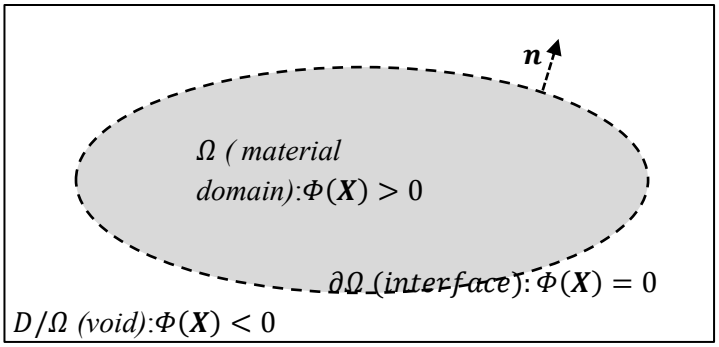

Fig. 2.1 Schematic plot of the level set field

Discrete level set representation is generally applied, with which the level set values are discretely stored at the mesh nodes, and determined by the signed distance information, i.e. the shortest distance from the node to the interface.

Update of the level set function depends on the interface propagating velocities, specifically only the part normal to the interface. For instance, in Fig. 2.1, $\boldsymbol{n} = -\frac{\nabla\Phi(\boldsymbol{X})}{|\nabla\Phi(\boldsymbol{X})|}$ is a unit vector normal to the interface pointing from the material domain outwards, and only the normal part $V_n = \boldsymbol{V} \cdot \boldsymbol{n}$ of the velocity $\boldsymbol{V}$ has the effect on the interface propagation, but not the tangential part.

V_n is generally derived through sensitivity analysis. For example, the basic level set topology optimization problem of compliance minimization is demonstrated as:

$$\begin{aligned} \min \quad & C = \int_D \boldsymbol{D}\boldsymbol{e}(\boldsymbol{u})\boldsymbol{e}(\boldsymbol{u})H(\Phi)d\Omega \\ s.t. \quad & a(\boldsymbol{u},\boldsymbol{v},\Phi) = l(\boldsymbol{v},\Phi), \forall \boldsymbol{v} \in U \\ & V = \int_D H(\Phi)d\Omega \le V_{max} \\ & a(\boldsymbol{u},\boldsymbol{v},\Phi) = \int_D \boldsymbol{D}\boldsymbol{e}(\boldsymbol{u})\boldsymbol{e}(\boldsymbol{v})H(\Phi)d\Omega \\ & l(\boldsymbol{v},\Phi) = \int_D \boldsymbol{p}\boldsymbol{v}H(\Phi)d\Omega + \int_D \boldsymbol{\tau}\boldsymbol{v}\delta(\Phi)|\nabla\Phi|d\Omega \end{aligned} \tag{2.2}$$

in which $\boldsymbol{u}$ is the displacement vector and $\boldsymbol{v}$ is the test vector. $U = \{\boldsymbol{v} \in H^1(\Omega)^d | \boldsymbol{v} = 0 \; on \; \Gamma_D\}$ is the space of kinematically admissible displacement field. $\boldsymbol{D}$ is the Hooke's law for the defined isotropic material and $\boldsymbol{e}(\boldsymbol{u})$ is the strain. $\boldsymbol{p}$ is the body force and $\boldsymbol{\tau}$ is the boundary traction force. V_{max} is the upper bound of the material volume. C represents the structural compliance, and the second line is the weak form of the governing equation.

Eq. (2.3) and (2.4) define the Heaviside function H and the Dirac Delta function δ. These functions are applied to analytically construct the domain and interface integration.

$$\begin{cases} H(\Phi) = 0 & \Phi < 0 \\ H(\Phi) = 1 & \Phi \geq 0 \end{cases} \tag{2.3}$$

$$\begin{cases} \delta(\Phi) = 0 & \Phi \neq 0 \\ \delta(\Phi) = +\infty & \Phi = 0 \end{cases} \qquad \int_{-\infty}^{+\infty} \delta(\Phi) d\Phi = 1 \tag{2.4}$$

Then, the sensitivity result of this problem is presented in Eq. (2.5) [Wang et al. 2003], as:

$$V_n = -[\lambda - \boldsymbol{D}\boldsymbol{e}(\boldsymbol{u})\boldsymbol{e}(\boldsymbol{u})] \tag{2.5}$$

Details about the derivation will be presented in Chapter 3. λ is the Lagrange multiplier. It can be defined in multiple ways: applying fixed value [Allaire et al. 2004], calculating based on volume conservation [Wang et al. 2003], using the bi-sectioning algorithm [Wang et al. 2007], or applying the augmented Lagrange method.

Once V_n is obtained, the level set function can be updated by solving the Hamilton-Jacobi equation:

$$\frac{\partial \Phi(\boldsymbol{X})}{\partial t} = V_n |\nabla \Phi(\boldsymbol{X})| \tag{2.6}$$

The upwind scheme [Osher and Sethian 1988; Wang et al. 2003, Allaire et al. 2004] is commonly applied with the following update equation for 2D problems:

$$\Phi_{jk}{}^{I+1} = \Phi_{jk}{}^{I} + \Delta t[\max(V_n{}^{jk}, 0)\nabla^+ + \min(V_n{}^{jk}, 0)\nabla^-] \tag{2.7}$$

in which,

$$\nabla^{+}= [\max(D_{jk}{}^{-x},0)^2 + \min(D_{jk}{}^{+x},0)^2 + \max(D_{jk}{}^{-y},0)^2 + \min(D_{jk}{}^{+y},0)^2]^{1/2}$$
$$\nabla^{-}= [\min(D_{jk}{}^{-x},0)^2 + \max(D_{jk}{}^{+x},0)^2 + \min(D_{jk}{}^{-y},0)^2 + \max(D_{jk}{}^{+y},0)^2]^{1/2} \quad (2.8)$$

In Eq. (2.7) and (2.8), (j,k) denotes the two-dimension grid node index. $D_{jk}{}^{\pm x}$ and $D_{jk}{}^{\pm y}$ are the forward and backward finite difference operators. Δt should satisfy the Courant-Friedrichs-Lewy (CFL) condition [Osher and Fedkiw 2003].

Additionally, in order to maintain the accurate interface evolvement, the level set function should be re-initialized to maintain the signed distance property for every a few iterations, as,

$$|\nabla \Phi| = 1 \quad (2.9)$$

Other than the discrete representation, parametric level set definitions are also available, such as the radial basis function based [Wang and Wang 2006; Wang et al. 2007; Luo et al. 2008b; Luo et al. 2009; Ho et al. 2011; Ho et al. 2013; Liu et al. 2014] and spline based [Chen et al. 2007; Chen et al. 2008a] definitions. With the parametric definitions, both design space flexibility and convergence speed of the discrete level set topology optimization can be enhanced, because new holes can be naturally generated, and the upwind schemes, velocity field, and re-initialization can be eliminated.

2.1.3 A comparative discussion

A comparative discussion will be made in this section between the SIMP and level set methods, give their popularity.

The basic topology optimization problem of compliance minimization based on SIMP method is demonstrated in Eq. (2.10).

$$min.\ \ C = \boldsymbol{U}^T\boldsymbol{K}\boldsymbol{U} = \sum_{e=1}^{n} \boldsymbol{u}^e\boldsymbol{k}^e\boldsymbol{u}^e = \sum_{e=1}^{n} (\rho^e)^p \boldsymbol{u}^e\boldsymbol{k}_0\boldsymbol{u}^e$$

$$s.t.\ \ V = \sum_{e=1}^{n} x^e v^e \leq V_{max} \tag{2.10}$$

$$\boldsymbol{K}\boldsymbol{U} = \boldsymbol{F}$$

$$0 < \rho_{min} \leq \rho^e \leq 1$$

where $\boldsymbol{U}$ and $\boldsymbol{F}$ are the global displacement vector and force vector, respectively. $\boldsymbol{K}$ is the global stiffness tensor; $\boldsymbol{u}^e$ and $\boldsymbol{k}^e$ are the element displacement vector and stiffness tensor, respectively; ρ^e is the element density and ρ_{min} is the lower bound. v^e is the element volume and V_{max} is the upper bound of the material volume. p is the penalization factor.

Through comparing Eq. (2.2) and Eq. (2.10), it can be observed that: SIMP method uses element densities as the optimization variables which is counted as an element based method; instead, level set method defines the design domain by the signed distance information, and the material/void interface by the zero-value level set contour, which belongs to a interface based method. It is widely recognized that, SIMP method is easy in implementation and employs high computational efficiency, but it has the limitations of deriving check-board pattern and blurred material/void interface of the final topological design. In contrast, the level set method employs clear-cut and smooth interface. More importantly, the diversified level set definitions can be applied in a hybrid manner which enables the concurrent sizing, shape, and topology optimization. Even geometry features could be involved in the optimization problems, which builds the connection between the emerging topology optimization and the popular feature-based design.

Therefore, in this research, the majority of the works will be performed based on the level set method, while in certain situations, both SIMP and level set methods will be applied in a hybrid manner.

2.2 Manufacturing oriented topology optimization

Development of topology optimization mainly concentrates on the following aspects [Sigmund and Maute 2013]: (1) low CPU time, (2) generality of applicability, (3) reliability, (4) simplicity of implementation, and (5) simplicity of topologies obtained. For the author's interest, the aspects (2) and (5) are highlighted, because they could make topology optimization friendly to manufacture. Topology optimization pursues the result optimality and generally produces very complex topologies, which can only be manufactured through additive manufacturing. However, in practice, additive manufacturing is only an emerging technique while the conventional manufacturing methods such as machining and injection molding/casting still dominate the market. Therefore, coming back to the aspects (2) and (5), topology optimization problems should be constructed and solved with careful considerations of the manufacturing requirements, in this way to generate simple topologies which are manufacturable by the conventional manufacturing methods.

2.2.1 Machining oriented topology optimization

Rules for machining part design are frequently violated by the topological designs. For instance, interior holes are non-manufacturable through machining but are commonly mandatory for a superior structural performance. With these violations, CAD model construction and the following shape optimization are complicated, because it is non-trivial and somehow arbitrary to remove these violations. For this reason, it is necessary to carefully consider the machining rules and properly reflect them in the optimization problem.

Size control is significant in guaranteeing the machinability: the void size should be controlled by being bigger than the minimum cutting tool size, and very small features should be avoided because they may cause machining difficulties.

Concerning size control in topology optimization, the pioneering works can be tracked back to the filtering method [Sigmund 1997] and the local gradient constraint method [Petersson and Sigmund 1998]. These methods were developed mainly to eliminate the checker board patterns and the mesh dependencies [Sigmund and Petersson 1998], and marginally, they served the purpose of constraining the minimum component/void size.

In order to strictly constrain the minimum length scale, Guest et al. [2004] developed the Heaviside projection method. Nodal densities were defined as the optimization variables, and the element density was calculated through Heaviside projection of the nodal values with the minimum length scale embedded in the operator. However, this method was only effective in controlling the minimum length scale of components but not the voids. Later, this method was modified through double projections restricting the minimum length scales of both the components and voids [Guest 2009a]. Sigmund [2007] developed a morphology-based density filtering scheme which generates black-and-white design with well satisfied minimum length scale. Four morphology operators were developed: erode, dilate, open, and close, to control the single-phase minimum length scale. For double-phase minimum length scale control, two enhanced operators: open-close and close-open, were developed, but sensitivity analysis cost is overweighed. Fig. 2.2 demonstrates a few examples of applying these operators. Later, a robust topology optimization method [Sigmund 2009; Wang et al. 2011; Schevenels et al. 2011] was developed based on these morphology operations. Better local length scale control was realized for both phases [Wang et al. 2011; Schevenels et al. 2011] if the multiple realizations can keep a consistent topology, even though it is not always true [Zhou et al. 2015]. Also, this method had the drawback of performing multiple finite element analyses in each optimization iteration.

Table 2.1 A list of density filters for component/void size control

Density filter	Equation
Heaviside projection [Guest et al. 2004]	$\rho^e = 1 - e^{-\beta\mu^e(\boldsymbol{\rho_n})} + \mu^e(\boldsymbol{\rho_n})e^{-\beta}$ $\mu^e = \frac{\sum_{j\in S_e}\rho_j\omega(\boldsymbol{x_j}-\overline{\boldsymbol{x}}^e)}{\sum_{j\in S_e}\omega(\boldsymbol{x_j}-\overline{\boldsymbol{x}}^e)}$ $\omega(\boldsymbol{x_j}-\overline{\boldsymbol{x}}^e) = \begin{cases}\frac{r_{min}-\lvert\boldsymbol{x_j}-\overline{\boldsymbol{x}}^e\rvert}{r_{min}} & if\ \boldsymbol{x_j}\in S_e \\ 0 \quad otherwise\end{cases}$ in which β indicates the curvature of regulation, μ^e is the projected element density, $\boldsymbol{\rho_n}$ is the set of nodal densities, ρ_j is the *j*th nodal density, and S_e is the set of nodes within the circular area of radius r_{min}.
Double Heaviside projection [Guest 2009a]	$\rho^e = \frac{1}{2}({\rho_0}^e + {\rho_1}^e)$ ${\rho_0}^e = e^{-\beta\mu_0^e(\boldsymbol{\rho_n})} - \mu_0^e(\boldsymbol{\rho_n})e^{-\beta}$ ${\rho_1}^e = 1 - e^{-\beta\mu_1^e(\boldsymbol{\rho_n})} + \mu_1^e(\boldsymbol{\rho_n})e^{-\beta}$ $\mu_0^e = \frac{\sum_{j\in S_e}(1-\rho_j)\omega(\boldsymbol{x_j}-\overline{\boldsymbol{x}}^e)}{\sum_{j\in S_e}\omega(\boldsymbol{x_j}-\overline{\boldsymbol{x}}^e)}$ $\mu_1^e = \frac{\sum_{j\in S_e}\rho_j\omega(\boldsymbol{x_j}-\overline{\boldsymbol{x}}^e)}{\sum_{j\in S_e}\omega(\boldsymbol{x_j}-\overline{\boldsymbol{x}}^e)}$
Dilate [Sigmund 2007]	$\rho^e = \log\left(\frac{\sum_{j\in S_e} e^{\beta\rho_j}}{\sum_{j\in S_e}1}\right)/\beta$ It is noted that ρ_j here is the *j*th element density.
Erode [Sigmund 2007]	$\rho^e = 1 - \log\left(\frac{\sum_{j\in S_e} e^{\beta(1-\rho_j)}}{\sum_{j\in S_e}1}\right)/\beta$
Close [Sigmund 2007]	Dilation followed by erosion
Open [Sigmund 2007]	Erosion followed by dilation
Close-open [Sigmund 2007]	Close followed by open
Open-close [Sigmund 2007]	Open followed by close

* Please refer to the original works for more specific meanings of the characters.

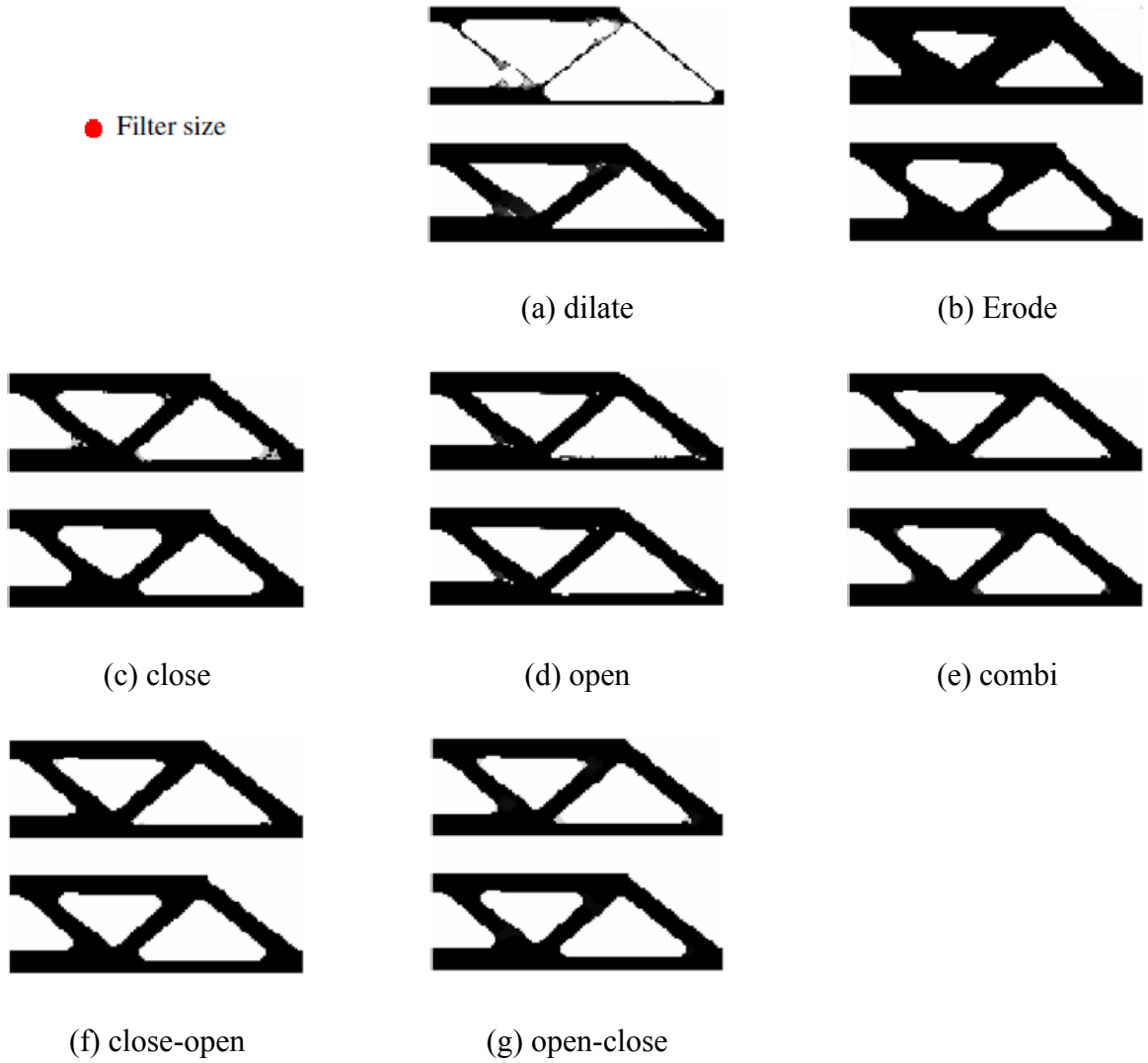

Fig. 2.2 Results for the MBB (Messerschmidt-Bolkow-Blohm) example with the morphology operators. For each operator, two images are shown. The upper one shows the design variable field and the lower one shows the filtered density field. [Sigmund 2007]

Other than the density filters, it is also widely applied of constraints. Poulsen [2003] developed the MOLE (MOnotonicity based minimum LEngth scale) method to impose the minimum length scale. This method relied on the local integral constraints checking the monotonic density variations. By satisfying the local constraints, the minimum length scale is strictly satisfied for both the components and voids. Zuo et al. [2006] applied a minimum hole size constraint to remove the small hole features from the optimization result. Guest et al. [2009b] constrained the

maximum component length scale by restricting the material volume within circular areas to be smaller than the area size. This method also works for voids. More recently, Zhang et al. [2014] realized the simultaneous maximum and minimum length scale control. The structural skeleton was extracted, and elements located on it were applied of local length scale constraints. In Zhou et al. [2015], the structural indicator function based geometric constraints were developed based on the filtered and physical density fields. Strictly-satisfied minimum length scale was realized and the multiple finite element analyses in each iteration were avoided compared to the robust topology optimization [Sigmund 2009; Wang et al. 2011; Schevenels et al. 2011]. It is noted that all works above are based on the SIMP method.

The level set method is also capable of size control, and in some aspects, it has demonstrated unique characteristics. Chen et al. [2008b] and Luo et al. [2008a] applied the quadratic energy functional as part of the objective function for rib thickness control, which successfully realized the strip-like design with controlled thickness. Guo et al. [2014a] realized rib thickness control by concurrently imposing maximum and minimum thickness constraints. This method relied on the structural skeleton similar to [Zhang et al. 2014], as well as the signed distance information. Allaire et al. [2014b] explored the thickness control mechanism in depth, with diversified schemes of maximum thickness only, minimum thickness only and also the hybrid manners; additionally, a comparative discussion between thickness control constraints and functional was given.

In comparison of the methods for size control, it seems more natural to apply the level set method, because it defines the entire design domain by a signed distance function which eases the component/void size measurement. For instance, level set method has demonstrated the ability of realizing constant rib thickness. However, SIMP method in fact has the potential to realize equivalent control effects, especially given the active research in this field. It would not be surprising to find more works of the simultaneous maximum and minimum length scale control in the near future. In addition, it is interesting to find out that the level set method has only been applied to constrain the component length scale but not the voids, even though it has the potential.

2.2.2 Injection molding/casting oriented topology optimization

Injection molding and casting are two similar manufacturing processes. They share some common procedures that: liquefy the material, inject/pour the liquid material into the cavity of desired shape, cooling and solidify the material, open the mold and eject the part. These procedures are distinctive from the material removal based machining process, which makes the injection molding/casting oriented topology optimization methods strategically different.

An important principle is to avoid interior voids and undercuts (see Fig. 2.3), because these details can only be molded by using extra devices like mold inserts and will complicate the ejection process. In literature, there are effective modifications of the optimization algorithms in satisfying this requirement.

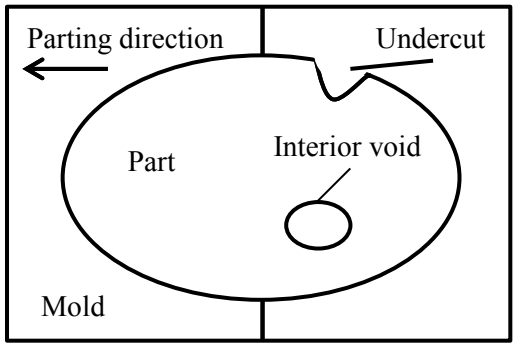

Fig. 2.3 Interior void and undercut

Based on SIMP method, Zhou et al. [2002] and Schramm and Zhou [2006] developed the casting constraints that elements were only allowed of monotonous density changes along the casting direction. Stromberg [2010] applied the molding/casting constraints for unilateral contact problems. Lu et al. [2012] applied the molding/casting constraints in a multi-directional manner. Gersborg and Andreason [2011] modified the SIMP method by using a single material density variable to decide the solid-void interface for each row of elements along the casting direction, which avoided the large number of constraints especially for refined mesh. Guest and Zhu [2012] extended the projection-based algorithm to satisfy the milling and casting restrictions. Additionally, a short review about the casting part design through topology optimization can be found in [Harzheim and Graf 2002; 2005; 2006].

As for level set method, Xia et al. [2010a] satisfied the no undercut and void restrictions for casting parts by adjusting the design velocity only parallel with the pre-defined casting direction. In this way, once the initial design satisfies the casting restrictions, the topology design is guaranteed castable. In Xia's work [2010a], the velocity is aligned to the casting direction; and the algorithm used cannot recover the material portions once removed. An enhanced version was reported by Allaire et al. [2013]. They added a minimum thickness constraint in the casting direction, and therefore avoided the overly removed material portions.

In summary, both the SIMP and level set methods can effectively avoid interior voids and undercuts through certain modifications, and no one has demonstrated outstanding characteristic compared to the other. On the other hand, it should be noted that interior voids and undercuts sometimes can cause difficulties in machining as well, so the modifications mentioned in this sub-section equally applies to machining oriented topology optimization methods.

Another important aspect to be addressed is the constant rib thickness control. For injection molding/casting, part cooling and solidification are carried out with external devices such as cooling channels and air blowers. These devices speed up the cooling process but intensify the cooling imbalance, which causes residual thermal stress and impacts the part quality, especially for the areas of varying rib thickness. Therefore, small rib thickness gradient or even constant rib thickness is required to relax the cooling imbalance.

It is non-trivial to realize the constant rib thickness through topology optimization. Extra control efforts are mandatory to influence the shape and topology evolvement process. As reviewed earlier, the efforts based on SIMP method can only satisfy the single-sided length scale control, while rarely realize the concurrent minimum and maximum length scale control [Zhang et al. 2014]. Comparatively, it is more suited to apply the level set method, because both constant rib thickness [Chen et al. 2008b; Luo et al. 2008a] and concurrent maximum and minimum length scale control [Guo et al. 2014a; Allaire et al. 2014b] have been realized, owing to the signed distance information which greatly eases the thickness track.

In this research, a new thickness control functional is developed which employs simple form and is efficient in numerical implementation.

2.3 Geometry feature-based level set topology optimization

In recent years, the development of engineering feature-based level set topology optimization methods have gained in popularity. Only the discrete and parameterized geometries are not sufficient for engineering applications, while the featurized geometries with well-defined engineering knowledge need to be addressed [Ma 2013]. So far, two streams of geometry feature-based level set methods have been developed based on shape and topological sensitivity analysis: implicit feature control and explicit feature manipulation.

2.3.1 Implicit feature control

The first stream is about implicit feature control. An implicit feature means that the geometry approximately approaches certain geometry pattern without sizing or shape control parameters. An example is presented in Fig. 2.4 that, by implementing implicit feature control, the flow channel employs nearly uniform channel width (see Fig. 2.4b); however, no parameters exist to adjust the flow channel's size or shape before it is post-treated into a parametric CAD model. It is applicable of the implicit feature control that, geometry feature-based design is strongly expected while the initial input is arbitrary.

(a) Flow channel design without implicit feature control

(b) Flow channel design with implicit feature control

Fig. 2.4 Implicit feature control

For the past efforts about implicit feature control, Chen et al. [2008b] and Luo et al. [2008a] applied the quadratic energy functional as part of the objective function and proposed the shape

feature control method which successfully realized the strip-like design with controlled thickness. Guo et al. [2014a] realized strip-like design by imposing maximum and minimum thickness constraints on the signed distance function. However, simultaneously introducing the maximum and minimum length scale control frequently leads to local optima. Allaire et al. [2014b] explored the thickness control mechanism in depth, with diversified schemes of maximum thickness only, minimum thickness only and also the combined manners; additionally, a comparative discussion between thickness control constraints and functional was demonstrated. Limitation of the current development is that by adding constraints, one can only loosely realize the feature-based design; the only work using control functional employs the quadratic energy functional in the form of double-layer boundary integration, which is difficult in numerical implementation [Guo et al. 2014a]. Therefore, a new thickness control functional is developed in this research. It employs simple expression and is efficient in numerical implementation.

2.3.2 Explicit feature manipulation

The second stream, of geometry feature-based level set methods, is about direct manipulation on the explicit feature primitives. An explicit feature in this context means that the geometry is intuitively constrained by sizing and shape parameters, and these parameters can be applied as optimization variables. An example is presented in Fig. 2.5 that, the explicit feature-based optimization only manipulates the sizing parameters to derive the optimal design.

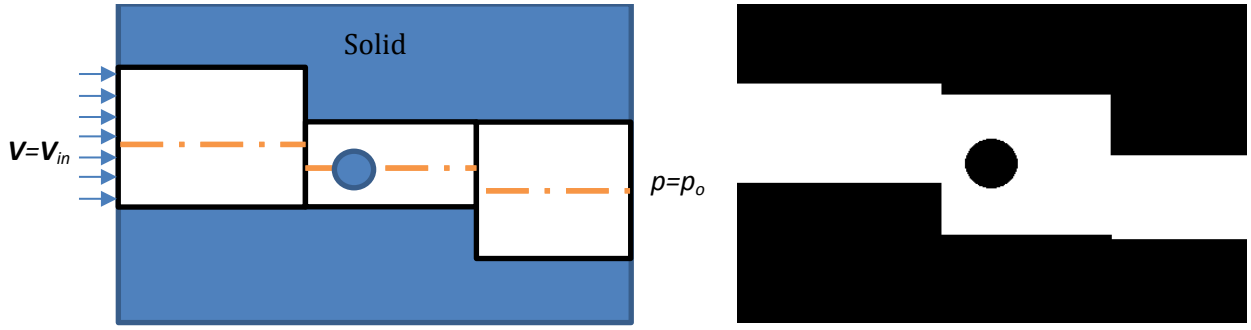

(a) Initial flow channel

(b) Flow channel after explicit feature-based optimization

Fig. 2.5 Explicit feature manipulation

For the existing methods of explicit feature manipulation, Chen et al. [2007; 2008a] fully parameterized the level set functions by modeling form features with intuitive shape parameters

and freeform features with B-splines. The feature primitives were combined through R-functions. Parametric sensitivity analysis and design update are enabled by the differential properties of implicit function [Shapiro and Tsukanov 1999]. Cheng et al. [2006] and Mei et al. [2008] applied a similar way to perform parametric sensitivity analysis on the explicit feature primitives. More importantly, they developed an initial procedure to topologically insert explicit feature primitives into the design domain, which made it possible to derive feature-based design without relying on feature-based input. Gopalakrishn and Suresh [2008] contributed the feature-specific topological derivative algorithm introducing both internal and boundary features under 2D scheme. This work provided a good theoretical basis of topological sensitivity analysis on inserting certain explicit features. Zhou and Wang [2013] conducted the explicit feature manipulation in a different way, by regulating the boundary velocity fields via least squares fitting. By doing so, shape characteristics of the feature primitives can be reserved during the Hamilton-Jacobi equation based design update. More recently, Liu et al. [2014] conducted a similar work as [Chen et al. 2007; 2008a], but they applied RBFs (Radial Basis Functions) to model the freeform features. Guo et al. [2014b] contributed a novel level set method. The design domain was initially distributed with explicit feature components, which had freedoms of scaling, movement, and rotation. By optimizing these freedoms, explicit feature-based design could be generated.

Except for the pure level set approaches, there are also hybrid methods which simultaneously optimize the layout of explicit features represented by the level set function, and the material distribution of supporting structures through density based method [Kang and Wang 2013; Xia et al. 2013].

For all the works reviewed above, efforts are focused on maintaining and manipulating the existing explicit feature primitives, but it is still infeasible to insert new primitives during the optimization process, which is also the case for software tools like PareTO [2013]. The only exception is the work from [Cheng et al. 2006; Mei et al. 2008]. They applied the topological derivative to insert new explicit feature primitives during the first few iterations of the optimization process. However, as mentioned earlier, this method is still not well-developed for several reasons:

- The topological derivative theory is designed to insert infinitesimal holes, but local analysis about the exact feature type to be inserted can be rather sophisticated. Therefore, they

developed an in-between feature primitive to be inserted which approaches to the specific feature type during the optimization process. However, they also mentioned that this process was slow [Mei et al. 2008];

- The scale control is far from ideal for the infinitesimal nature of topological derivative. A large number of small in-between feature primitives are inserted at the initial iterations, which generate numerous parameters to be controlled. Furthermore, the final result is composed of too many small segments; a "feature match process" is indispensable to idealize the optimized model, for which the resulting relaxation of the objective value was not discussed;
- This method has not been proven to be effective in 3D scheme.

Gopalakrishn and Suresh [2008] contributed the explicit feature-specific topological derivative algorithm including both internal and boundary features under 2D scheme. This work provides a good theoretical basis for topological sensitivity analysis on inserting certain explicit features. However, the possibility and effectiveness of its implementation under the level set framework has not been explored yet.

At the end of this sub-section, we conclude that a comprehensive explicit feature-based level set topology optimization method is still in great need. Specifically, this method should have the following characteristics:

- New explicit feature primitives can be automatically selected and inserted during the optimization process;
- The scale of explicit feature primitives should be controllable;
- No post-processing is needed to produce a perfect explicit feature-based design for being directly imported into the CAD system;
- It can be applied for 3D scheme.

All these desired characteristics will be satisfied by the proposed method in this research, while Table 2.2 demonstrates a comprehensive summary about the performance of the existing methods on the listed characteristics.

Table 2.2 Characteristics of existing feature-based level set methods

	In-process insertion of feature primitives	Scale control of feature primitives	Need of post-processing for explicit feature-based result	Applied in 3D schemes
Implicit feature-based approaches:				
Chen et al. [2008b]; Luo et al. [2008a]; Guo et al. [2014a];	Yes	Yes	Yes	To be proven
Allaire et al. [2014b];	Yes	Yes	Yes	Yes
Explicit feature-based approaches:				
Chen et al. [2007; 2008a]	No	N/A	No	Yes
Cheng et al. [2006]; Mei et al. [2008];	Yes	No	Yes	No
Zhou and Wang [2013];	No	N/A	No	Yes
Liu et al. [2014];	No	N/A	No	To be proven
Guo et al. [2014b];	No	Yes	No	To be proven
Method proposed in this research;	Yes	Yes	No	Yes

2.4 CAD/CAE integration

Automated CAD (computer-aided design)/CAE (Computer-aided engineering) integration has been a challenging research issue for decades. Even though many research efforts have been spent on it, human interactions are still required which makes it tedious, labor-intensive, and costly. Therefore, in this research, it is of the authors' interest to explore the possibility of realizing the full automation. It is worth noting that, the inverse integration is emphasized and the B-rep geometry based topology optimization method will be an ideal solution.

Generally, CAD/CAE integration can be divided into two sub-problems (see Fig. 2.6): the forward integration to prepare the CAD model for CAE analysis; and the inverse integration to adjust the CAD model based on the CAE result.

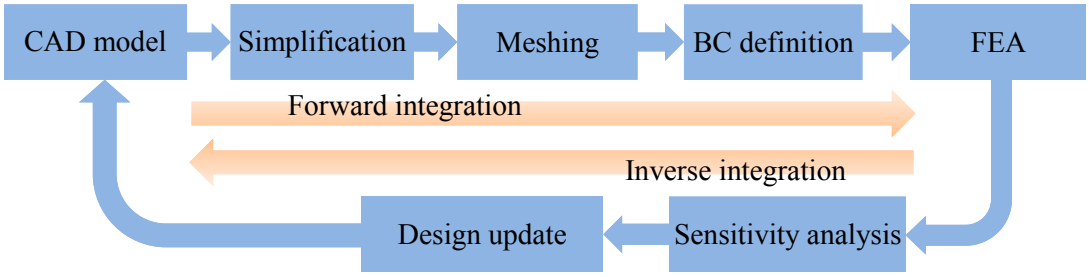

Fig. 2.6 Cyclic CAD/CAE integration

2.4.1 Forward integration

For forward integration, there are mainly four intermediate steps: CAD model simplification, meshing, boundary condition (BC) definition, and the CAE analysis. A major problem of the forward integration is about the unexpected long preparation time of the analysis model, especially given the cyclic design process. To be specific, each time the CAD model is perturbed, the intermediate steps, simplification, meshing and BC definition, need to be repeated and routine user interactions are needed. These steps make the design process less efficient and labor-intensive. Therefore, many research works attempted to reduce the analysis model preparation time. A review of model simplification, meshing and BC definition will be presented.

(1) Model simplification. This is a step of simplifying the design in order to save computation time. It generally includes two parts: remove small geometry details and abstract the geometry through dimension reduction. A comprehensive review can be found in [Thakur et al. 2009] about the specific techniques.

From the perspective of CAD/CAE integration, it is popular to apply unified data model to concurrently store both the complete and simplified geometry information, as well as the in-between association. In this way, the repeated model simplifications can be eliminated given the cyclic design process. Deng et al. [2002] proposed the integrated CAD-CAE feature concept for plastic parts. It contains both geometry and non-geometry information related to both design and analysis activities, with which analysis model could be automatically prepared subject to any

CAD model changes. Lee [2005] developed the feature-based non-manifold modeling system. A master model was created containing multi-resolution and multi-abstraction geometry information, from which both the CAD solid model and the non-manifold analysis model could be extracted. Gujarathi and Ma [2011] developed a common data model to realize the parametric CAD/CAE integration.

In this research, it is not intended to further investigate the simplification techniques or the unified data model. Therefore, small geometry details will not appear in the studied examples.

(2) Meshing is a mandatory and the most time-consuming step in the forward process. Especially for complex geometry, user interaction is commonly needed to guarantee the mesh quality. In case of a large number of design cycles, it is expected to eliminate the repeated meshing efforts to save time and labor. For minor sizing and shape changes, mesh deformation is a feasible solution; however, for major shape and topological changes, it is non-applicable of mesh deformation. As reviewed in [Shapiro et al. 2011], boundary element method and meshfree methods can be feasible solutions to replace finite element method. However, they have limitations in maturity and popularity. Iso-geometric analysis is another option which unifies the CAD model and the analysis model through the spline information [Hughes et al. 2005]. It is promising, but also has the problem of immaturity and is not supported by the current commercial CAD/CAE systems.

From the authors' opinion, fixed grid finite element analysis (FGFEM) [Garcia-Ruiz and Steven 1998; Dunning et al. 2011] is the suitable method for CAD/CAE integrated design process. Eulerian mesh is applied and geometry conformity is not required. Therefore, the re-meshing effort is totally eliminated. On the other hand, FGFEM approximates the boundary crossed elements (BCEs) and the computation accuracy is reduced. To fix this issue, the extended finite element method (X-FEM) [Belytschko et al. 2003] was developed which enhanced the BCE modeling through local enrichment of the approximated spaces. It is effective in modeling local discontinuities, but requires the effort equivalent to local re-meshing, which is tedious for high-dimension and multi-boundary crossed cases. Therefore, to balance the computation accuracy and cost, a modified FGFEM is developed in this research, and details will be presented in Chapter 5.

(3) Concerning the BC attachment, it is not difficult to perform this manually but it is time consuming. However, it is non-trivial to automatically update the BC if topological changes happen to BC attached faces [Xia et al. 2015].

2.4.2 Inverse integration

For inverse integration, the simulation result must be analyzed and accordingly decide the design changes. The preliminary way to fulfill these obligations is to rely on expert knowledge and make human interpretation, with which the overall design process belongs to the trial and error method.

Another way to fulfill these obligations is to use the surrogate modeling based optimization. Park and Dang [2010] applied the response surface and radial basis function to build the surrogate models between optimization objective and design variables. A CAD/CAE integrated framework was developed to automate the surrogate modeling process, and the sequential quadratic programming method was used to find the optimal solution. Wang et al. [2014] implemented the improved sequential approximation optimization algorithm under the CAD/CAE integrated framework to find the structural optima. In these works, automation of the inverse integration is realized, but there are major limitations that: the efficiency and accuracy heavily depend on the specific surrogate modeling method, and it is mainly applicable to sizing optimization because of the scale limitation of design variables.

From the authors' opinion, sensitivity analysis based optimization methods are more appropriate to realize the inverse integration.

In early research, finite difference is widely used for sensitivity analysis for the sake of simplicity. Hardee et al. [1999] developed a CAD based shape optimization method. Shape parameters of the CAD model were applied as design variables and finite difference method was applied to calculate the sensitivity result. This method was successfully implemented by interfacing Pro/ENGINEER and a few CAE software tools. Grindeanu et al. [2002] developed a similar CAD based method, where both meshfree analysis and finite element analysis were applicable to support the finite difference sensitivity calculation. Vaidya et al. [2006] implemented the CAD based design optimization by sequentially optimizing the topology and

the shape. Manual transition was required between the two sub-procedures, and the shape optimization was performed similar to [Hardee et al. 1999].

Later, the adjoint sensitivity analysis is becoming popular, because it is computationally efficient as it requires only one-time finite element analysis in each optimization loop. For instance, in [Robinson et al. 2012], the authors developed the adjoint sensitivities for parameterized CAD geometries.

The adjoint sensitivity was initially developed for fluid-structure interacted problems, such as the air foil design, given the computationally expensive Navier-Stokes solution. Yu et al. [2011] extracted the NURBS surface information from the B-rep (Boundary representation) model and applied the control points as design variables. Adjoint sensitivity analysis was performed to update the control point positions. Later, they modified the optimization scheme by adding constraints to maintain the geometric relationships between NURBS surface patches [Xu et al. 2014].

For the aforementioned works, they stay at the level of sizing and shape optimization. However, it is not sufficient to fully demonstrate the capability of CAD/CAE integrated design, for the lack of topological changes. In fact, it has been a long-lasting issue of realizing topology optimization under the CAD/CAE integrated environment. For SIMP and ESO methods, discrete and staggered topological design is produced which requires a tedious process to be post-treated into a feasible CAD model [Hsu and Hsu 2005]. For the level set method, the implicit boundary representation and the CSG (Constructive Solid Geometry) geometry [Chen et al. 2007, 2008a] are not well supported by the B-rep dominated CAD systems. It is also very tedious to translate the CSG model into B-rep format, especially given the freeform nature (See Fig. 2.7). In summary, topology optimization is a CAE supported inverse design method, but there is a big gap to synchronize the CAD/CAE models.

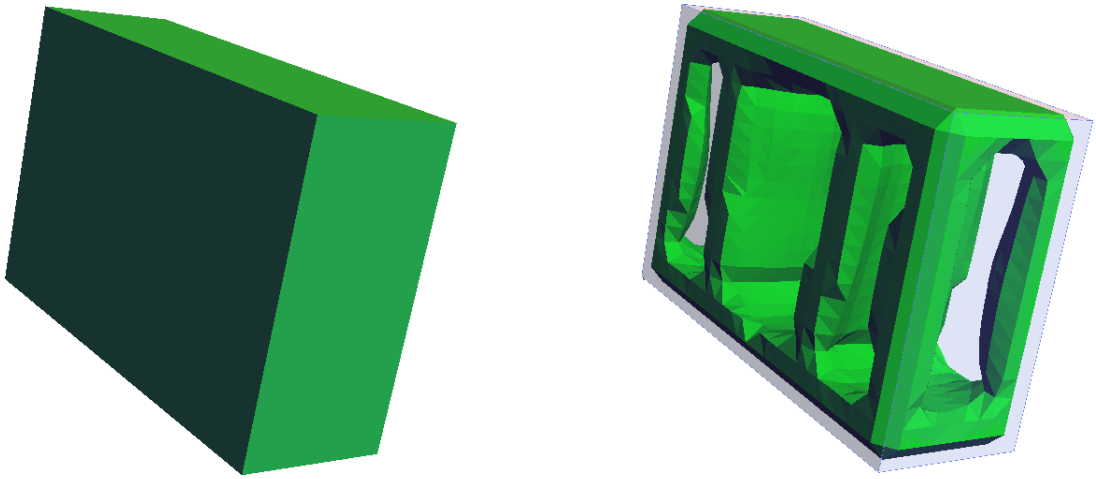

(a) Solid model (b) Freeform topological design

Fig. 2.7 Freeform shape and topological changes of the solid model

To fill the gap, one promising approach is the isogeometric analysis based shape [Wall et al. 2008] and topological [Seo et al. 2010a, 2010b] optimization methods. It is completely performed under the CAD/CAE integrated environment. However, as mentioned earlier, it has the limitations of being immature and less popular, and is not well supported by the current CAD/CAE systems.

Another promising approach is to develop the B-rep geometry based topology optimization method. B-rep geometry modeling is the foundation of most CAD systems. Therefore, if the analysis model and all topological changes are represented in B-rep format, the synchronization could be greatly eased. Hence, it is expected to perform the topological changes in the manner of conventional CAD modeling operations (such as drafting and extrusion), and record the topological changes to form the feature modeling history. Additionally, B-rep geometry based topological and shape sensitivity analysis is also indispensable for the inverse process automation. It is noted that development of B-rep geometry based topology optimization is a contribution of this research, and details will be presented in Chapter 5.

2.5 Multi-material topology optimization

Currently, multi-material topology optimization is an active research domain as it allows more design freedoms compared to homogeneous design. Furthermore, due to the advancement of

manufacturing methods, most of the multi-material designs are manufacturable within a reasonable cost.

In [Sigmund and Torquato 1997; Gibiansky and Sigmund 2000], the authors used the SIMP method to design two-material microstructures pursuing extreme physical properties. Later, Sigmund [2001] extended the method to design multi-physics actuators with two material phases. Bendsoe and Sigmund [1999] summarized the rule of multi-material interpolation in SIMP method. The general method of two-material interpolation is to assign two design variables to each finite element: one ($\rho^e{}_1$) determines the solid material ratio in the element, while the other ($\rho^e{}_2$) determines the material composition ratio of material 1. For instance, the element elasticity tensor is defined as,

$$\boldsymbol{D}(\rho^e) = \left(\rho^e{}_1\right)^p [\left(\rho^e{}_2\right)^p \boldsymbol{D}^1 + \left(1 - \rho^e{}_2\right)^p \boldsymbol{D}^2] \tag{2.10}$$

in which $\boldsymbol{D}^1$ and $\boldsymbol{D}^2$ are the elasticity tensors of material 1 and 2 respectively; p is the penalization term. Hvejsel and Lund [2011] generalized the SIMP method to make it applicable to interpolate any number of predefined materials with isotropic or anisotropic properties. Luo and Kang [2013] used the SIMP method to design steel-reinforced concrete structures by solving the strength constrained two-material topology optimization problem.

Additionally, Lund and Stegmann [2005] and Stegmann and Lund [2005] developed the discrete material optimization (DMO) method to optimize the discrete material selection of laminated composite structures, which offers a new material interpolation scheme, as,

$$\boldsymbol{D}(\rho^e) = \left(\rho^e{}_1\right)^p [1 - \left(\rho^e{}_2\right)^p] \boldsymbol{D}^1 + \left(\rho^e{}_2\right)^p [1 - \left(\rho^e{}_1\right)^p] \boldsymbol{D}^2 \tag{2.11}$$

Lund [2009] applied the DMO method to design multi-material shell laminates by solving the buckling topology optimization problem. Gao and Zhang [2011] compared the SIMP and DMO interpolation schemes through solving mass constrained multi-material topology optimization problems. Ferreira et al. [2014] developed a two-scale optimization scheme, with the DMO method to optimize the fiber fractions and orientations, and surrogate modeling to optimize the fiber sizes and shapes.

The level set method is a new rising and powerful approach addressing multi-material topology optimization problems. Wang and Wang [2004] developed the 'color' level set method to solve the compliance-minimization problems involving multiple materials; the advantage of this method is that, it only requires m level set functions to represent $n = 2^m$ material phases. Mei and Wang [2004] demonstrated a similar idea to perform multi-material topology optimization. Later, this method was used to design multi-material compliant mechanisms [Wang et al. 2005], and was generalized to design and optimize heterogeneous objects [Wang and Wang 2005]. Additionally, multi-material heat conduction problems [Zhuang et al. 2010a] and stress-related problems [Guo et al. 2014c] were also solved under this theoretical framework. In [Allaire et al. 2014a], the authors gave a more rigorous shape derivative to multi-material topology optimization problems. Vermaak et al. [2014] explored the influence of continuous material property change between material phases. Other than the 'color' level set method, Xia and Wang [2008] developed the numerical approach to solve topology optimization problems with functionally graded materials. Very recently, Wang et al. [2015] proposed a new Multi-Material Level Set (MMLS) scheme, which represents $m + 1$ material phases by m level set functions; this method guaranteed no redundant material phases, but may have efficiency issue with a large number of material phases.

In summary of the methods reviewed above, they have been extensively applied in multi-material design of solid structures and discrete fiber orientation design of composite laminates; however, there are even broader application scopes which have rarely been investigated. In this research, the novel pipeline opening layout design is investigated by using the multi-material level set topology optimization method. It is named 'multi-material' because for each shell element, it is either homogeneous or contains the opening which leads to distinguished element elasticity properties. By applying the level set method, the design process is automated and the result optimality is ensured, which demonstrates obvious advantages compared to the conventional trial and error method.

2.6 Shell topology optimization

Most topology optimization research efforts have been spent on 2D planar and 3D solid models, while shell models are less commonly explored. Therefore, this section summarizes research efforts on shell topology optimization.

Luo and Gea [1998] developed a procedural method to design the stiffened shell structure, in which the stiffener area was designed through topology optimization and then the exact stiffeners were identified through the orientation optimization. Li et al. [1999] extended EXO method to design shell structures subjected to thermal loading. Lee et al. [2000] applied SIMP method to address shell topology optimization by considering multi-layer shell models. Belblidia and Bulman (2002) developed a hybrid SIMP and ESO method to design shell structures under both static and vibrating conditions. Afonso et al. [2005] applied an integrated and procedural topology and sizing optimization process to design the stiffeners of the shell structure; similar to [Luo and Gea 1998], the stiffener area was designed through topology optimization, but the exact stiffeners were manually identified and optimized of the sizes and positions. Victoria et al. [2014] explored the influence of membrane thickness in the stiffened shell topology optimization. In summary of these works, it is effective to topologically optimize the shell structures, but it is not mature of the stiffener design. The optimized stiffeners are far from the practical strip-like shapes and they are post-processed into the strip-like designs through major approximations. In fact, thickness control techniques [Chen et al. 2008b; Luo et al. 2008a; Liu et al. 2015] could be applied to eliminate the post-processing.

In [Ansola et al. 2002], the authors proposed an integrated shape and topology optimization method, for which B-spline control points were used as shape optimization variables and local micro-structure parameters of the rank-2 layered material were applied as the topology optimization variables. Later, the authors [Ansola et al. 2004] made change to the micro-structure of the rank-2 layered material and applied this method to the integrated shape and reinforcement layout optimization. It is noticed that Ansola et al. [2002; 2004] applied a procedural method which optimized the shell shape first and then the topology. Distinctively, Hassani et al. [2013] developed a concurrent shape and topology optimization method for shell structures. NURBS (Non Uniform Rational B-Spline) surface was applied to model the shell structure and the control points were used as the shape optimization variables. SIMP method was applied to optimize the topology.

Shell topology optimization has rarely been performed based on the level set method. For the exception, Park and Youn et al. [2008] developed an adaptive inner-front level set method applied to shell structures, which features the hole digging capability.

In summary of the shell topology optimization methods, they mainly focus on the single-layer topology optimization and the multi-layer stiffener design; however, the single-layer multi-material topology optimization is rarely investigated. One reason of this status is the limited application scope of the single-layer multi-material shell structures. In this research, the pipeline opening layout design is innovatively transformed into a single-layer multi-material topology optimization problem, and it is solved by applying the multi-material level set method.

2.7 Limitations of the existing methods

At the end of this literature review chapter, limitations of the existing methods are summarized below:

(1) Limited connection between topology optimization and feature-based design

Currently, topology optimization and feature-based design are two standalone design schemes under the common umbrella of engineering informatics. It is non-trivial to build the connection for two reasons. First, as reviewed in Section 2.3, geometry feature-based topology optimization methods are not well-developed, including both implicit and explicit feature-based approaches. This means that, at most times, the topology optimization result needs to be manually post-treated into a geometry feature-based model. This manual post-treatment would definitely compromise the structural performance. Second, topology optimization usually focuses on geometry design, while the feature-attached semantic information is rarely involved, which again causes a post-treatment procedure. For instance, although topology optimization could produce a manufacturable design, it must be modified in the CAD/CAM system to reduce manufacturing time and cost.

(2) Limited application to address multidisciplinary design problems

Topology optimization is applicable in a variety of engineering fields. However, for most of them, certain adaption of the topology optimization algorithm is required, and it could be very challenging like in the case of the slotted liner design. In the research community, most researchers focus on improving the algorithm's efficiency and stability, while there is a lack of efforts in popularizing the topology optimization method in industry.

(3) Limited development of the two-scale extension

Many engineering problems involve two scales of material distribution: the macro-scale structural design and the micro-scale local material composition. A typical case is the fiber-reinforced plastic part. However, there is only limited development of the two-scale topology optimization, especially under the level set framework.

In summary, the aforementioned limitations clearly exist in the existing methods of level set topology optimization, and they are going to be addressed in this thesis.

2.8 Research objectives

Limitations of the existing methods have been identified in the last section, and accordingly, the research objectives are proposed in this section as follows:

- Development of the implicit feature-based level set topology optimization method to realize uniform rib thickness (Chapter 3);
- Development of the explicit feature-based level set topology optimization method and apply it to 2.5D machining parts (Chapter 4);
- Development of the B-rep geometry based topology optimization method and use it to support the CAD/CAE integration (Chapter 5);
- Proposing the OFM scheme for some trial applications (Chapter 6);
- Working-out the two-scale extension of the level set method and applying it to design fiber-reinforced plastic parts (Chapter 7); and
- Extension of the level set method to the slotted liner case used in oil industry (Chapter 8).

Chapter 3 Implicit feature-based level set topology optimization

3.1 Introduction

An implicit feature means that a geometry approximated approaching certain geometric pattern without explicit sizing or shape control parameters. An example was presented in Fig. 2.4. It is significant to develop a method for implicit feature control that the modified level set algorithm follows the freeform nature of the discretized geometry representation, and at the same time realizes satisfactory geometry control which makes the post-processing of the topological design into an explicit feature-based solution much more convenient.

In this chapter, certain parts demanding constant rib thickness control are studied. As reviewed in Chapter 2, the rib thickness control can be meaningful in several aspects. For machining parts, it can be applied to control the minimum component size for good cutting stability; additionally, it can also be applied to control the minimum void size which guarantees the machinability given the available cutting tools. For plastic parts that are commonly produced by injection molding, it is even more significant to have the constant rib thickness control because the constant rib thickness facilitates the cooling balance, and therefore reduces the thermal residual stress and the induced part defects.

3.2 Compliance minimization problem

The constant rib thickness control has been implemented based on the popular method to solve compliance minimization problem [Wang et al. 2003; Allaire et al. 2004]. Therefore, hereafter in this section, the level set topology optimization for compliance minimization is introduced in detail.

3.2.1 Problem formulation

A general compliance minimization problem could be formulated as:

$$Min. \quad J(\boldsymbol{u}, \Phi) = \int_D \boldsymbol{De}(\boldsymbol{u})\boldsymbol{e}(\boldsymbol{u})H(\Phi)d\Omega$$

$$s.t. \quad a(\boldsymbol{u}, \boldsymbol{v}, \Phi) = l(\boldsymbol{v}, \Phi), \qquad \forall \boldsymbol{v} \in U$$

$$\int_D H(\Phi)d\Omega \leq V_{max} \tag{3.1}$$

$$a(\boldsymbol{u}, \boldsymbol{v}, \Phi) = \int_D \boldsymbol{De}(\boldsymbol{u})\boldsymbol{e}(\boldsymbol{v})H(\Phi)d\Omega$$

$$l(\boldsymbol{v}, \Phi) = \int_D \boldsymbol{pv}H(\Phi)d\Omega + \int_D \boldsymbol{\tau v}\delta(\Phi)|\nabla\Phi|d\Omega$$

and this is a repeat of Eq. (2.2).

To conveniently apply the level set function into the optimization process, the Heaviside function and Dirac delta function are adopted as,

$$\begin{cases} H(\Phi) = 1, & \Phi \geq 0 \\ H(\Phi) = 0, & \Phi < 0 \end{cases} \tag{3.2}$$

$$\delta(\Phi) = \frac{\partial H(\Phi)}{\partial \Phi}, \quad \int_{-\infty}^{+\infty} \delta(\Phi)d\Phi = 1 \tag{3.3}$$

Then, the interior and boundary of the material domain can be represented by,

$$\Omega = \{\boldsymbol{X} \mid H(\Phi(\boldsymbol{X})) = 1\} \tag{3.4}$$

$$\partial\Omega = \{\boldsymbol{X} \mid \delta(\Phi(\boldsymbol{X})) > 0\} \tag{3.5}$$

Normally, the approximated Heaviside and Dirac delta functions are preferred in numerical implementation [Wang et al. 2003; Wang and Wang 2005].

3.2.2 Sensitivity analysis

To solve the optimization problem, a sensitivity analysis is needed to derive the boundary velocity V_n which evolves the structure in the steepest descent direction. The material derivative and the adjoint method are employed to perform the sensitivity analysis.

The Lagrange function is defined as,

$$L = J(\boldsymbol{u}, \Phi) + a(\boldsymbol{u}, \boldsymbol{w}, \Phi) - l(\boldsymbol{w}, \Phi) + \lambda(\int_D H(\Phi) d\Omega - V_{max}) \tag{3.6}$$

where λ is the Lagrange multiplier and $\boldsymbol{w}$ is the adjoint displacement field.

Material derivative of the Lagrange formulation is given as,

$$L' = J'(\boldsymbol{u}, \Phi) + a'(\boldsymbol{u}, \boldsymbol{w}, \Phi) - l'(\boldsymbol{w}, \Phi) + \lambda(\int_D H(\Phi) d\Omega)' \tag{3.7}$$

in which,

$$J'(\boldsymbol{u}, \Phi) = \int_D 2\boldsymbol{Ae}(\boldsymbol{u})\boldsymbol{e}(\boldsymbol{u}')H(\Phi) d\Omega + \int_D \boldsymbol{Ae}(\boldsymbol{u})\boldsymbol{e}(\boldsymbol{u})\delta(\Phi)V_n|\nabla\Phi| d\Omega \tag{3.8}$$

$$\begin{aligned} a'(\boldsymbol{u}, \boldsymbol{w}, \Phi) = &\int_D \boldsymbol{Ae}(\boldsymbol{u}')\boldsymbol{e}(\boldsymbol{w})H(\Phi) d\Omega + \int_D \boldsymbol{Ae}(\boldsymbol{u})\boldsymbol{e}(\boldsymbol{w}')H(\Phi) d\Omega \\ &+ \int_D \boldsymbol{Ae}(\boldsymbol{u})\boldsymbol{e}(\boldsymbol{w})\delta(\Phi)V_n|\nabla\Phi| d\Omega \end{aligned} \tag{3.9}$$

$$\begin{aligned} l'(\boldsymbol{w}, \Phi) = &\int_D \boldsymbol{p}\boldsymbol{w}'H(\Phi) d\Omega + \int_D [\boldsymbol{p}\boldsymbol{v} - \boldsymbol{\tau}\boldsymbol{w}\nabla \cdot (\frac{\nabla\Phi}{|\nabla\Phi|})]\delta(\Phi)V_n|\nabla\Phi| d\Omega \\ &+ \int_D \boldsymbol{\tau}\boldsymbol{w}'\delta(\Phi)|\nabla\Phi| d\Omega \end{aligned} \tag{3.10}$$

$$\lambda\left(\int_D H(\Phi) d\Omega\right)' = \lambda \int_D \delta(\Phi)V_n|\nabla\Phi| d\Omega \tag{3.11}$$

Substitute equations (3.8-3.11) into Eq. (3.7). Collect all the terms including $\boldsymbol{w}'$, and the sum is shown in Eq. (3.12) which is naturally equal to zero.

$$\int_\Omega [\boldsymbol{Ae}(\boldsymbol{u})\boldsymbol{e}(\boldsymbol{w}') + \boldsymbol{p}\boldsymbol{w}']H(\Phi) dx - \int_D \boldsymbol{\tau}\boldsymbol{w}'\delta(\Phi)|\nabla\Phi| d\Omega = 0 \tag{3.12}$$

Then, collect the terms containing $\boldsymbol{u}'$ and make the sum equal to zero, that is,

$$\int_{\Omega} [2\boldsymbol{Ae}(\boldsymbol{u})\boldsymbol{e}(\boldsymbol{u}') + \boldsymbol{Ae}(\boldsymbol{u}')\boldsymbol{e}(\boldsymbol{w})]H(\Phi)dx = 0 \tag{3.13}$$

Through solving Eq. (3.13), the solution of the adjoint variable $\boldsymbol{w} = -2\boldsymbol{u}$ can be derived. By collecting the remaining terms, the following sensitivity analysis result is obtained,

$$\begin{gathered} L' = \int_{D} R\delta(\Phi)V_n|\nabla\Phi|d\Omega \\ R = -\boldsymbol{Ae}(\boldsymbol{u})\boldsymbol{e}(\boldsymbol{u}) + \lambda \end{gathered} \tag{3.14}$$

where R is called shape gradient density. Then, by following Eq. (3.15),

$$V_n = -R \tag{3.15}$$

L could be guaranteed to change in the descent direction, as shown in Eq. (3.16),

$$L' = \int_{D} -R^2\delta(\Phi)|\nabla\Phi|d\Omega \leq 0 \tag{3.16}$$

The design update procedures were introduced in Chapter 2, Section 2.1, and will not be repeated here.

3.2.3 Numerical implementation

The finite element analysis (FEA) is implemented on fixed quadrilateral/hexahedral mesh to solve the linear elastic problem. The artificial weak material is applied for voids by employing the elasticity tensor of $10^{-3}\boldsymbol{E}$, in order to avoid the singularity of the stiffness matrix.

In Eq. (3.14), the Lagrange multiplier is applied to address the volume constraint. It can be defined in multiple ways: applying fixed value [Allaire et al. 2004], calculating based on volume conservation [Wang et al. 2003], or using the bi-sectioning algorithm [Wang et al. 2007].

In this research, the Augmented Lagrange method [Guo et al. 2014c] is applied which adopts the Lagrange multiplier as,

$$\lambda_{k+1} = \lambda_k + \mu_k(\int_D H(\Phi)d\Omega - V_{max})$$
$$\mu_{k+1} = \alpha\mu_k \ \ where\ 0 < \alpha < 1 \tag{3.17}$$

3.3 Implicit feature control

As mentioned earlier, implicit feature-based LSTO could be implemented by employing either constraints or additional control functional. For constant rib-thickness design, the latter achieves better control effect. However, the only works from Chen et al. [2008b] and Luo et al. [2008a] employ the quadratic energy functional in the form of double-layer boundary integration, which is difficult in numerical implementation [Guo et al. 2014a]. Therefore, a new thickness control functional is developed.

3.3.1 Thickness-control functional

The proposed thickness-control functional is shown below:

$$D_T = \int_D \left\{\left[\left(\Phi(\boldsymbol{X}) - \frac{T}{2}\right)^+\right]^2 - \left[\left(\Phi(\boldsymbol{X}) - \frac{T}{2}\right)^-\right]^2\right\} H(\Phi)d\Omega \tag{3.18}$$

The optimization problem presented in Eq. (3.1) is adapted with the new objective function, as:

$$Min. \quad J(\boldsymbol{u}, \Phi) = \int_D \boldsymbol{Ae}(\boldsymbol{u})\boldsymbol{e}(\boldsymbol{u})H(\Phi)d\Omega + \mu D_T \tag{3.19}$$

in which μ is the weighting factor of the thickness-control functional and T is the targeted rib thickness.

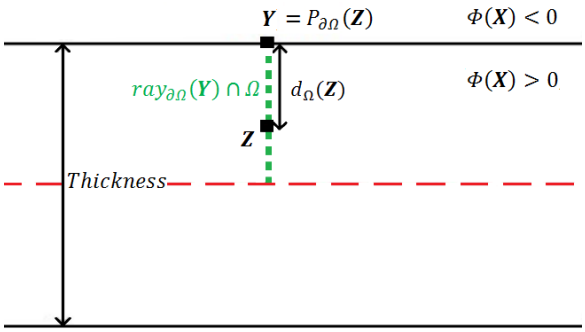

Fig. 3.1 Schematic plot of corollary 1

3.3.2 Sensitivity analysis on the thickness control functional

In order to prove its effect, sensitivity analysis on the level set function Φ is demonstrated.

Derivative of the thickness-control function on Φ is presented in Eq. (3.20)

$$D_T' = \int_D \left\{\left[\left(\Phi(\boldsymbol{X}) - \frac{T}{2}\right)^+\right]^2 - \left[\left(\Phi(\boldsymbol{X}) - \frac{T}{2}\right)^-\right]^2\right\}\delta(\Phi)V_n|\nabla\Phi|d\Omega$$
$$+ \int_D \left[2\left(\Phi(\boldsymbol{X}) - \frac{T}{2}\right)^+ - 2\left(\Phi(\boldsymbol{X}) - \frac{T}{2}\right)^-\right]H(\Phi)V_n|\nabla\Phi|d\Omega \tag{3.20}$$

In Eq. (3.20), the second term on the right side is field integration and needs to be transformed into boundary integration. As the basis of this transformation, a corollary is cited from [Allaire et al. 2014a]:

Corollary 1.

For a 2D integrable function $\phi(\boldsymbol{X})$ as demonstrated in Fig. 3.1,

$$\int_\Omega \phi(\boldsymbol{X})d\boldsymbol{X} = \int_{\partial\Omega}\left(\int_{\mathrm{ray}_{\partial\Omega}(\boldsymbol{Y})\cap\Omega} \phi(\boldsymbol{Z})(1 - d_\Omega(\boldsymbol{Z})\kappa(\boldsymbol{Y}))d\boldsymbol{Z}\right)d\boldsymbol{Y} \tag{3.21}$$

Two definitions are needed to interpret this corollary.

Definition 1.

For any $\boldsymbol{X} \in R^n, \Pi_{\partial\Omega}(\boldsymbol{X}) \coloneqq \{\boldsymbol{Y}_0 \in \partial\Omega, |\boldsymbol{X} - \boldsymbol{Y}_0| = inf_{\boldsymbol{Y}\in\partial\Omega}|\boldsymbol{X} - \boldsymbol{Y}|\}$ is the set of projections of $\boldsymbol{X}$ on $\partial\Omega$. When $\Pi_{\partial\Omega}(\boldsymbol{X})$ reduces to a single point, it is called the projection $P_{\partial\Omega}(\boldsymbol{X})$ of $\boldsymbol{X}$ onto $\partial\Omega$.

Definition 2.

For any $\boldsymbol{Y} \in \partial\Omega$, $ray_{\partial\Omega}(\boldsymbol{Y}) \coloneqq \{\boldsymbol{Z} \in R^n, d_\Omega \; is \; differentiable \; at \; \boldsymbol{Z} \; and \; P_{\partial\Omega}(\boldsymbol{Z}) = \boldsymbol{Y}\}$ is the ray emerging from $\boldsymbol{Y}$.

In Corollary 1, $d_\Omega(\boldsymbol{Z})$ represents the signed distance function which is equal to $\phi(\boldsymbol{Z})$ in case of Eq. (3.21) satisfied. By applying Corollary 1, the sensitivity analysis is adapted into:

$$D_T{}' = \int_D G\delta(\Phi)V_n|\nabla\Phi|d\boldsymbol{X}$$

$$G = \left[\left(\Phi(\boldsymbol{X}) - \frac{T}{2}\right)^+\right]^2 - \left[\left(\Phi(\boldsymbol{X}) - \frac{T}{2}\right)^-\right]^2 \tag{3.22}$$

$$+ \int_{ray_{\partial\Omega}(\boldsymbol{Y})\cap\Omega} \left[2\left(\Phi(\boldsymbol{Z}) - \frac{T}{2}\right)^+ - 2\left(\Phi(\boldsymbol{Z}) - \frac{T}{2}\right)^-\right]\left(1 - d_\Omega(\boldsymbol{Z})\kappa(\boldsymbol{Y})\right)d\boldsymbol{Z}$$

$\boldsymbol{Y}$ is the boundary projection point of $\boldsymbol{X}$, and $\boldsymbol{Z}$ is the sample points on $ray_{\partial\Omega}(\boldsymbol{Y})$.

By defining:

$$V_n = -G \tag{3.23}$$

We can make sure D_T will change in a descent direction, as:

$$D_T{}' = \int_D -G^2\delta(\Phi)|\nabla\Phi|d\boldsymbol{X} \leq 0 \tag{3.24}$$

Once the sensitivity analysis is done, the result can be used to analyze the thickness control effect. For any rib-like structure, there will be double-sided boundary movements all together influencing the rib thickness variation. It can be assumed that the curvatures at the double sides employ similar values but different signs. Therefore, the item including κ in Eq. (3.27) can be eliminated, which is adapted into:

$$G = \left[\left(\Phi(\boldsymbol{X}) - \frac{T}{2}\right)^{+}\right]^2 - \left[\left(\Phi(\boldsymbol{X}) - \frac{T}{2}\right)^{-}\right]^2 + \int_{ray_{\partial\Omega}(\boldsymbol{Y})\cap\Omega} \left[2\left(\Phi(\boldsymbol{Z}) - \frac{T}{2}\right)^{+} - 2\left(\Phi(\boldsymbol{Z}) - \frac{T}{2}\right)^{-}\right] d\boldsymbol{Z} \tag{3.25}$$

From Eq. (3.25), it can be concluded that the thickness could be controlled around T, because $G < 0$ can be guaranteed when the actual thickness is smaller than T, which makes the rib expand; while $G > 0$ is the case when the actual thickness is bigger than T, which makes the rib contract.

3.4 Case studies

To demonstrate the effectiveness of this thickness control functional, a few numerical examples are studied in this section.

3.4.1 Two-bar cantilever problem

First, a two-bar cantilever problem is studied. As shown in Fig. 3.2a, the design domain is of the size 50*100, with its left side fixed and a unit force loaded at the middle of its right side. The material has a Young's modulus of 1.3 and Poisson ratio of 0.4. The optimization problem is to minimize the compliance under a volume ratio constraint.

To sufficiently explore the thickness control effect, the algorithm has been performed with different T values of 6, 9 and 12, respectively. The results are shown in Fig. 3.2(b-e) and Table 3.1. Apparently, the thickness has been accurately controlled around the targeted values with very little tolerance, which is comparable with the effect presented previously in [Chen et al. 2008a].

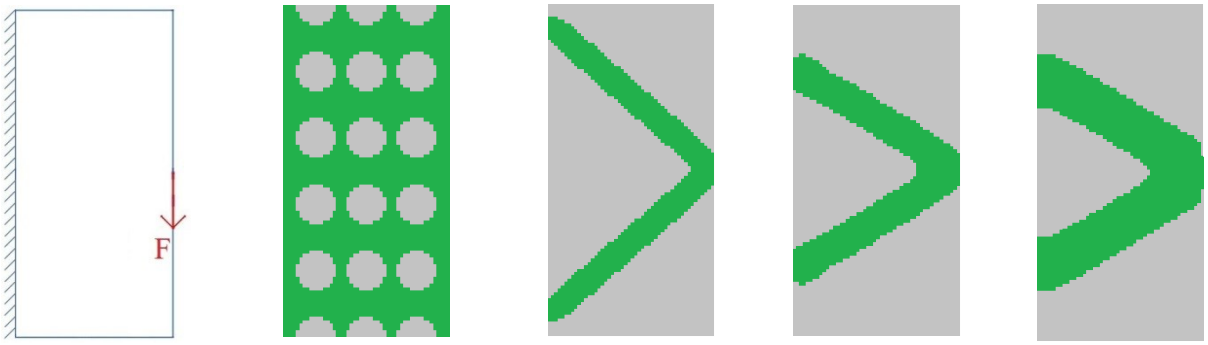

(a) Problem setup (b) The initial input (c) $T = 6$ (d) $T = 9$ (e) $T = 12$

Fig. 3.2 Results of the two-bar cantilever problem with different targeted thickness (a) Problem setup (b) The initial input (c) $T = 6$ (d) $T = 9$ (e) $T = 12$

Table 3.1 Data of the results of the two-bar cantilever problem

Targeted thickness	Compliance	Volume ratio
$T = 6$	8.7814	0.200
$T = 9$	9.2237	0.225
$T = 12$	7.0838	0.300

3.4.2 L-bracket problem

In Fig. 3.3, an L-bracket problem is demonstrated. The design domain size is 100*100. A point force is loaded on the right top and the top edge is fixed. It is assumed the material has a Young's modulus of 1.3 and Poisson's ratio of 0.4. Again, the optimization problem is to minimize the compliance under the volume ratios of 0.3125.

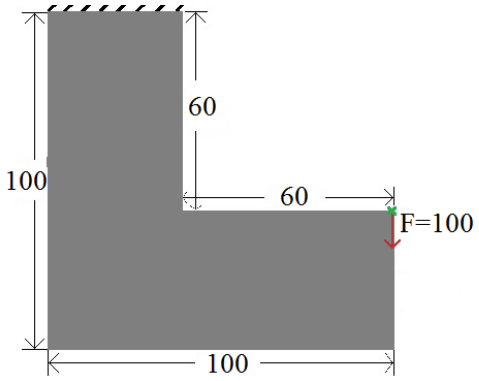

Fig. 3.3 L-bracket problem

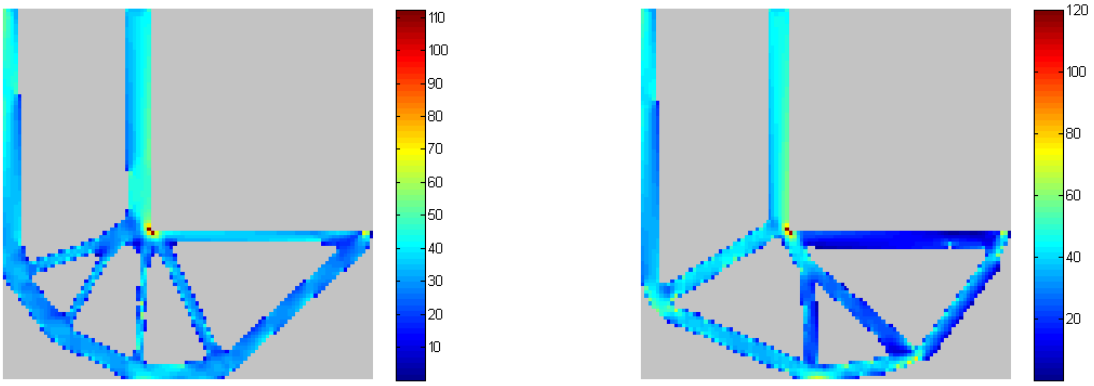

(a) Regular result without thickness control (b) Result with thickness control ($T = 5$)

Fig. 3.4 Results of the L-bracket problem (the color bar marks the von Mises stress level)

The optimization results are presented in Fig. 3.4. Fig. 3.4a shows the raw result without thickness control, while the result with thickness control is demonstrated in Fig. 3.4b. It is clear that, the thickness could be controlled around the pre-defined value with small tolerance, but there is a little sacrifice of the structural strength with the maximum local von Mises stress increased from around 110 to about 120. The thickness control may be necessary for improved manufacturability, e.g. injection molding part design, without sacrificing structural integrity.

3.5 Conclusion

Theoretically, the main contribution of this section is the new thickness control functional. With it equipped, the implicit feature-based level set topology optimization method has been proven

effective in deriving topological design of well-controlled rib thickness around a predefined value within reasonable tolerances.

For future work, improved thickness control effect is under exploration, especially for stress-constrained problems. Other implicit feature control types are also under investigation. In addition, implicit feature control is not adaptive to all geometry feature-based design problems. Therefore, the explicit feature-based approach is developed in the next chapter.

Chapter 4 Explicit feature-based level set topology optimization

4.1 Introduction

Chapter 3 presented the implicit feature-based level set topology optimization, which realizes the geometry feature control in an approximate manner. However, the design solution still needs to be post-processed into an explicit feature-based solution for the following detail design activities. In this chapter, an alternative approach is developed to directly perform the explicit feature-based level set topology optimization.

An explicit feature, in this context, means the geometry, defined by a set of geometrical entities, is intuitively constrained by sizing and shape parameters, and these parameters can be applied as optimization variables. An example was presented in Fig. 2.5. As reviewed in Section 2.3, there are several limitations of the current explicit feature-based level set topology optimization methods. For instance, new feature primitives can rarely be generated during the optimization process, the scale control capability is poor, and most of the methods are not proven effective in 3D schemes. Therefore, this new method is developed to overcome these limitations and will be presented in the rest of this chapter.

4.2 Velocity field

The common procedure of solving the level set topology optimization problem is to derive the virtual velocity field through sensitivity analysis, and then accordingly evolve the structural boundary. For the widely studied compliance minimization problem, the velocity field is presented in Eq. (4.1).

$$V_n = -(\lambda - \boldsymbol{De}(\boldsymbol{u})\boldsymbol{e}(\boldsymbol{u})) \tag{4.1}$$

Generally, the velocity field is composed of continuously varying velocities and lacks of regulation, which drives the topological design into 2D/3D freeform. The freeform design is not easy to manufacture and a post-processing step is normally required to manually re-construct the

design into explicit feature-based. This step is time-consuming and labor intensive, and more severely, it may unacceptably relax the objective function.

Therefore, it would be meaningful to train the velocity field into regulated patterns, and therefore, explicit feature primitives could be generated through design update while the freeform design is suppressed. Consequently, explicit feature-based design could be directly obtained without any post-processing effort. This would provide a substantial and novel improvement to topology optimization. In this chapter, this new method is implemented given the background of 2.5D machining.

4.3 Machining feature fitting algorithm

Machining feature is a domain-specific form of the explicit feature concept. The machining feature fitting algorithm developed in this work is inspired by feature-based model reconstruction in reverse engineering [Thompson et al. 1999; Rabbani and van den Heuvel 2004; Bi and Wang 2010; Wang et al. 2012], for which different methods have been developed to construct the feature-based models from scanned point cloud. Three major procedures (Fig. 4.1) – define feature library, make segmentation and solve the feature fitting problem – commonly exist in these methods. Specifically, the feature library includes the candidate feature primitives to be fitted in; segmentation is applied for the piecewise property of feature fitting, as mechanical components are normally composed of numerous feature primitives; then, the nonlinear least squares formulation is adopted to solve the segmented feature fitting problems as shown in Eq. (4.2).

$$min \quad f = \sum_{i} d(\boldsymbol{p_i}, \boldsymbol{s})^2 \tag{4.2}$$

where d is the shortest distance from $\boldsymbol{p_i}$ to the targeted feature surface, and $\boldsymbol{s}$ is the parameter set which uniquely determine the feature profile.

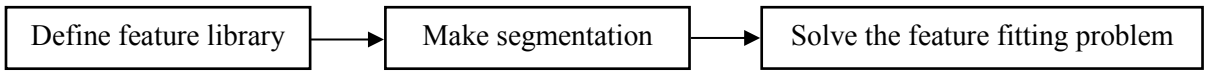

Fig. 4.1 Three common procedures of feature-based model reconstruction methods

In level set topology optimization, boundary velocity field is similar to the point cloud in reverse engineering, as both of them are structural boundary based and contain a large number of elements (velocities/points). Therefore, it is appropriate of level set topology optimization to inherit the procedures in Fig. 4.1 to train the velocity field into explicit feature-based patterns. Combined, we name these procedures the feature fitting algorithm.

Previously, in [Zhou and Wang, 2013], the authors applied least squares fitting to regulate the velocity field of existing feature primitives, in this way to realize the feature manipulations (movement, rotation, and scaling) with maintained shape characteristics. Comparatively, the feature fitting algorithm developed in this research is more advanced with the capability of generating new primitives during the optimization process, instead of only manipulating the existing ones.

4.3.1 2D features

2D features are involved because 2D topology optimization is popular and they can be applied to thin-plate structures.

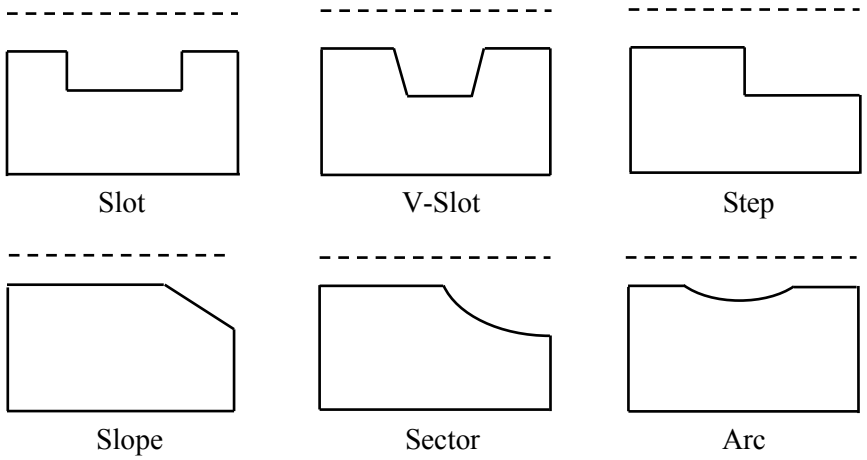

(a) Individual features

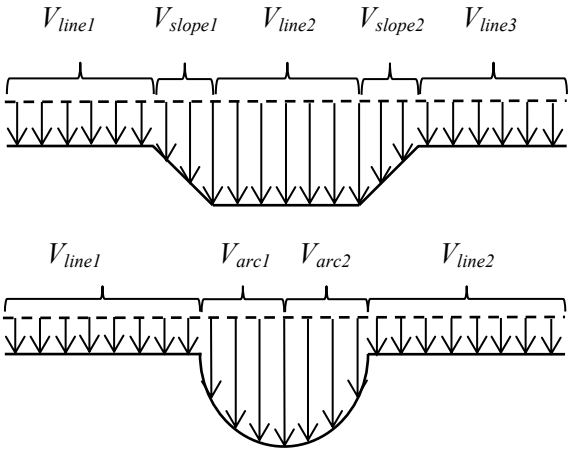

(b) Compound features

Fig. 4.2 2D machining feature library

There are different taxonomies for 2D machining features [Miao et al. 2002; Kang et al. 2014], in which numerous feature types have been defined. A few examples are illustrated in Fig. 4.2a. However, it would be ineffective to train the velocity field with the feature types separately. Therefore, two compound features – the compound slot feature and the compound arc feature – have been defined (see Fig. 4.2b), which can evolve into any specific example as shown in Fig. 4.2a through solving the feature fitting problem. Mathematically, velocity field of the compound features can be represented by Eq. (4.3-4.4).

$$V_{slot}(x) = \begin{cases} V_{line_1}(L_1, C_1) = C_1 \quad x \in [0, L_1) \\ V_{slope_1}(L_2) = C_1 + \dfrac{C_2 - C_1}{L_2 - L_1}(x - L_1) \quad x \in [L_1, L_2) \\ V_{line_2}(L_3, C_2) = C_2 \quad x \in [L_2, L_3) \\ V_{slope_2}(L_4) = C_2 + \dfrac{C_3 - C_2}{L_4 - L_3}(x - L_3) \quad x \in [L_3, L_4) \\ V_{line_3}(L_5, C_3) = C_3 \quad x \in [L_4, L_5] \end{cases} \tag{4.3}$$

$$\sum_{i=1}^{5} L_i = L$$

$$V_{arc}(x) = \begin{cases} V_{line_1}(C_1) = C_1 \quad x \in [0, \max(0, x_0 - R)] \\ V_{arc1}(x_0, y_0, R) = \max(C_1, \sqrt{R^2 - (x - x_0)^2} + y_0) \quad x \in (\max(0, x_0 - R), x_0) \\ V_{arc2}(x_0, y_0, R) = \max(C_2, \sqrt{R^2 - (x - x_0)^2} + y_0) \quad x \in [x_0, \min(x_0 + R, L)) \\ V_{line_2}(C_2) = C_2 \quad x[\min(x_0 + R, L), L] \end{cases} \tag{4.4}$$

$$x_0 \in (0, L)$$

In Eq. (4.3-4.4), C_1, C_2 and C_3 are constants representing the piecewise velocity magnitude; (x_0, y_0) and R are the center position and radius of the circle in the circular arc feature; L represents the total length of the linear boundary segment.

Boundary segmentation is significant because the feature fitting problems are solved on the basis of piecewise boundary segments. Therefore, different fitting results would be produced with different scales of segmentation. For instance, a linear boundary can be cut into numerous small segments and then each one is fitted with a 2D feature. In this way, the boundary evolvement can be tracked accurately. However, too many segments are definitely undesirable as they will bring numerous parameters to manage and create difficulties in manufacturing. Therefore, a proper scale of segmentation is important. In this work, the segments are recognized through natural boundary definitions; and a customized minimum length scale L_{lim} is employed to filter the small segments out of the fitting activities.

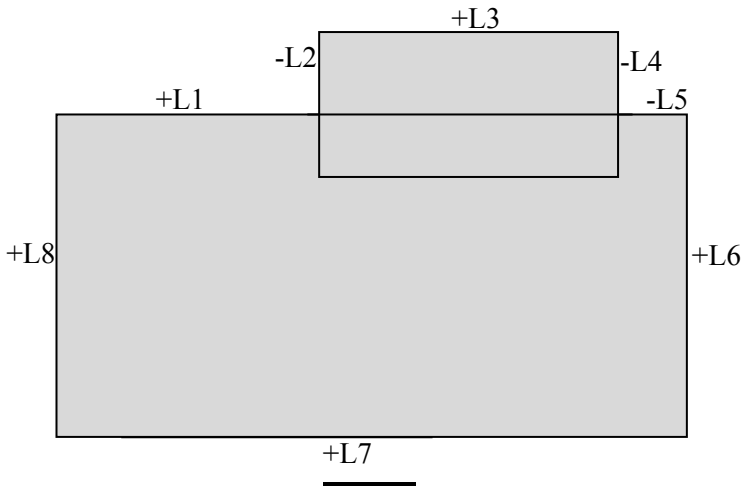

Fig. 4.3 Boundary segmentation ('+' means the length larger than L_{lim}; '-'means the length shorter than L_{lim})

As shown in Fig. 4.3, this algorithm divides the model boundary into 8 linear segments, and the length of each segment is calculated. The following feature fitting problems will only be solved on the segments employing the length larger than L_{lim}, for the purpose of scale control of the newly generated feature primitives.

After proper setup of the 2D feature library and the boundary segmentation, it is designed to apply the least squares formulation as shown in Eq. (4.5) to regulate the velocity distribution on each piecewise linear segment with the predefined compound feature velocity fields.

$$min \quad f = \int_0^L (V(x, \boldsymbol{s}) - V_n(x))^2 \, dx \tag{4.5}$$

Here $V_n(x)$ is the local normal velocity; $V(x, \mathbf{s})$ is the 1D feature velocity as demonstrated in Eq. (4.3-4.4), and $\boldsymbol{s}$ is the optimization variable vector. Because of the multiple candidate compound features, the feature fitting problem is finally formulated into a double-layer scheme as,

$$\begin{aligned} &min.\ (min.\ f_i \\ &by\ finding\ \boldsymbol{s_i})\ \ i = compound\ slot\ or\ compound\ arc \end{aligned} \tag{4.6}$$

In Eq. (4.6), the inner loop can be solved by finite difference method as the analytical expression is non-trivial to be obtained [Rabbani and van den Heuvel 2004], while the outer loop can be solved through direct comparison.

4.3.2 2.5D features

2.5D machining is a popular milling method which is greatly preferred by the manufacturing industry for its high efficiency and low cost. A clear classification of 2.5D machining features is proposed according to [Miao et al. 2002; Kang et al. 2014].

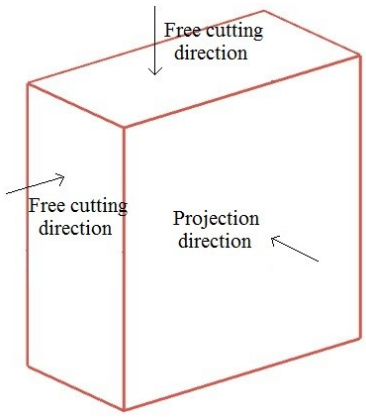

Fig. 4.4 Directions in the 2.5D milling process

(1) 2.5D form features

2.5D form features employ simple profiles composed of linear and/or circular segments, which are commonly applied in mechanical design. In Fig. 4.5, two sub-categories of 2.5D form features are demonstrated, which are categorized based on the fitting through the projection direction (Fig. 4.5a) or the free cutting directions (Fig. 4.5b).

(2) 2.5D freeform features

2.5D freeform features employ freeform profiles in the cutting directions. It is more complex but still can be handled by 2.5D machining. Detailed classification of 2.5D freeform features is similar to those demonstrated in Fig. 4.5a and 4.5b, and is shown in Fig. 4.5c.

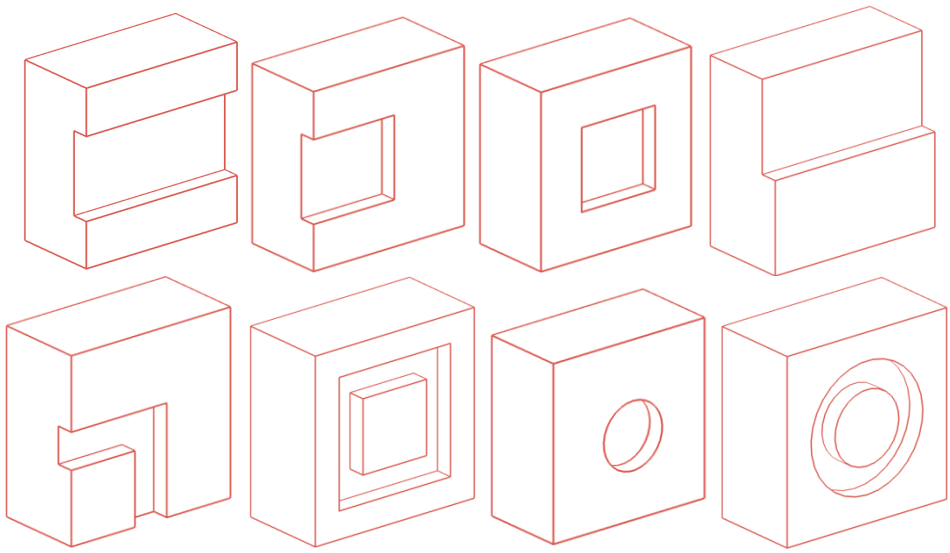

(a) 2.5D form features in the projection direction

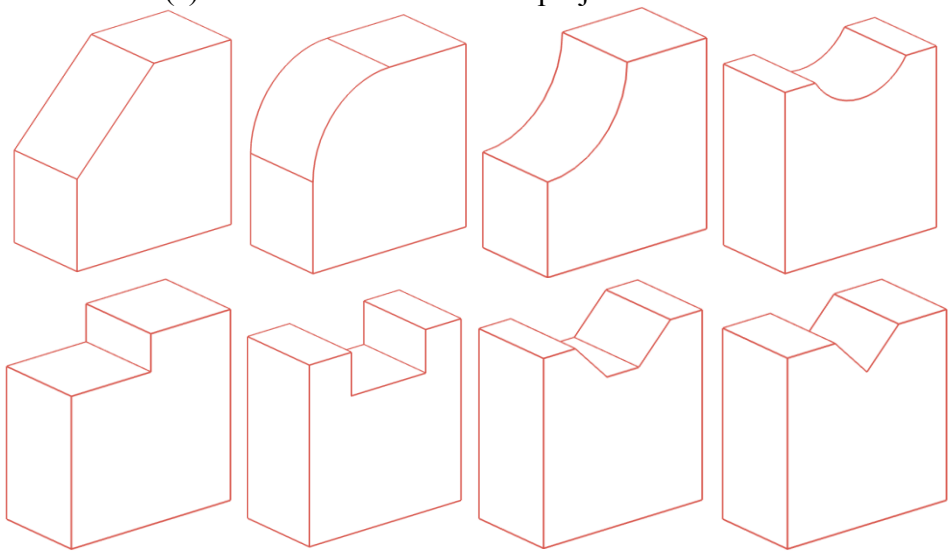

(b) 2.5D form features in the free cutting directions

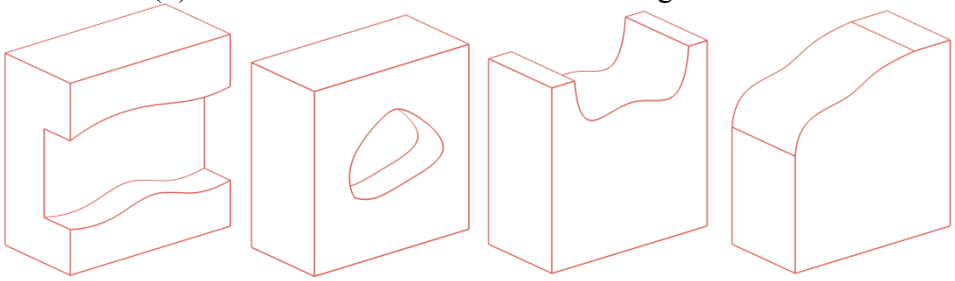

(c) 2.5D freeform features

Fig. 4.5 Classification of 2.5D features

Similar segmentation rules as demonstrated in the 2D scheme can be extended to 3D cases, but certain adaptations are needed. Details about the rules will be introduced in the next section because it is tightly connected to the construction method of the feature model.

With regards to the exact 2.5D feature fitting algorithm, the least squares formulation demonstrated in Eq. (4.5) needs to be extended with one more dimension as shown in Eq. (4.7).

$$min \quad f = \int_0^H \{\int_0^L (V(x,y,\boldsymbol{s}) - V_n(x,y))^2 \, dx\} dy \tag{4.7}$$

The feature fitting problem with 2.5D form features is still a double-layer optimization formulation as shown in Eq. (4.8), but different feature libraries will be applied for the projection direction and the free cutting directions. Through solving Eq. (4.8), the best fitted feature and its specifications (size, depth and orientation) for each feasible surface can be found. For instance, a fitting case with 2.5D form features in the projection direction is demonstrated in Fig. 4.6.

$$\begin{aligned} &min.\ (min.\ f_i \\ &by\ finding\ \boldsymbol{s_i})\ \ i = feature\ index \end{aligned} \tag{4.8}$$

As for 2.5D freeform features, the feature fitting problem is adapted into a one-layer optimization problem as shown in Eq. (4.9), because of the spline curves applied for the free contour representation.

$$\begin{aligned} &min.\ f \\ &by\ finding\ \boldsymbol{s}, which\ represents\ the\ set\ of\ control\ points \end{aligned} \tag{4.9}$$

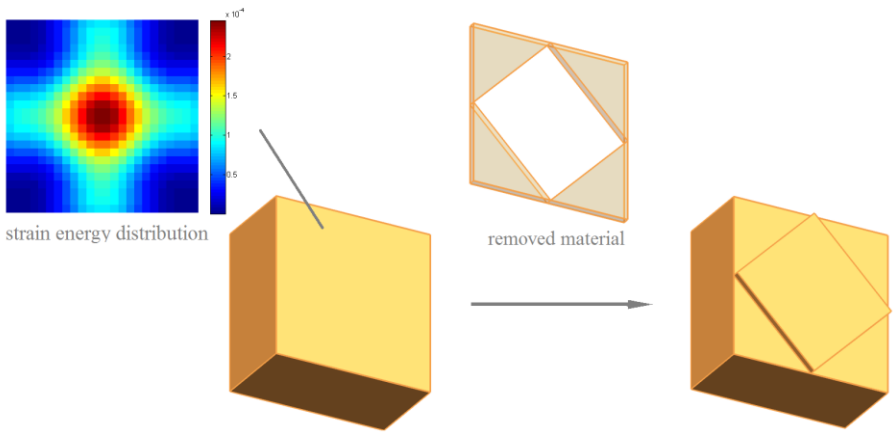

Fig. 4.6 A fitting case with 2.5D form features in the projection direction

Here, a major problem is to define the projection direction. The strategy applied in this work is to determine the surface employing the highest material removal rate (MRR) in the initial iteration, and define its normal direction as the projection direction. The reason lies in that the projection direction is normally the major cutting direction.

4.4 Explicit feature-based shape optimization

Apparently, the material domain after feature fitting is composed of explicit feature primitives, and can be easily transformed into a constructive feature model by R-functions to support the explicit feature-based shape optimization. In this way, further shape adjustments of the material domain can be achieved in a fast and robust iterative manner without relying on the velocity field.

4.4.1 Constructive feature model

In CAD systems, CSG and B-rep are two widely adopted geometry representation methods, while the latter is more general in commercial software tools. However, for shape and topology optimization, sensitivity analysis on the boundary representation requires the model to be isomorphic which severely influence the optimization capability [Chen et al. 2008a]. Comparatively, CSG format is insensitive to topological changes. Therefore, CSG is suitable to be the basis of explicit feature-based shape optimization.

To form the constructive feature model, explicit feature primitives are represented by parametric level set functions. For instance, a circle is represented by Eq. (4.10),

$$\Phi(\boldsymbol{X}) = R - |\boldsymbol{X} - \boldsymbol{X_0}| \tag{4.10}$$

in which R is the circle radius and $\boldsymbol{X_0}$ is the circle center.

On the other hand, the freeform profiles of the 2.5D features can also be implicitly represented. In this work, the 1-D Bezier curve is applied to represent the freeform profiles for the sake of simplicity [Xu and Ananthasuresh, 2003], for which the implicit representation is demonstrated in Eq. (4.11). Extension to more complex spline curves like B-spline is possible [Chen et al. 2007; Cai et al. 2014].

$$\begin{aligned} \Phi(x,y) &= (\sum_{i=0}^{n} B_{n,i}(t(x))Y_i) - y \\ B_{n,i}(t) &= \frac{n!}{i!\,(n-i)!} t^i (1-t)^{n-i} \\ t(x) &= \frac{x-K}{L} \quad x \in [K, K+L] \end{aligned} \tag{4.11}$$

The feature primitives ($\Phi_1(\boldsymbol{X}), \Phi_2(\boldsymbol{X}), \Phi_3(\boldsymbol{X})$ ... ...) are then combined together by R-functions to form new and complex geometry [Cai et al. 2014],

$$\begin{aligned} \Phi_1 \cup \Phi_2 &= max(\Phi_1, \Phi_2) \\ \Phi_1 \cap \Phi_2 &= min(\Phi_1, \Phi_2) \\ \Phi_1 \setminus \Phi_2 &= min(\Phi_1, -\Phi_2) \end{aligned} \tag{4.12}$$

In this sense, the integral level set function will be,

$$\Phi = C(\Phi_1, \Phi_2, \Phi_3, \dots\dots) \tag{4.13}$$

In Fig. 4.7, the integral level set function is formed by R-function as $\Phi = (\Phi_1 \cup \Phi_3) \setminus (\Phi_2 \cup \Phi_4)$.

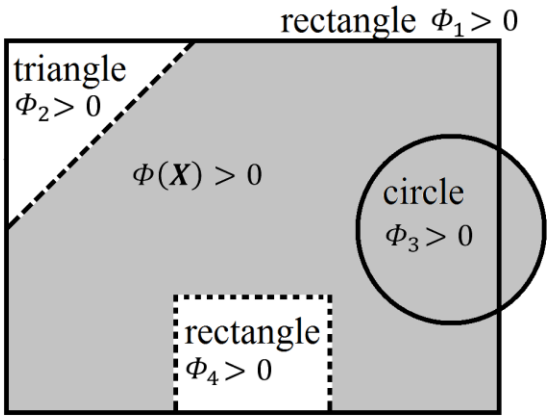

Fig. 4.7 Constructive feature model

So far, the constructive feature model has been introduced in details. Therefore, the boundary segmentation rules are presented here for its tight connection with the construction method.

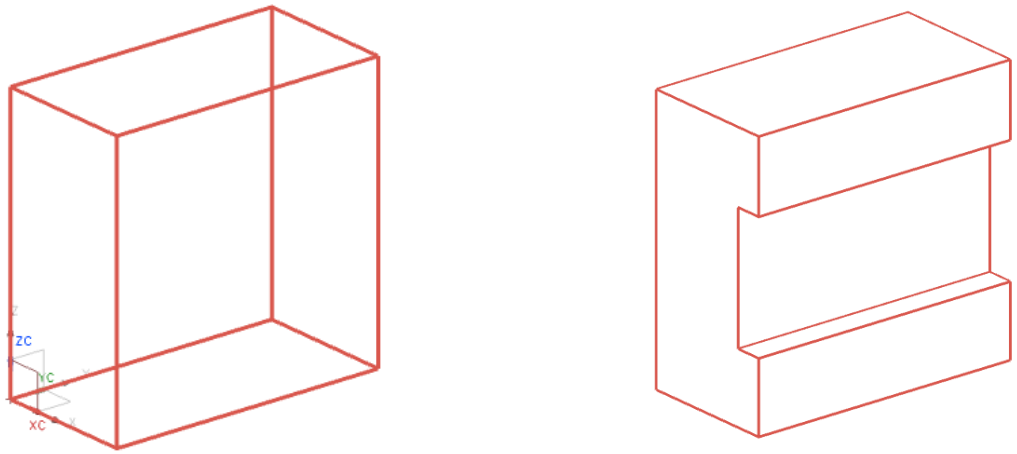

(a) (b)

Fig. 4.8 Boundary segmentation

As presented in Fig. 4.8a, the constructive feature model composed of only one primitive can be represented by:

$$\Phi(\boldsymbol{X}) = \Phi_1(\boldsymbol{X}) = min[\frac{L}{2} - (x - x_0), \frac{L}{2} + (x - x_0), \frac{W}{2} - (y - y_0), \frac{W}{2} + (y - y_0), \frac{H}{2} - (z - z_0), \frac{H}{2} + (z - z_0)] \quad (4.14)$$

in which L, W, H are the lengths in x, y, z directions, respectively; and (x_0, y_0, z_0) is the coordinate of the center point. Correspondingly, the front boundary segment in x direction is represented by:

$$\{\boldsymbol{X} | \frac{L}{2} - (x - x_0) = 0 \; and \; \Phi(\boldsymbol{X}) = 0\} \quad (4.15)$$

In Eq. (4.15), the last term is naturally satisfied, because $\Phi(\boldsymbol{X})$ is identical to $\Phi_1(\boldsymbol{X})$. However, it is significant to have the $\Phi(\boldsymbol{X}) = 0$ term in this representation, because only the overlapping boundaries between the feature primitive and the constructive feature model will be tracked as effective boundary segment for feature fitting.

If fit in another primitive Φ_2 to the front face in x direction as presented in Fig. 4.8b, the constructive level-set function will be:

$$\Phi(\boldsymbol{X}) = \Phi_1(\boldsymbol{X}) / \Phi_2(\boldsymbol{X}) \quad (4.16)$$

$$\Phi_2(\boldsymbol{X}) = min[\frac{L'}{2} - (x - x'_0), \frac{L'}{2} + (x - x'_0), \frac{W'}{2} - (y - y'_0), \frac{W'}{2} + (y - y'_0), \frac{H'}{2} - (z - z'_0), \frac{H'}{2} + (z - z'_0)] \quad (4.17)$$

Then, the front boundary segment of primitive Φ_1 in x direction is still tracked by Eq. (4.15), but the effective area has changed. The effective boundary segment of primitive Φ_2 is tracked by Eq. (4.18).

$$\{\boldsymbol{X} | [\frac{L'}{2} - (x - x'_0) = 0 \; or \; \frac{L'}{2} + (x - x'_0) = 0] \; and \; \Phi(\boldsymbol{X}) = 0\} \quad (4.18)$$

In this way, all effective boundary segments can be accurately tracked during optimization. Another point to be emphasized is that the orientation (projection direction, or one of the free cutting directions) of each created explicit feature primitive should be recorded. For each of the

primitive, only boundary segment perpendicular to the recorded orientation will be considered for further feature fitting.

As for the size of the boundary segment, it is determined by the number of included grid nodes.

4.4.2 Sensitivity analysis

Sensitivity analysis on the shape parameters or control points can be calculated by applying Eq. (4.19).

$$\frac{\partial p_j}{\partial t} = -\int_D R \frac{\partial \Phi}{\partial \Phi_i} \frac{\partial \Phi_i}{\partial p_j} \delta(\Phi) d\Omega \tag{4.19}$$

where p_j means the j^{th} shape parameter (control point) of shape (spline curve) i, and R is called the shape gradient density, as:

$$R = -\boldsymbol{De}(\boldsymbol{u})\boldsymbol{e}(\boldsymbol{u}) + \lambda \tag{4.20}$$

Details about the proof of Eq. (4.19-4.20) can refer to [Chen et al. 2007].

After sensitivity analysis, design update can be done parametrically (Eq. (4.21)) instead of solving the Hamilton-Jacobi Equation for velocity field based evolvement.

$$p_j = p_j + \frac{\partial p_j}{\partial t} * \Delta t \tag{4.21}$$

4.4 Numerical implementation details and procedures

The finite element analysis (FEA) is implemented on fixed quadrilateral/hexahedral mesh to solve the linear elastic problem. Again, artificial weak material is applied for voids in order to avoid the singularity of the stiffness matrix.

The volume constraint is satisfied by applying the Augmented Lagrange method.

As for the feature fitting algorithm, the customized length scale L_{lim} is applied in an increasing manner to save computational expense and to avoid the infinite loop. That is,

$$L_{lim}{}^{k+1} = \beta L_{lim}{}^{k}$$
$$\beta \geq 1 \tag{4.22}$$

In Fig. 4.9, the complete numerical implementation procedures are demonstrated, and the overall algorithm is illustrated step by step as below:

Step 1: Initialize the constructive feature model by defining the level set functions and the Boolean operations. Define the projection direction and the free cutting directions. Set the Lagrange multiplier λ, penalty factor μ, and the length scale L_{lim}.

Step 2: Perform finite element analysis to evaluate the deformation field.

Step 3: Make segmentation and measure the segment sizes.

Step 4: If there are segments eligible for feature fitting (size > L_{lim}), go to Step 4.1; otherwise, go to Step 4.2.

- Step 4.1. Solve the feature fitting problems on all eligible segments to fit in new feature primitives. Go to Step 5.
- Step 4.2. Perform parametric sensitivity analysis and update the feature primitives. Go to Step 5.

Step 5: Update the constructive feature model with either new feature primitives (if go through Step 4.1) or updated parameter values (if go through Step 4.2).

Step 6: Update of the Lagrange multiplier λ, penalty factor μ, and the length scale L_{lim}.

Step 7: Check if the termination condition is satisfied. If yes, then a convergent solution is found; otherwise, go through Step 2 to Step 6.

It should be noted that if L_{lim} is bigger than the maximum possible boundary segment size, the algorithm will ignore Step 3 and Step 4.1 in order to save computational effort.

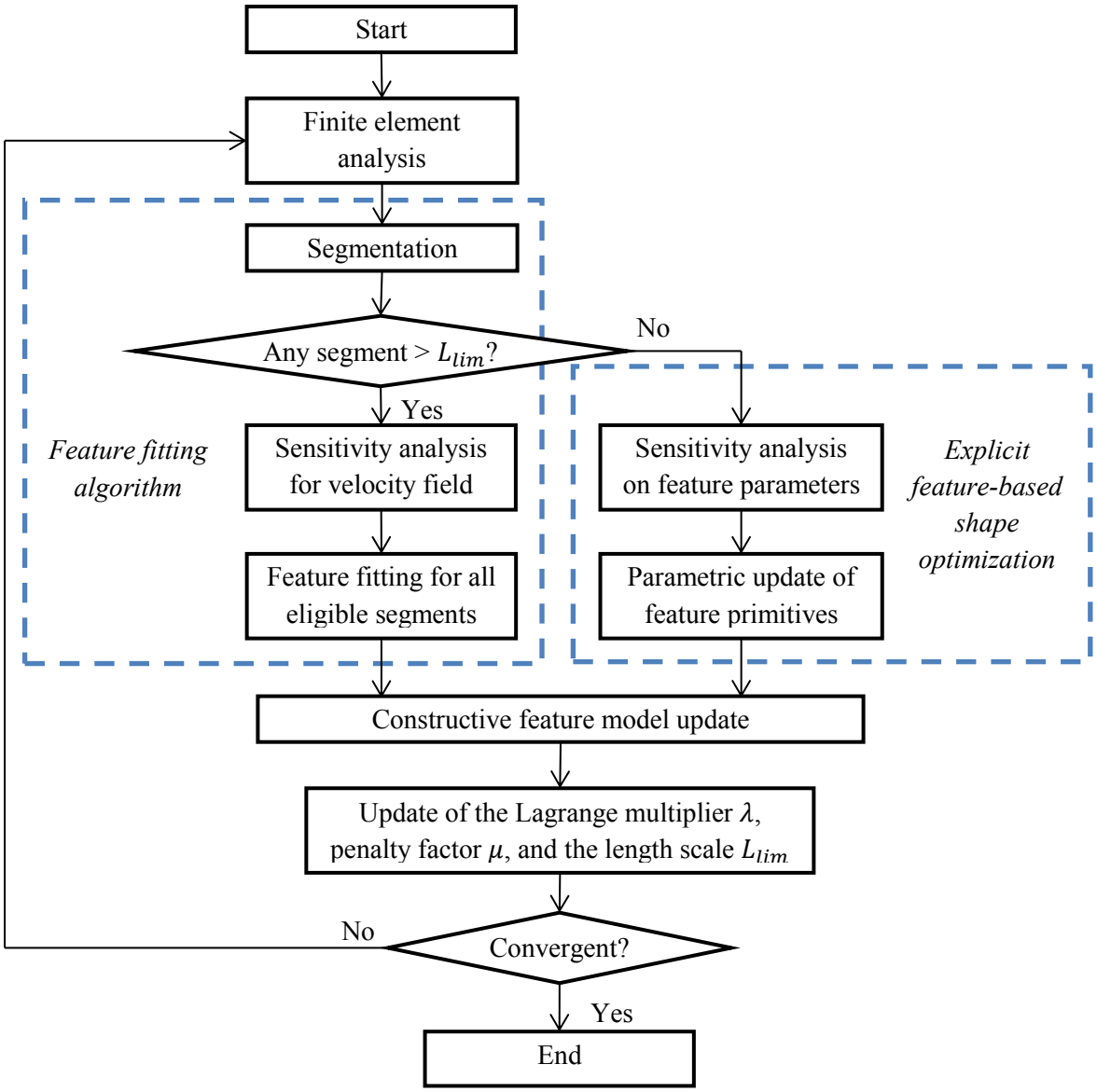

Fig. 4.9 Flowchart of the implementation procedures

4.5 Numerical examples

4.5.1 Short cantilever problem – the 2D case

The first case is about the short cantilever problem as shown in Fig. 4.10. The top and bottom of the left side are fixed and a vertical unit force pointing downward is loaded at the middle of the right side. The objective is to minimize the compliance with the maximum volume ratio of 0.4. Poisson ratio and Young's modulus are 0.3 and 1, respectively.

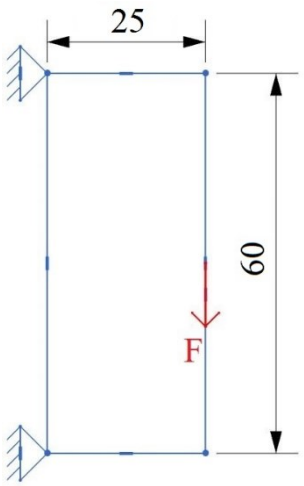

Fig. 4.10 Short cantilever problem in 2D

In order to determine the difference of adding the feature fitting algorithm into the optimization process, the regular level set approach and the machining feature-based approach with customized length scale L_{lim}=15 have been implemented. The optimization results are illustrated in Fig. 4.11.

In analysis of these two optimization processes, the regular level-set approach takes 107 iterations and adapts the design from Fig. 4.11a to Fig. 4.11b with the final objective of 7.3101. Then the machining feature-based approach takes 81 iterations, and the design follows the adaption path of a-c-e-f in Fig. 4.11, of which the objective ends at 7.5128. Through comparison of these two results, it can be concluded that the regular level set approach is able to reach the optimal objective but its design manufacturability is relatively low; while machining feature-based approach can achieve the desired design with great manufacturability.

An extra feature-based process with enlarged length scale L_{lim}=25 is tested in this case. This process adapts the design following the path of a-c-d in Fig. 4.11, and its final compliance is 8.7760 which is 20.29 percent higher than the optimum. Through this test, the significance of appropriately selecting the customized length scale is emphasized.

A similar case appeared earlier in [Mei et al. 2008]. Their result consists of many small feature primitives, for lack of scale control capability. Consequently, manufacturability is still problematic unless adopting the post-treatment of boundary smoothing.

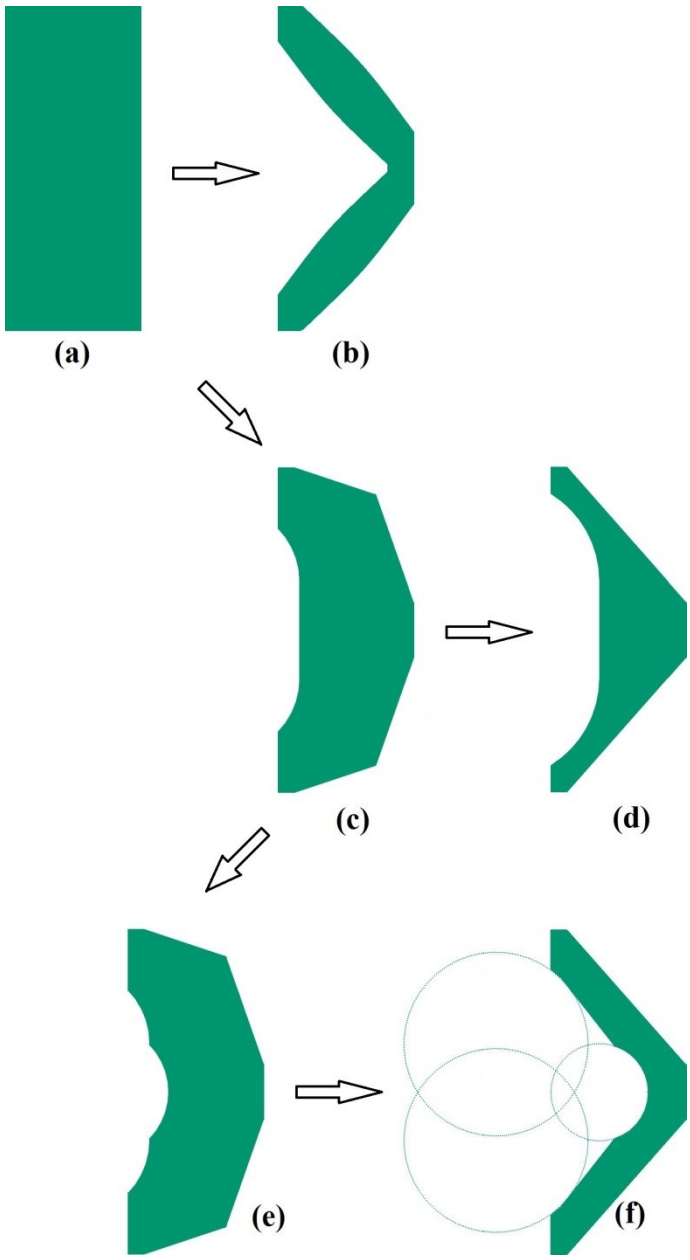

Fig. 4.11 Optimization processes of different schemes

(1) Regular level set approach (a-b);

(2) Machining feature-based approach with customized length scale L_{lim}=15 (a-c-e-f);

(3) Machining feature-based approach with customized length scale L_{lim}=25 (a-c-d)

As mentioned earlier, the 2D features can be regarded as the contour projection of the 2.5D machining features. Therefore, we extrude the 2D design with the depth of 10, and compare it

with the conventional 3D level set result. From Fig. 4.12 and Table 4.1, it can be seen that the 2.5D result employs the compliance nearly at the same level with the conventional 3D result, but has much better manufacturability.

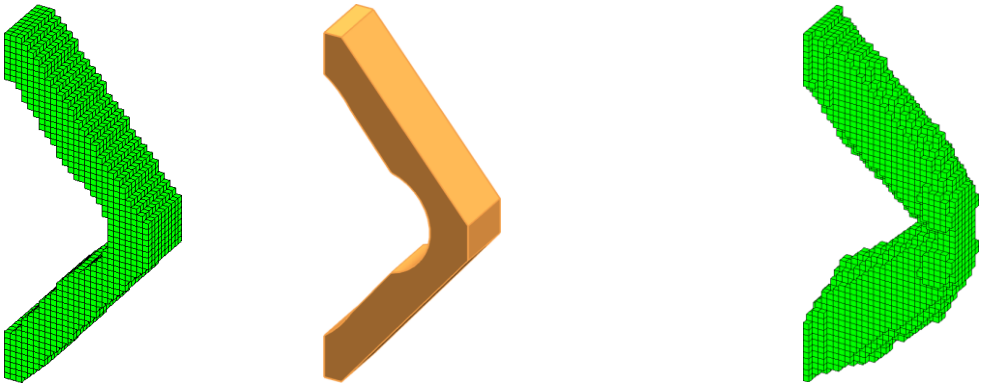

(a) Gird and iso-contour model of extruded 2.5D result

(b) Grid model of conventional 3D level set result

Fig. 4.12 Comparison between extruded 2.5D result and the conventional 3D level set result

Table 4.1 Quantitative comparison between extruded 2.5D result and the conventional 3D level set result

	Extruded 2.5D result	Conventional 3D level set result	Rate of increase compared with the conventional 3D result
Compliance (under the volume ratio of 0.3)	8.02	7.88	1.78%

4.5.2 Cube problem

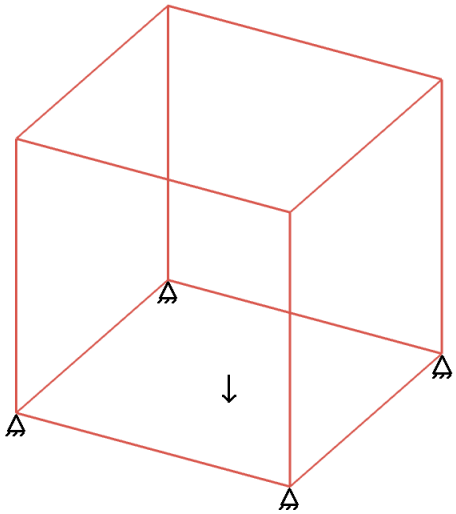

Fig. 4.13 Cube problem

In this case, the design domain (as shown in Fig. 4.13) is a cube (24*24*24) with its four bottom corners fixed and a force of magnitude 2 loaded at the bottom center. The objective is to minimize the compliance under the volume constraint of 0.2. Poisson ratio and Young's modulus are 0.3 and 1 respectively.

Three different optimization schemes have been adopted to demonstrate the effectiveness of the machining feature-based approach, as well as the scale control ability. The first scheme is the machining feature-based approach with customized length scale $L_{lim} = 20 * 20$, and the results are shown in Fig. 4.14. Comparatively, the second scheme is still the machining feature-based approach, but with the customized length scale $L_{lim} = 14 * 14$, for which the results are illustrated in Fig. 4.15. Finally, the conventional 3D level set approach is applied to derive the freeform 3D result as shown in Fig. 4.16.

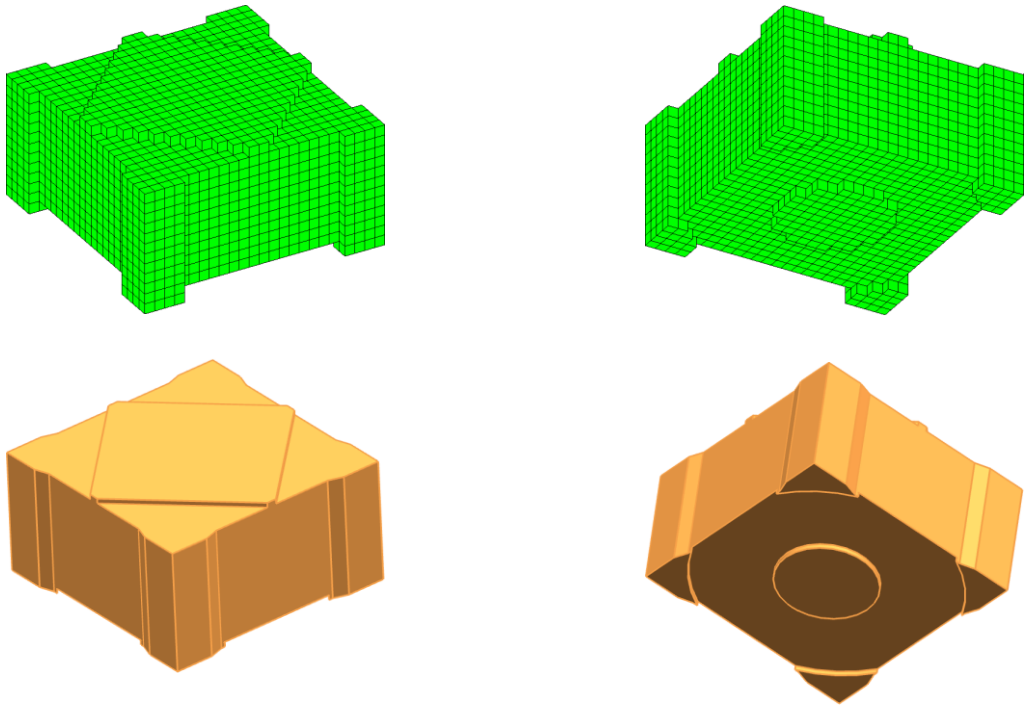

(a) Result after feature fitting

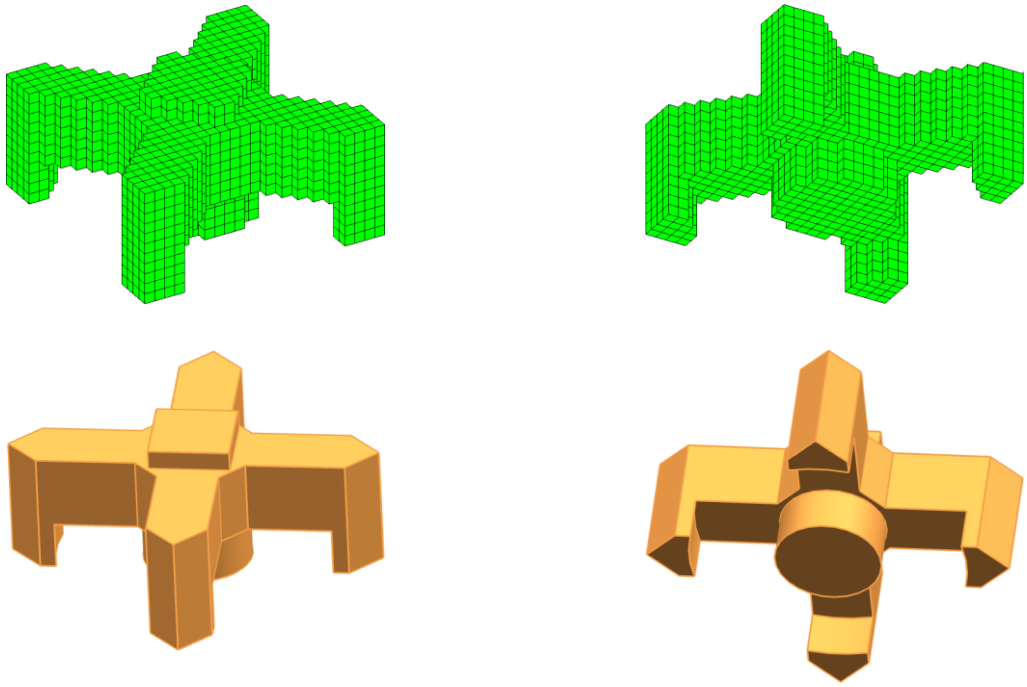

(b) Final result

Fig. 4.14 Results of the machining feature-based approach with $L_{lim} = 20 * 20$

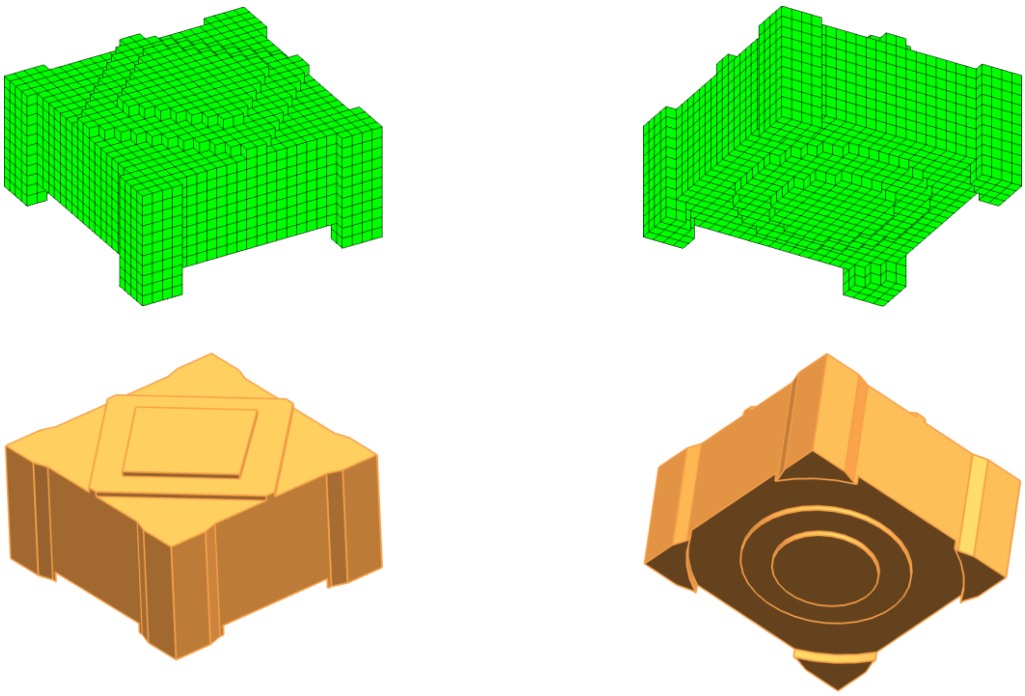

(a) Result after feature fitting

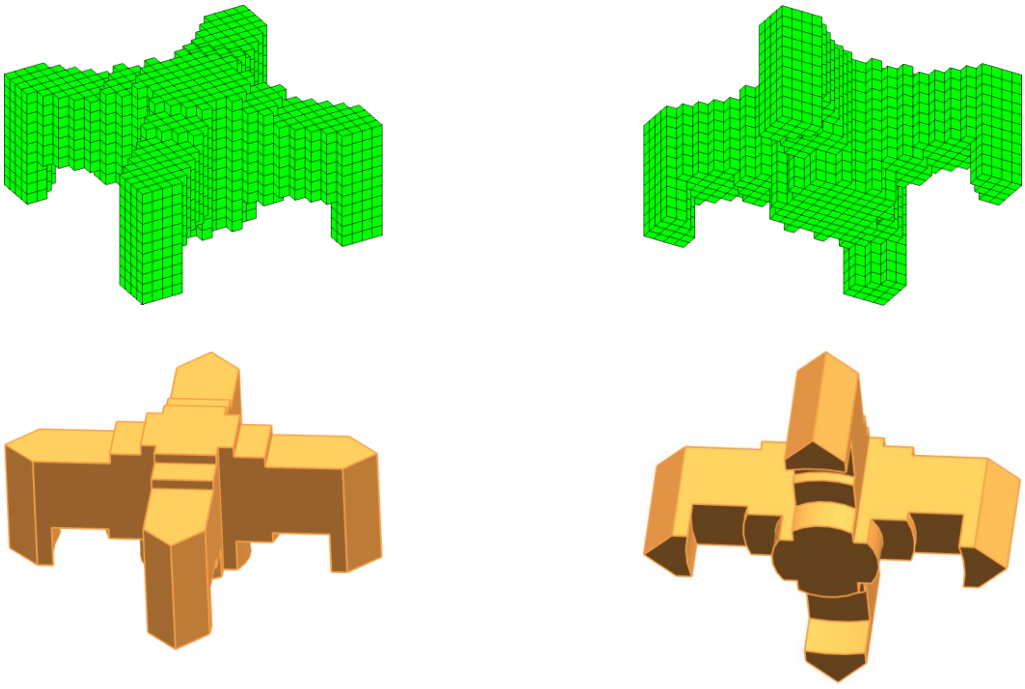

(b) Final result

Fig. 4.15 Results of the machining feature-based approach with $L_{lim} = 14 * 14$

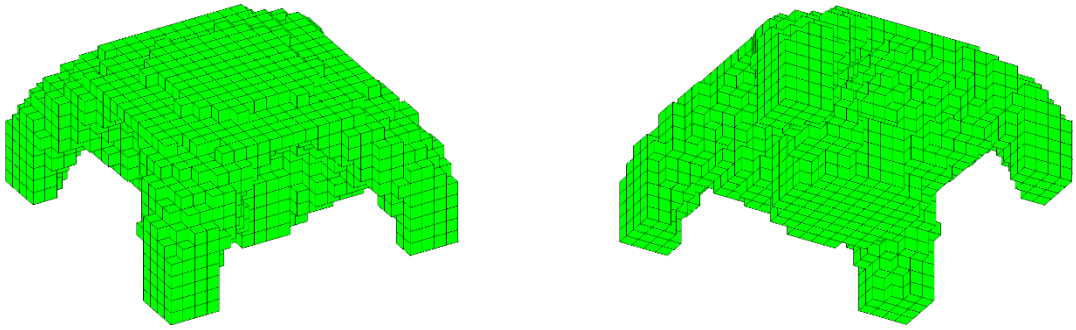

Fig. 4.16 Result of conventional 3D level set approach

Data of the three different results is listed in Table 4.2. Through data analysis, it can be concluded that the conventional 3D level set approach can derive the optimum, while the machining feature-based approach slightly sacrifices the optimality in order to improve the desired manufacturability. On the other hand, smaller customized length scale can lead the objective closer to the optimum. In fact, the 3D level set approach is equivalent to the machining feature-based approach with infinitesimal customized length scale. Practically this may take more time to machine as smaller tools and multiple tool changes may be required.

Table 4.2 Data of the three different results

	Machining feature-based result ($L_{lim} = 20 * 20$)	Conventional 3D result	Rate of increase compared with the conventional 3D result
Compliance (under the volume ratio of 0.2)	14.58	13.62	7.04%
	Machining feature-based result ($L_{lim} = 14 * 14$)	Conventional 3D result	Rate of increase compared with the conventional 3D result
Compliance (under the volume ratio of 0.2)	14.07	13.62	3.30%

4.5.3 Cantilever problem with fixed hole

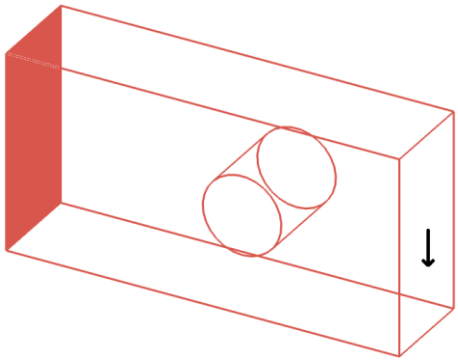

Fig. 4.17 Cantilever problem with fixed hole

The 3D cantilever (40*10*20) problem is depicted in Fig. 4.17, where the left side is fixed and a vertical force (magnitude = 2) pointing downward is loaded at the middle of the right face. The objective is to minimize the compliance with the maximum volume ratio of 0.4. Poisson ratio and Young's modulus of the material are 0.3 and 1, respectively. It is noted that a fixed hole exists in the design domain for purpose of assembly. This is a benchmark case cited from [Zhou and Wang 2013] to better demonstrate the effectiveness of our novel machining feature-based approach.

Fig. 4.18 presents two intermediate results (a-b), as well as the final design (c) of the 2.5D form feature-based approach. Specifically, the symmetric design in this case employs final compliance of 34.65.

For the 2.5D freeform feature-based approach, the intermediate results are shown in Fig. 4.19(a-b), and consequently, the final result is demonstrated in Fig. 4.19c, of which the compliance is 33.52.

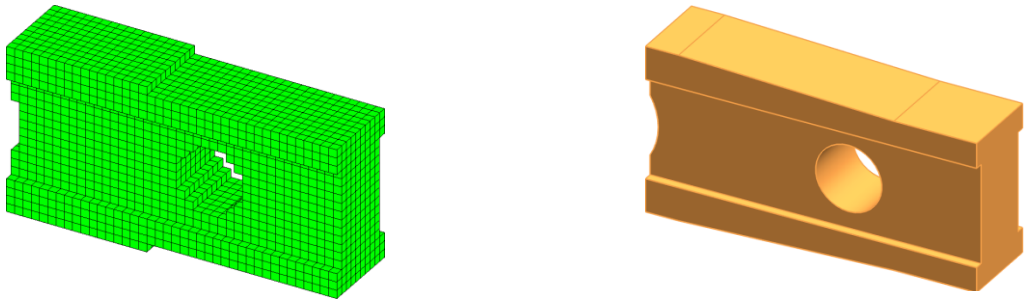

(a) Intermediate result

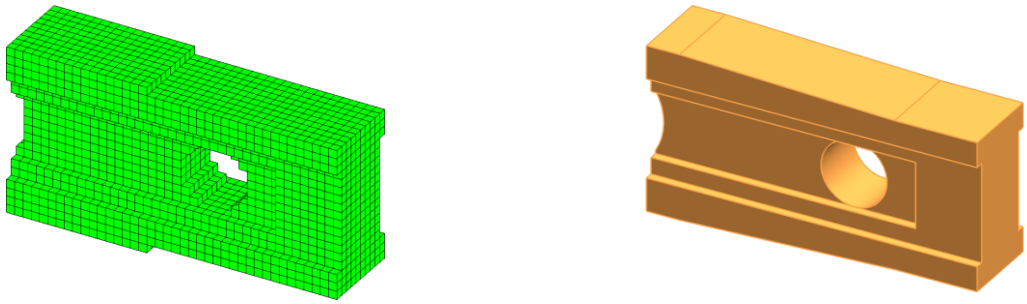

(b) Intermediate result

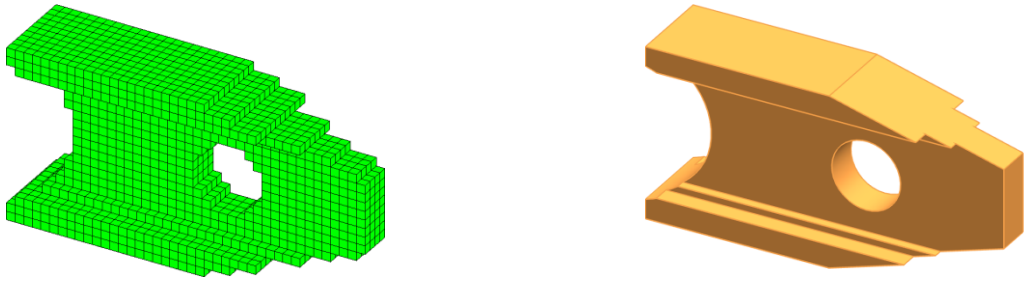

(c) The final result

Fig. 4.18 Optimization process of 2.5D form feature-based approach with L_{lim}=10*20

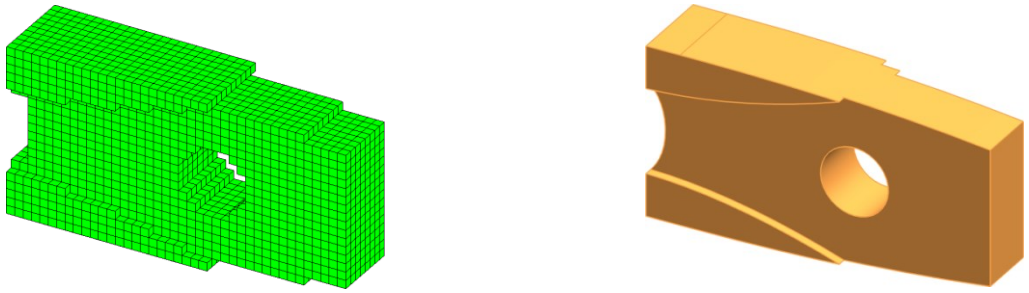

(a) Intermediate result

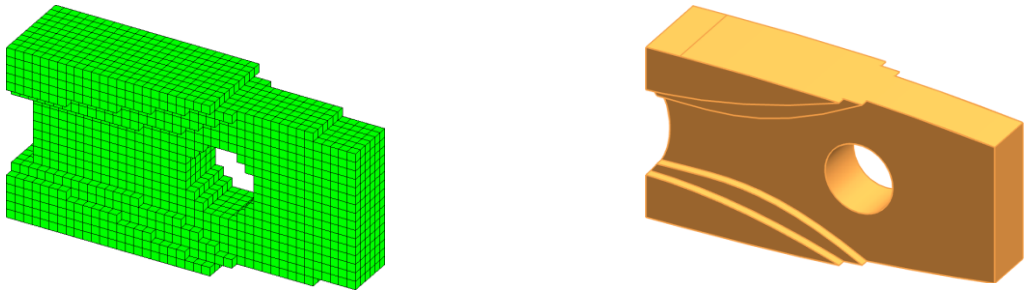

(b) Intermediate result

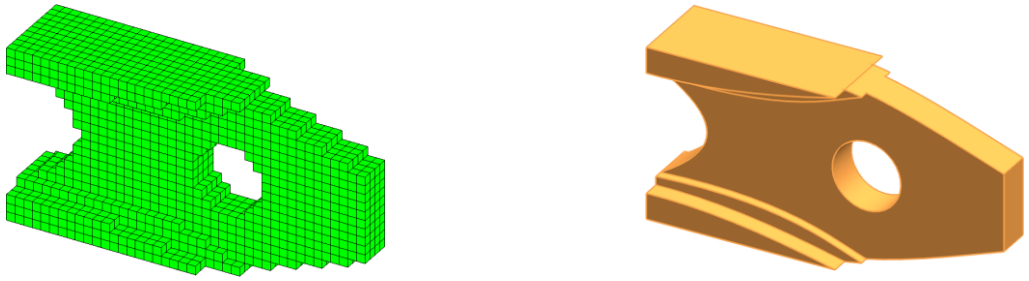

(c) The final result

Fig. 4.19 Optimization process of 2.5D freeform feature-based approach with L_{lim}=10*20

The conventional 3D level set result is shown in Fig. 4.20. Through comparison, it can be concluded that the material distributions are very similar among Fig. 4.18c, Fig. 4.19c and Fig. 4.20. Therefore, the mechanical performances can be predicted and are close as shown in Table 4.3. Readers who have interest can refer to [Zhou and Wang 2013] for a similar 3D result.

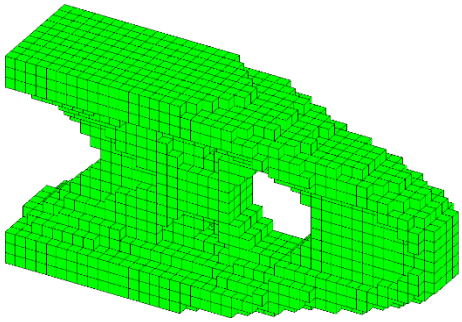

Fig. 4.20 Conventional 3D level-set result

Table 4.3 Statistic comparison between the machining feature-based and the conventional 3D results

	2.5D form feature-based result	Conventional 3D result	Rate of increase compared with the conventional 3D result
Compliance (under the same volume ratio of 0.4)	34.65	33.30	4.05%
	2.5D Freeform feature-based result	Conventional 3D result	Rate of increase compared with the conventional 3D result
Compliance (under the same volume ratio of 0.4)	33.52	33.30	0.66%

4.6 Conclusion

This chapter presents a novel explicit feature (2.5D machining feature) based level set topology optimization method, which relies on the feature fitting algorithm and the explicit feature-based shape optimization to directly obtain the explicit feature-based design. It overcomes the limitations of the existing explicit feature-based methods, and the effectiveness has been proven by a few numerical case studies.

For future work, there are mainly two directions to further improve the method.

First, the current geometry is CSG geometry based, while the B-rep geometry dominates the CAD systems. This fact leads to a gap between the topological solution and the editable CAD models, which is normally fixed through manual model reconstruction which is tedious and labor-costly. Therefore, the author intends to fix this problem by developing the B-rep geometry based topology optimization method which will be introduced in Chapter 5.

Second, currently, only geometry feature is involved in the optimization problem, but not the attached semantic information. This means the full power of engineering features cannot be fully utilized, and this problem will be further discussed in the Chapter 6.

Chapter 5 CAD/CAE integration through B-rep geometry based topology optimization

As suggested at the end of the last chapter, B-rep geometry based approach is superior than the current CSG geometry based approaches in implementing the explicit feature-based topology optimization. Moreover, the development of B-rep geometry based approach would fix another long-lasting problem: CAD/CAE integration, because of the unified geometry format and the synchronously updated design and analysis models.

Therefore, the objective of the work in this chapter is to investigate the CAD/CAE integration through the modified fixed grid finite element method (FGFEM) and the B-rep geometry based topology optimization. We intended to realize the automation of the inverse process. More specifications will be presented in the following contents, and the innovation points can be summarized as below:

- A modified FGFEM is developed which achieves a new balance between the computationally efficient FGFEM and the numerically accurate X-FEM (extended finite element method);
- A B-rep geometry based topology optimization method is developed which performs topological changes totally in the manner of conventional CAD modeling operations. This new method eliminates the need of mutual translation between the CAD model and the analysis/optimization model. Additionally, the feature modeling history can be properly constructed.

5.1. B-rep geometry based CAD modeling

To better understand the CAD/CAE integration, it is necessary to specify the solid geometry representations in both CAD and CAE systems.

B-rep constructs the solid geometry explicitly through clearly specifying the geometry entities including vertices, edges, and faces, as well as the related topology relationships. Compared to

CSG geometry modeling, it allows more modeling flexibility and is more intuitive to designers. Comparatively, CSG geometry modeling employs implicit representation for geometry primitives and relies on Boolean operations to construct complex geometry. It enjoys the computational advantages of the implicit representation that, the points inside and outside the solid geometry can be easily distinguished and the geometry is insensitive to topological changes [Chen et al. 2007, 2008a]. Therefore, it is widely accepted of the B-rep format in CAD systems and the CSG format by shape and topology optimization methods [Liu and Ma 2015]. On the other hand, CAE systems employ voxel based geometry representation, because of the discrete nature of the finite element analysis.

According to the illustrations above, it is necessary to unify the geometry representations. In this work, FGFEM is applied so that mesh conformity is not required and the B-rep geometry can be directly passed from CAD to CAE. Additionally, B-rep geometry based topology optimization is developed so that the CSG-dependence of the optimization activities can be eliminated. More details will be introduced in following sections.

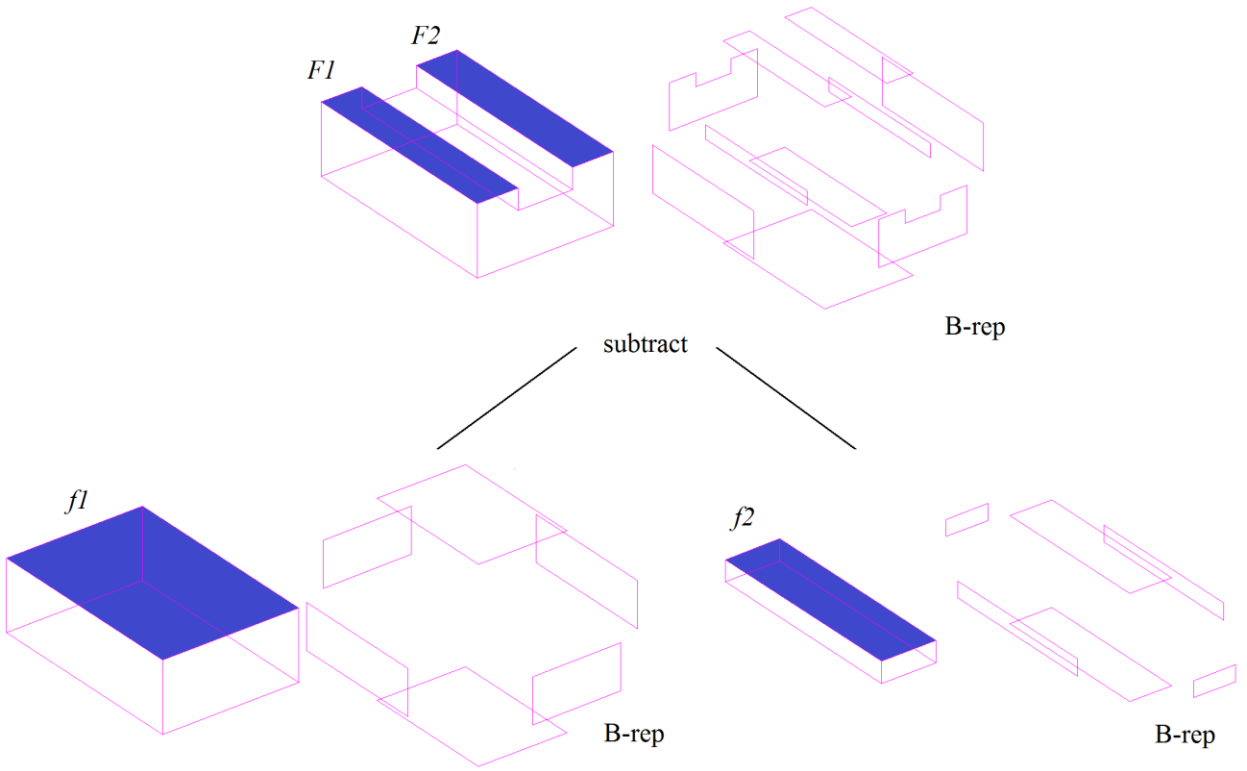

Fig. 5.1 B-rep modeling

To optimize the B-rep model, boundary velocity field based optimization is suitable and widely adopted [Zhou and Wang 2013]. As shown in Fig. 5.1, there are two levels of the B-rep model, of which the top-level model is constructed through subtracting operation of the two low-level block features. Then, there is the problem about which level of the B-rep model should be optimized. It is natural to apply the top-level model as the optimization target, because the boundary segments belong to the real artifact and therefore are intuitive. Additionally, there are more design freedoms. However, it may violate the corresponding relationship and therefore invalidate the modeling history. For instance, as shown in Fig. 5.1, if the top-level faces *F1* and *F2* are optimized of the positions independently, the coplanar relationship will be violated as they correspond to the same low-level face *f1*. To overcome this limitation, it is more appropriate to optimize the low-level feature models. Through manipulating the low-level boundary segments, nearly equivalent optimization effect could be achieved, and the modeling history is guaranteed to be valid. It is noted that, effective area of the low-level boundary segment should be timely tracked in order to accurately calculate the sensitivity result. The "effective area" means the overlapping area between the low-level boundary segment and the top-level model boundary. As shown in Fig. 5.1, the top-level faces *F1* and *F2* is the effective area of the low-level boundary segment *f1*.

For special cases, non-manifold B-rep geometry modeling techniques may be applied [Hamri et al. 2010; Nolan et al. 2015]. This will be considered in our future work.

5.2. Fixed grid finite element analysis (FGFEA)

For CAD/FEA integration, meshing is a mandatory step to transform the CAD solid geometry into finite elements. Normally, the mesh conforms to the geometry, but iterative re-meshing efforts are required for cyclic design process, which is time-consuming and may require the repeated user interaction. Therefore, in this work, fixed grid finite element analysis (FGFEA) is employed and the objective is to develop a modified FGFEA for more efficient numerical implementation.

5.2.1 FGFEA

FGFEA has been investigated for decades. It is free from mesh deformation or re-meshing to adapt the evolving geometry, and therefore, it is computationally efficient. However, several challenging issues remain.

Because of the non-conforming characteristic, the finite elements are categorised into three types: internal element (IE), external element (EE), and boundary crossed element (BCE). The IE is filled with solid material, and the EE is assumed of the "ersatz" material with properties close-to-zero to avoid the singularity problem. The BCE is special, because it includes both solid and void areas. Different approaches have been developed to approximate its properties. The simple approach is to assume the elements are either solid or void according to the area-fraction weight [Garcia-Ruiz and Steven 1998; Xia et al. 2010b]; however, this approach lacks of accuracy especially for stress-concentrated areas. The second approach is to homogenize the properties proportional to the area-fraction weight. This approach is widely applied to support CAD/FEA integration [Garcia-Ruiz and Steven 1998], shape optimization [Kim and Chang 2005], and the topology optimization methods such as SIMP [Bendsoe and Sigmund 2003], ESO [Kim et al. 2000; Kim et al. 2003], and level set [Wang et al. 2003].

Regularly, the element stiffness matrix is proportionally approximated, as:

$$\boldsymbol{D} = u\boldsymbol{D}_m$$

$$u = \begin{cases} 1 & for\ IEs \\ \alpha & for\ EEs \\ V_m/V_e & For\ BCEs \end{cases} \tag{5.1}$$

in which $\boldsymbol{D}$ and $\boldsymbol{D}_m$ represent the approximated stiffness matrix and the solid element stiffness matrix, respectively. V_m and V_e represent the internal area of BCE and the total area, respectively. α is a small positive number.

In SIMP method, the area-fraction weight is penalized by $p \geq 3$, as:

$$\boldsymbol{D} = u^p\boldsymbol{D}_m \tag{5.2}$$

which intends to eliminates the grey elements in the final design.

In level set method, the Heaviside function is applied, as:

$$\boldsymbol{D} = H(\Phi)\boldsymbol{D}_m$$

$$H(\Phi) = \begin{cases} \alpha & \Phi < -h \\ \dfrac{3(1-\alpha)}{4}\left(\dfrac{\Phi}{h} - \dfrac{\Phi^3}{3h^3}\right) + \dfrac{1+\alpha}{2} & -h \le \Phi < h \\ 1 & \Phi \ge h \end{cases} \tag{5.3}$$

in which Φ is the element level set value, and h is the band width of numerical approximation.

In fact, it is accurate to proportionally homogenize the stiffness matrix only if the elements are linearly interpolated. Given the commonly applied bilinear interpolation, it would be more appropriate to numerically calculate the stiffness matrix by integrating over the solid parts of BCEs. X-FEM (Extended finite element method) [Moes et al. 1999] realizes the solid part integration through local enrichment, and it is effective in modeling any moving discontinuities without mesh deformation or re-meshing. Later, the involvement of implicit interface representation powers the interface tracing and facilitates the local enrichment [Sukumar et al. 2001; Belytschko et al. 2003]. This combination has been successfully applied to solve shape [Van Miegroet and Duysinx 2007] and topology [Wei et al. 2010] optimization problems.

On the other hand, by using the Eulerian mesh, the inconformity also brings difficulties in attaching the boundary conditions [Kumar et al. 2008]. This issue does not occur in this work because the Dirichlet boundaries are fixed and only design-independent surface loads are employed.

5.2.2 Local fine graining

It has been validated in previous works that, by reducing the grid size, small geometry details can be modeled by area-fraction weighted properties without a significant loss of accuracy [Garcia-Ruiz and Steven 1998]. However, the selected size cannot be too small given the high computation expense [Belytschko et al. 2003]. X-FEM realizes the fine graining through local enrichment of the BCEs. The local enrichment relies on further partitioning of the BCEs, which is similar to local re-meshing. As shown in Fig. 5.2, the cases of solid part partition of the BCEs are listed. It is simple for 2D cases, however, there would be much more possibilities for 3D

cases and it is even more complex if multi-boundary crossing happens. Therefore, the authors would propose a new fine graining method which better aligns the fixed grid nature.

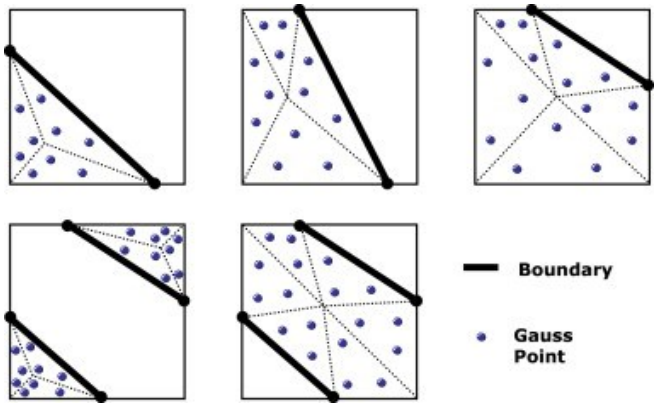

Fig. 5.2 Solid part partition of the BCEs [Wei et al. 2010]

As shown in Fig. 5.3a, the BCE is treated in a new way that it is further partitioned into four sub-grids. This partition is independent of the boundary crossing pattern and therefore the process is simplified. Then, the element stiffness matrix is calculated through Eq. (5.4).

$$\boldsymbol{D} = \sum_{i=1}^{4} \int_{\Omega_i} \max(w_i, \alpha) \boldsymbol{B^T D_m B} d\Omega \tag{5.4}$$

In Eq. (5.4), w_i is the area-fraction weight of sub-grid i, and $\boldsymbol{D_m}$ is the solid material elasticity matrix. It is noted that the sub-grids are only applied to evaluate the integrations while the finite element scale is not increased.

In Fig. 5.3(b-e), distributions of the diagonal terms of the integrand are presented according to the different BCE treatments. It can be observed that the new fine graining method demonstrates the capability of modeling material discontinuity which is compatible to X-FEM.

For the advantages, the fixed partition and the sub-grid area fraction calculation are computationally economic and not sensitive to dimension increase, especially compared to the partition and unity process of X-FEM.

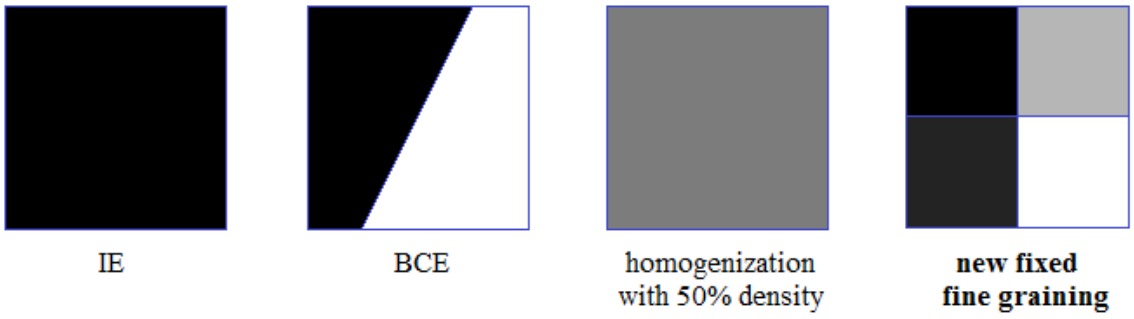

(a) BCE treatments

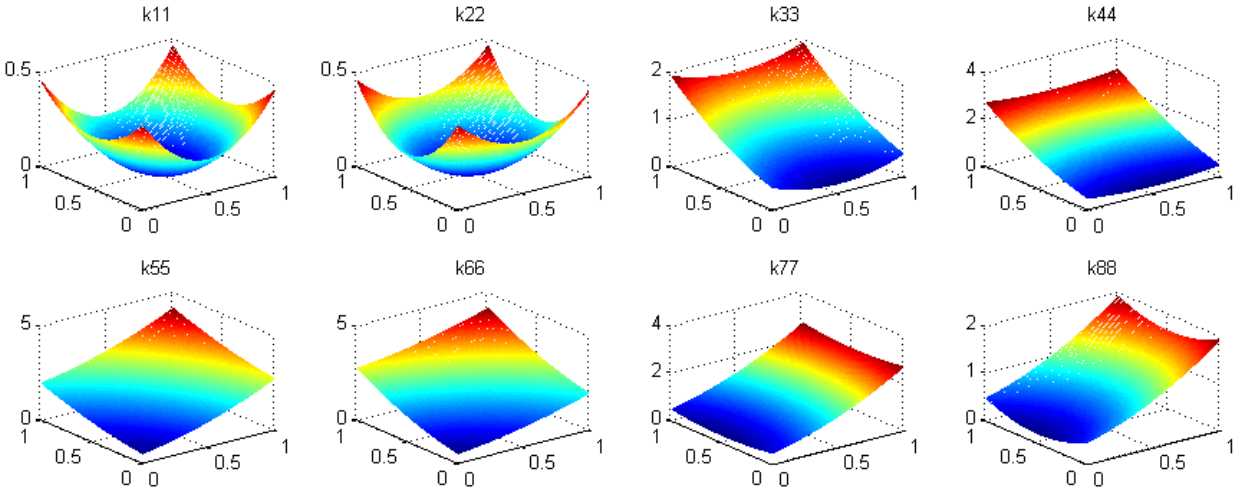

(b) IE

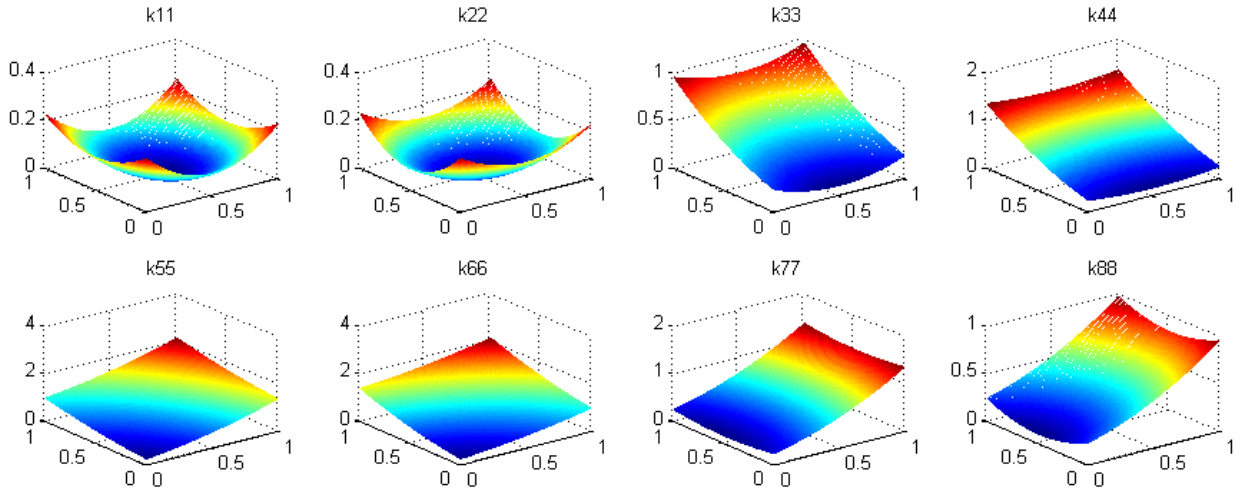

(c) Homogenization with 50% density of the BCE

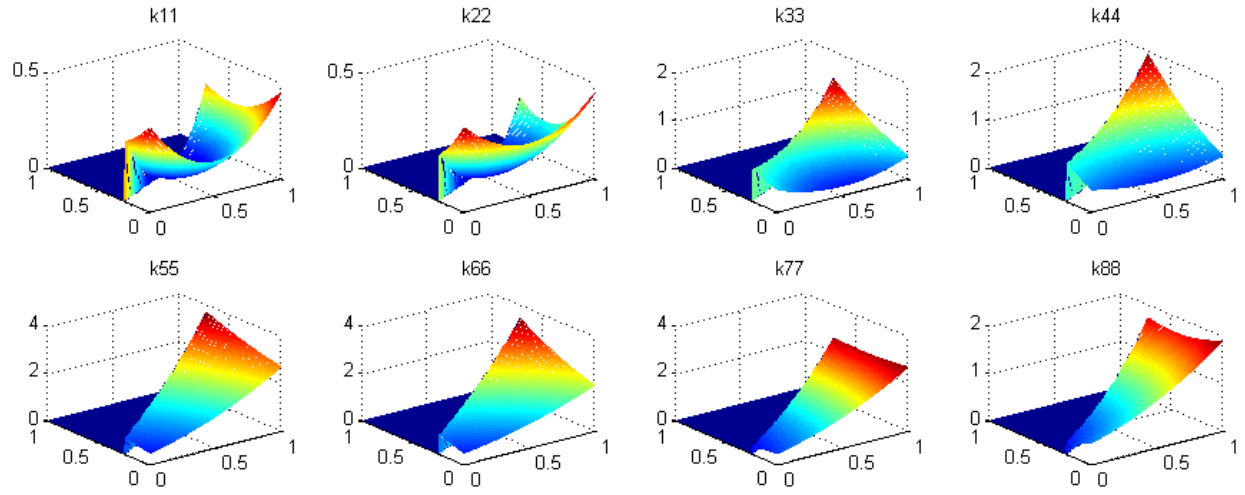

(d) X-FEM of the BCE

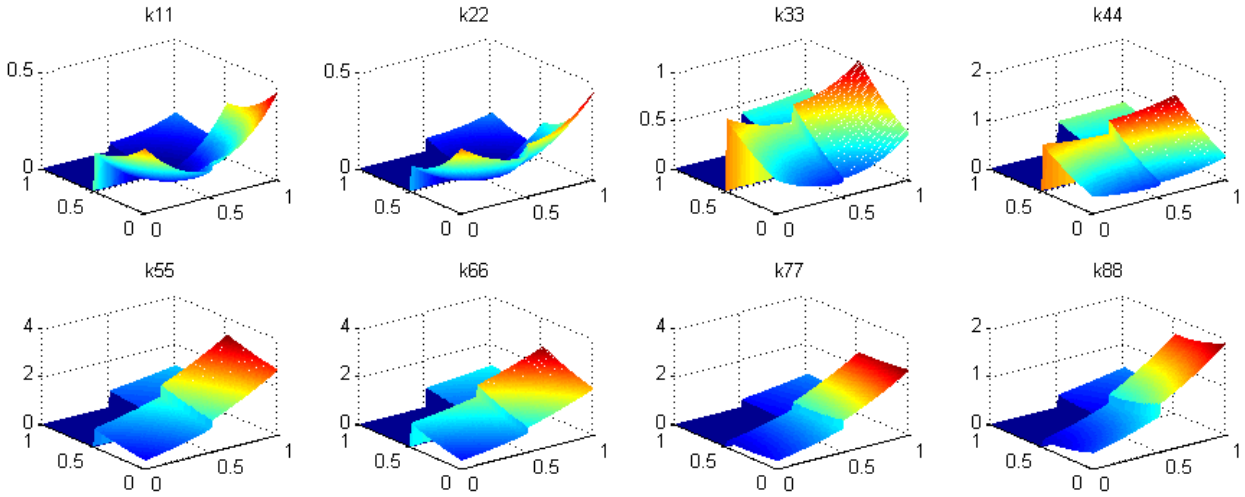

(e) Fixed fine graining of the BCE

Fig. 5.3 Distributions of the diagonal terms of the integrand according to the different BCE treatments

5.3. Automated inverse integration

The automated inverse integration is realized through the B-rep geometry based topology optimization. It is composed of two sub-steps: feature modeling and sizing optimization. For feature modeling, it selects the eligible faces and makes them the reference surfaces of the drafting and extrusion operations. Certain rules are set up to determine the face eligibility and

also the exact drafting pattern, and the extrusion operation causes the topological changes. For sizing optimization, it optimizes the sizing configuration of the feature primitives which leads to the final optimal solution. The overall work flow is demonstrated in Fig. 5.4, from which it is observed that two rounds of feature modeling and sizing optimization are performed. The reason as well as the technical details will be introduced in the rest of this section.

This work will only investigate the stiffness-maximization problem which is formulated as:

$$min. \quad J = \frac{1}{2}\int_D \boldsymbol{D}\boldsymbol{e}(\boldsymbol{u})\boldsymbol{e}(\boldsymbol{u})d\Omega$$
$$V \leq V_{max} \tag{5.5}$$

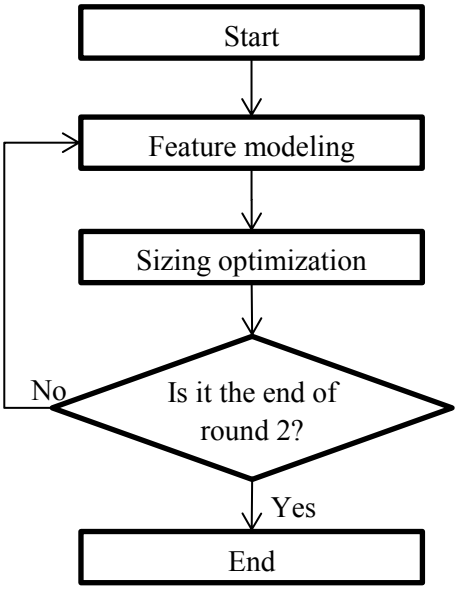

Fig. 5.4 Overall work flow of the automated inverse process

5.3.1 Feature modeling

In CAD system, feature modeling is performed by selecting the reference surface, drafting, and then doing the extrusion. Regularly, these operations are manually conducted, but in this work, we attempt to realize the automation. The overall work flow is illustrated in Fig. 5.5.

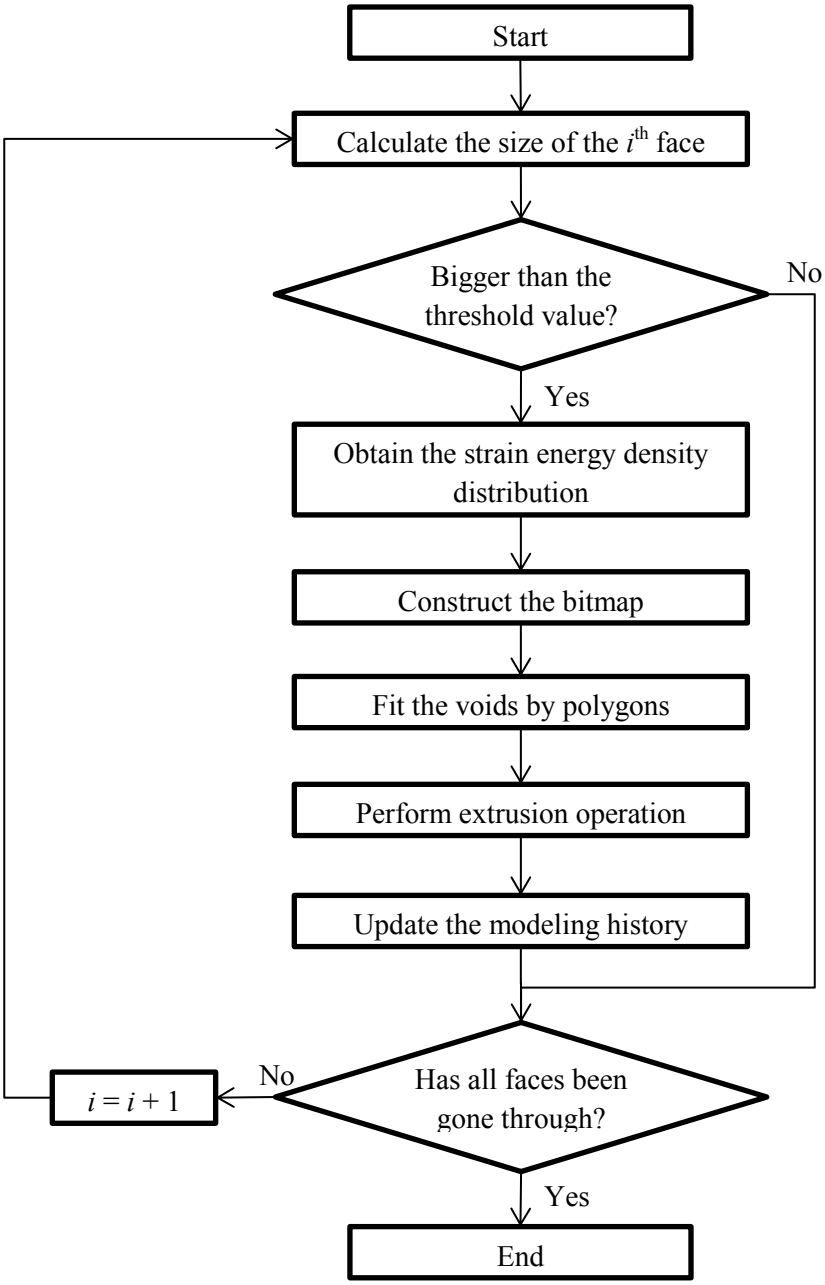

Fig. 5.5 Work flow of the automated feature modeling process

The work flow starts by checking the face sizes. Generally, the feature modeling operations are performed on faces in large size, so that small-scale feature primitives can be avoided. As mentioned in [Mei et al. 2008; Liu and Ma 2015], the small-scale feature primitives unnecessarily complicate the topology structure and may cause manipulation and manufacturing difficulties. Therefore, a threshold value is pre-defined and the feature modeling operations will only happen to faces larger than that. A thin-plate structure design example is shown in Fig. 5.6a.

The threshold value is pre-defined as 1/3 of the front face size, with which the side faces are disabled of the feature modeling operations.

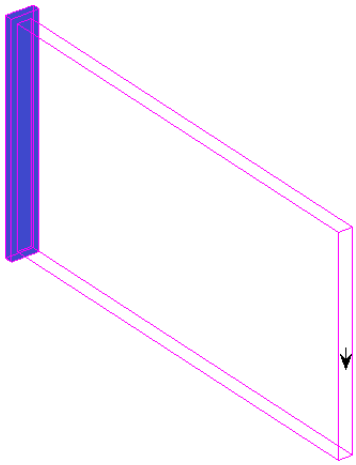

(a) Thin-plate structure (60*30*2)

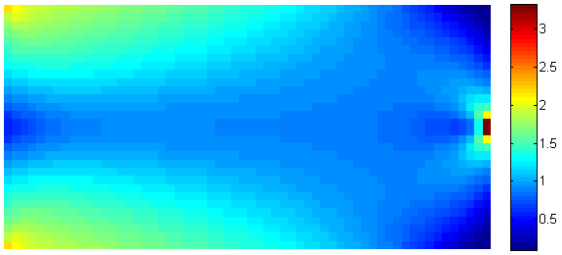

(b) SED distribution

(c) Bit map

(d) Fitted drafting pattern

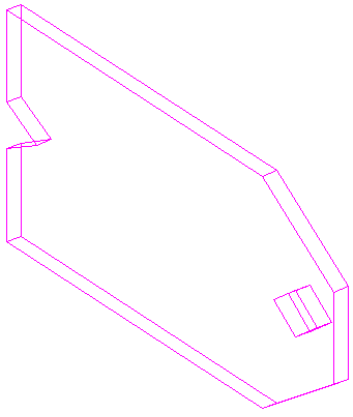

(e) Thin-plate structure after extrusion

Fig. 5.6 Feature modeling process

Then, for eligible faces, the strain energy density (SED) distribution is obtained through FEA. Normally, the SEDs follow disorganized distribution, as shown in Fig. 5.6b, and cannot be directly used to obtain the drafting pattern. Therefore, an image processing procedure is applied to translate the SED distribution into a bitmap. Another threshold value is defined as $\beta * median(SEDs)$, in which $median(SEDs)$ is the function calculating the median of the SEDs, and β is a factor smaller than 1. With this setup, the elements employing SED bigger than the threshold value will be defined to be solid, while the other elements defined to be void, as shown in Fig. 5.6c.

For the bitmap, it is not readable in CAD system, and it should be interpreted about the solid/void interface through curve fitting. In this work, only polygons are applied for the sake of simplicity. The fitted draft pattern is demonstrated in Fig. 5.6d. Finally, through extrusion, the thin-plate structure is updated into Fig. 5.6e.

Once the work flow shown in Fig. 5.5 is completed, even more faces are generated, some of which may be eligible for further feature modeling. However, it is not suggested to immediately conduct the second round of feature modeling, because it very likely will generate a topologically-equivalent drafting pattern. There will be only sizing differences while no new feature primitive, which makes the second round feature modeling meaningless. It is suggested to interlace the feature modeling and sizing optimization steps. Following Fig. 5.4, sizing optimization is conducted after the first round of feature modeling, which evolves the boundary segments and redistributes the SEDs drastically. Therefore, the second round of feature modeling will very likely generate new feature primitives and modified topology structure.

In order to stabilize the overall convergence, it is suggested to apply a relaxed volume constraint to the first round sizing optimization, as:

$$V \leq \gamma V_{max}$$
$$V_{max} < \gamma V_{max} < 1 \tag{5.6}$$

5.3.2 Sizing optimization

The feature modeling operations create new feature primitives; however, this preliminary design lacks of optimality. Optimization of the sizing configuration of these feature primitives is still required.

5.3.2.1 B-rep geometry based sensitivity analysis

Previously in [Chen et al. 2007, 2008a; Zhou and Wang 2013], CSG geometry based sensitivity analysis was performed, which is not applicable in this work because of the explicit boundary representation. Therefore, B-rep geometry based sensitivity analysis is developed, and details are presented below.

Based on the shape sensitivity analysis theory [Choi and Kim 2005a, 2005b], a continuous but irregular velocity field is generated alone each linear boundary segment, which causes the freeform evolvement. However, it is unwanted because shape characteristic of the linear boundary segments would change, which causes inconsistency of the boundary representation. Therefore, it is necessary to regulate the velocity field and thus maintain the shape characteristic. Referring to the least squares fitting method applied in [Zhou and Wang 2013], 2D velocity field can be trained by solving the following optimization problem:

$$min.\ \ Z = \frac{1}{2}\int_{\Gamma_i} [v_t(v_m, \theta) - v_c]^2 dS \tag{5.7}$$

in which Γ_i is the ith boundary segment; v_c is the calculated velocity field; v_t is the trained velocity field. For any linear boundary segment, it has two design freedoms of movement (v_m) and rotation (θ). Therefore, v_m and θ are the optimization variables, and v_t is the function of v_m and θ as presented in Eq. (5.7). It is noted that, the velocity is defined positive if it is in the normal direction pointing towards the material domain.

Because of the Eulerian mesh and the grey elements applied, the sensitivity calculation is problematic. As investigated in [Dunning et al. 2011], sensitivity calculation errors appear in the BCEs, and the errors increase as the area-fraction weights decrease. Therefore, they proposed the nodal averaging method (see Fig. 5.7) to improve the sensitivity calculation [Dunning et al.

2011], which has been proven effective. In fact, the nodal averaging method is widely applied to derive smooth sensitivity analysis result [Guest et al. 2004].

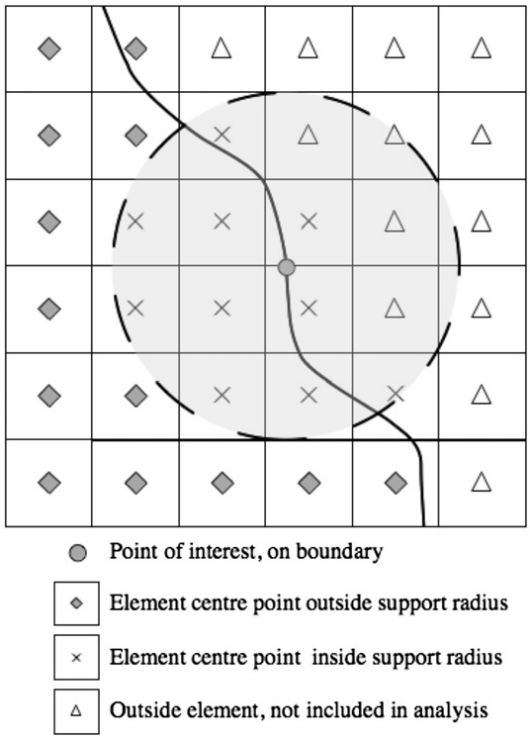

Fig. 5.7 Element center point sampling scheme [Dunning et al. 2011]

In this work, the normalized sensitivity result is calculated by:

$$v_n{}^e = \frac{\sum_{i\in S} v_c{}^i \omega(\boldsymbol{X}^i - \boldsymbol{X}^e)}{\sum_{i\in S} \omega(\boldsymbol{X}^i - \boldsymbol{X}^e)}$$

$$\omega\left(\boldsymbol{X}^i - \boldsymbol{X}^e\right) = \begin{cases} \dfrac{r - |\boldsymbol{X}^i - \boldsymbol{X}^e|}{r} & if\ \boldsymbol{X}^i \in S \\ 0 & otherwise \end{cases} \tag{5.8}$$

in which, S and r represent the circular area and its radius, respectively; $\boldsymbol{X}^e$ and $v_n{}^e$ mean the coordinates and the normalized sensitivity result of the point of interest; and $\boldsymbol{X}^i$ and $v_c{}^i$ represent the coordinates and the calculated sensitivity result of the ith element center inside the circular area. Consequently, the calculated velocity (v_c) in Eq. (5.7) is replaced by the normalized velocity (v_n).

As shown in Eq. (5.7), the continuous boundary integration is non-trivial to be analytically calculated. Therefore, we discretize Eq. (5.7) into:

$$min.Z = \frac{1}{2}\sum_{j=1}^{q} \varphi_j (v_t - v_n{}^{e_j})^2$$
$$\sum_{j=1}^{q} \varphi_j = 1 \tag{5.9}$$

where φ_j and e_j are the weighting factor and the integral point of discretized piece j, respectively; q represents the total number of discretized pieces.

Given the conventional topology optimization methods including SIMP [Bendsoe and Sigmund 2003], ESO [Xie and Steven 1993], and level set [Wang et al. 2003; Allaire et al. 2004], they share the same idea to remove materials from area of low SEDs while increase materials for area of high SEDs. This idea is inherited in this work to derive the element sensitivity result, which is [Allaire et al. 2004]:

$$v_c = \lambda - \boldsymbol{De}(\boldsymbol{u})\boldsymbol{e}(\boldsymbol{u}) \tag{5.10}$$

in which λ is still the Lagrange multiplier to satisfy the volume constraint.

5.3.2.2 Design update

According to the sensitivity result, the vertex locations are updated and so are the edges (see Fig. 5.8b). However, the shared vertexes are split into separate ones which changes the topology structure as shown in Fig. 5.8(a-b), which is unreasonable. Therefore, new shared vertex positions should be calculated to keep the topology structure consistent as shown in Fig. 5.8c. The implementation details will not be illustrated here for its simplicity.

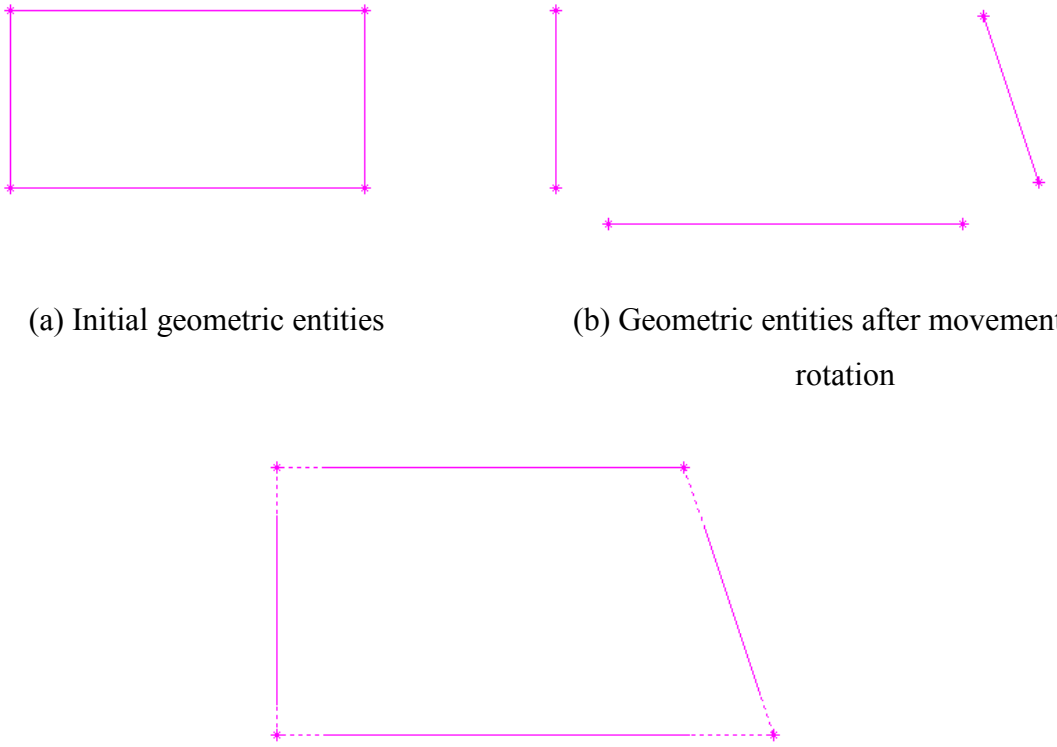

(a) Initial geometric entities

(b) Geometric entities after movement and rotation

(c) Re-build the geometric entities to keep the topology structure consistent

Fig. 5.8 Design update of the geometric entities

5.3.2.3 Implementation

With all the implementation details well illustrated, this sub-section will present a complete inverse process. The thin-plate example shown in Fig. 5.6 is studied.

(a) Structure after the first round feature modeling

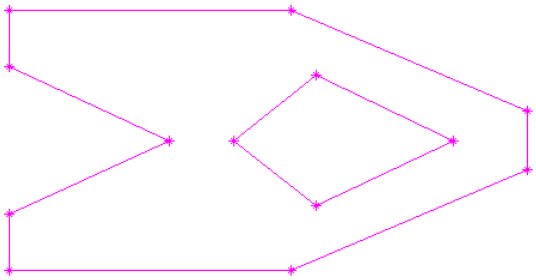

(b) Structure after the first round sizing optimization

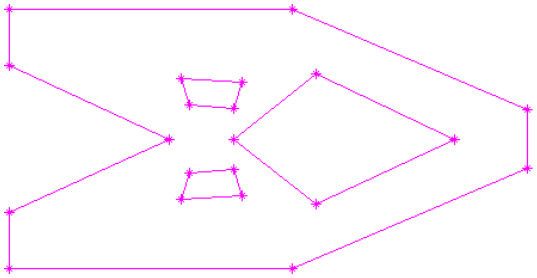

(c) Structure after the second round feature modeling

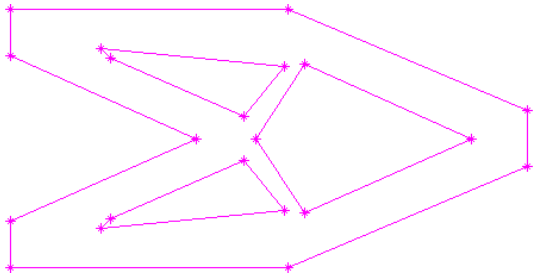

(d) Structure after the second round sizing optimization

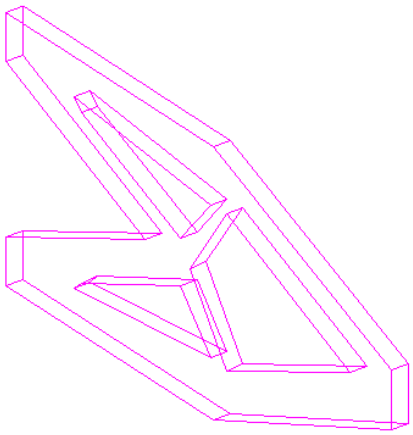

(e) 3D view of the optimal solution

Fig. 5.9 Automated inverse process

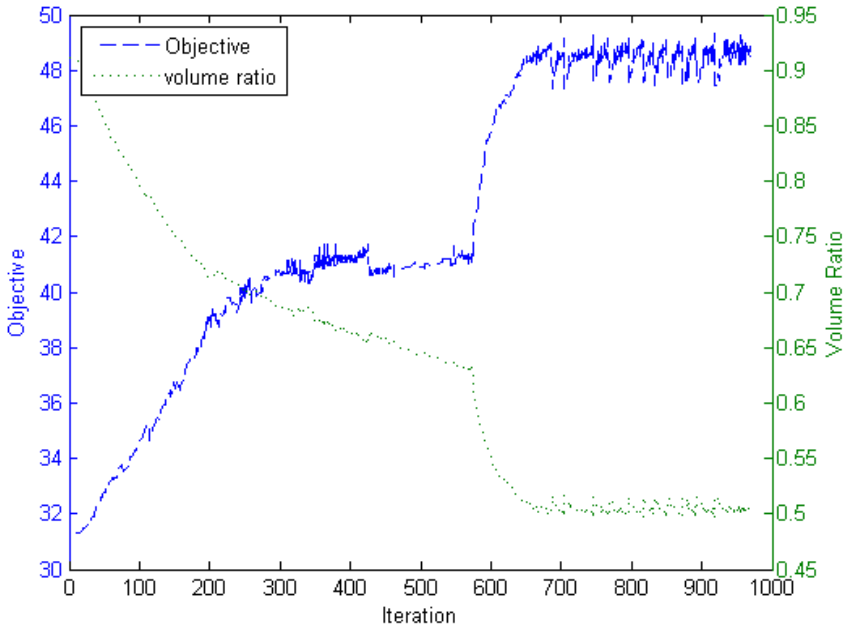

Fig. 5.10 Convergence history

In Fig. 5.9, the complete inverse process is demonstrated, and the convergence history is shown in Fig. 5.10. The thin plate goes through two rounds of feature modeling and sizing optimization. For the first round, the feature modeling process is already illustrated in Fig. 5.6. γ is assigned the value 1.3, so the first round sizing optimization converges around the material volume ratio of 0.65. For the second round, another drafting and extrusion dig two more holes, and the sizing optimization converges at the expected volume ratio of 0.5. The final result through the automated inverse process matches some benchmark results of the conventional topology optimization, which proves the effectiveness of this new method.

As mentioned earlier, the feature modeling history is established and timely updated. As demonstrated in Fig. 5.11, the initial modeling history only records creation of the thin plate as shown in Fig. 5.11a; then, Fig. 5.11b records the first round feature modeling and Fig. 5.11c records the second round feature modeling. It is noted that *f1*, *f2* represent the front and the back faces of the thin plate, respectively.

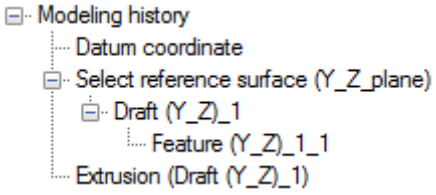

(a) Initial modeling history

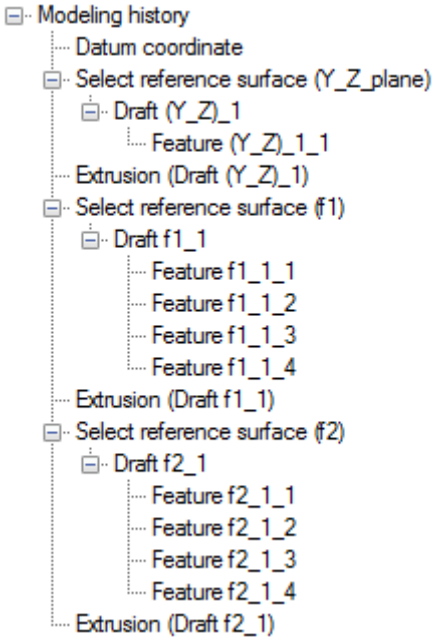

(b) Modeling history after the first round feature modeling

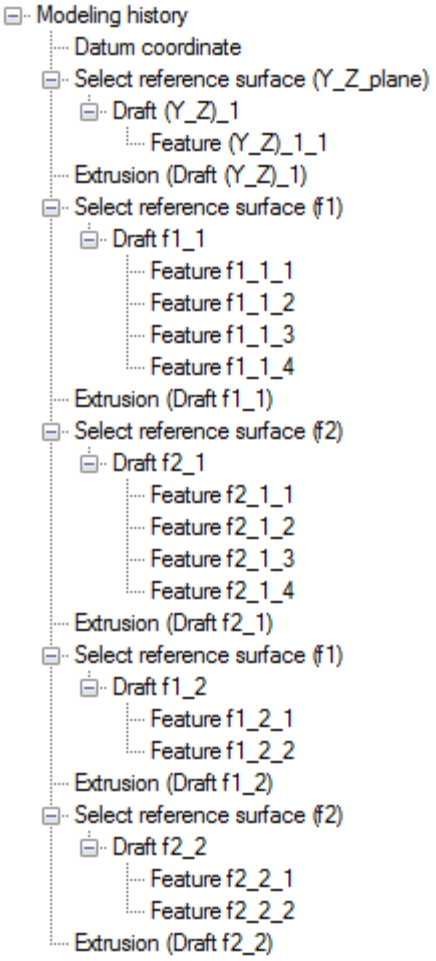

(c) Modeling history after the second round feature modeling

Fig. 5.11 Evolvement of the feature modeling history

5.4 Case study

5.4.1 The Michell structure

In this sub-section, the Michell structure is studied as a thin plate design problem. The initial design domain and the attached BCs are demonstrated in Fig. 5.12a. The objective is to derive the stiff design under the material volume constraint of 0.5.

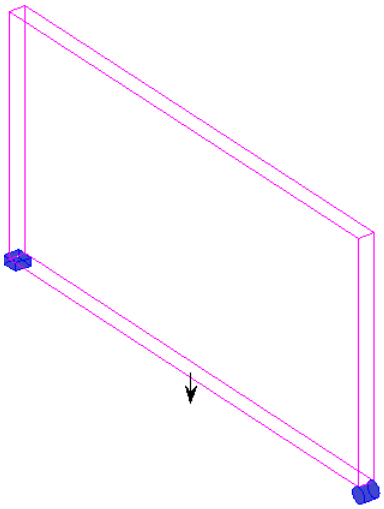

(a) Initial design domain (60*30*2) and BCs

(b) Structure after the first round feature modeling

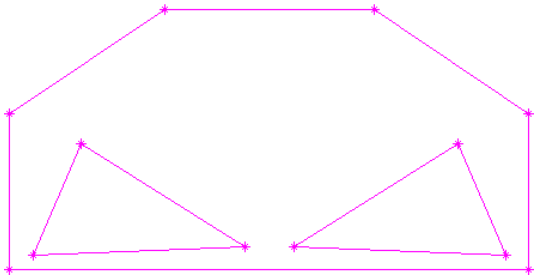

(c) Structure after the first round sizing optimization

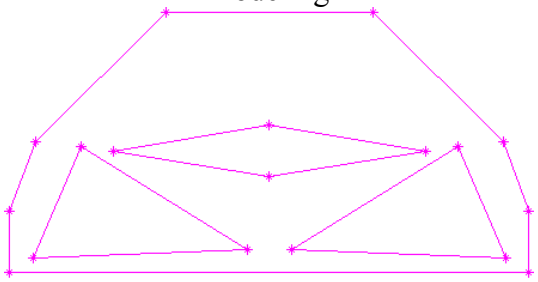

(d) Structure after the second round feature modeling

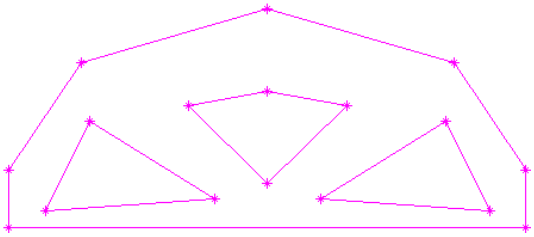

(e) Structure after the second round sizing optimization

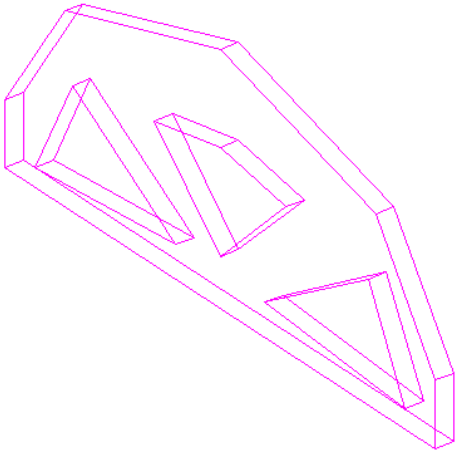

(f) 3D view of the optimal solution

Fig. 5.12 Automated inverse process

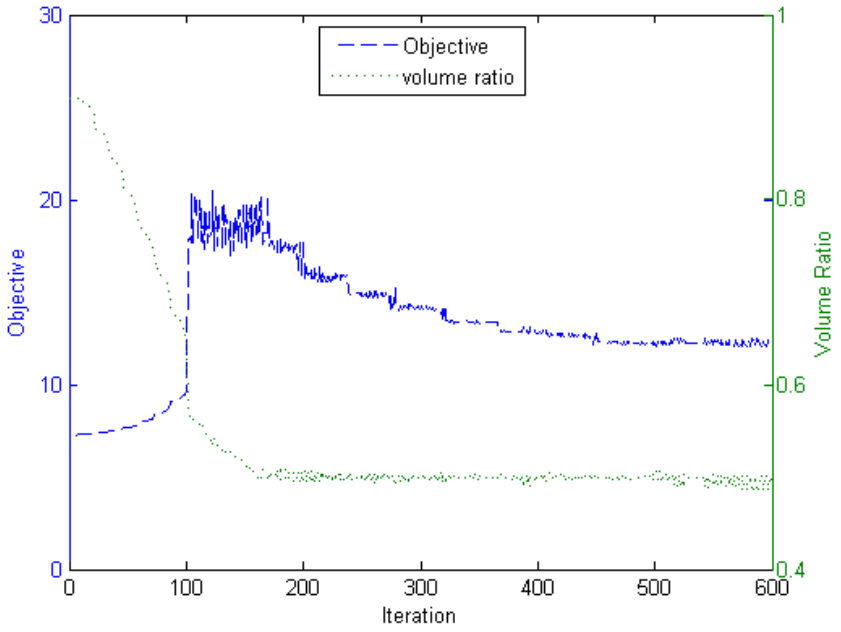

Fig. 5.13 Convergence history

Again, the design process goes through two rounds of feature modeling and sizing optimization. For the first round, the feature modeling result is illustrated in Fig. 5.12b, and the sizing optimization result is presented in Fig. 5.12c. γ is assigned the value 1.3, and so the first round volume constraint is 0.65. For the second round, the drafting and extrusion dig one more hole and enrich external boundary representation as shown in Fig. 5.12d. The final optimal solution, as shown in Fig. 5.12(e-f), converges at the expected volume ratio of 0.5. The overall convergence history is demonstrated in Fig. 5.13.

Evolvement of the modeling history is similar to that shown in Fig. 5.11, so it is not re-presented here.

5.4.2 3D cantilever

In the previous cases, only the thin plate design problems are studied. They share the characteristic that the extrusion operation always produces through holes, while no compound hole/slot is generated. Therefore, in order to fully demonstrate the capability of the B-rep geometry based topology optimization, a 3D cantilever problem is studied in this sub-section

which employs the design domain size of 30*15*5. The related BCs are shown in Fig. 5.14, and the objective is still to derive the stiff design under the material volume constraint of 50 percent.

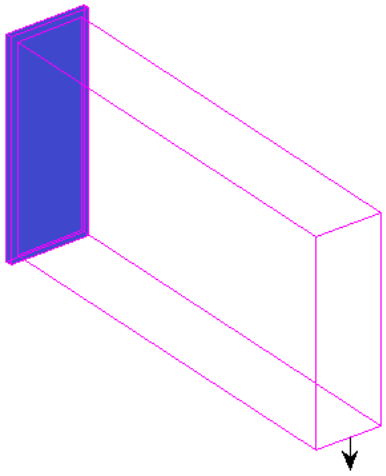

(a) Initial design domain and BCs

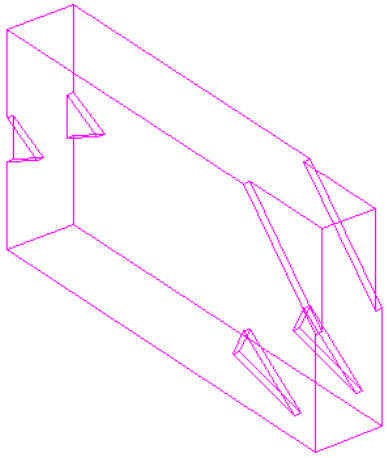

(b) Structure after the first round feature modeling

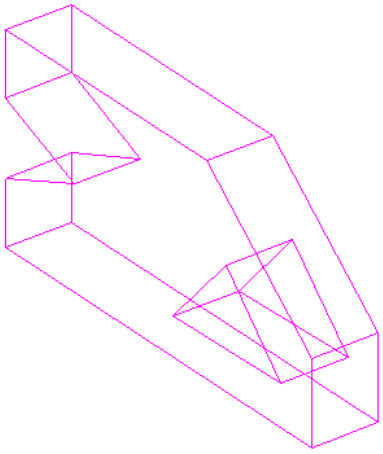

(c) Structure after the first round sizing optimization

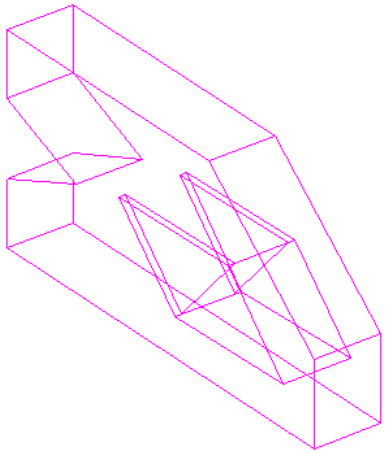

(d) Structure after the second round feature modeling

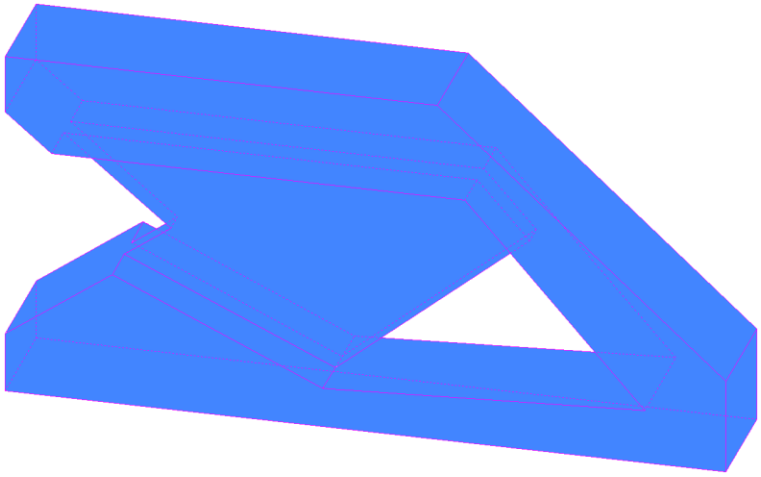

(e) The optimal solution

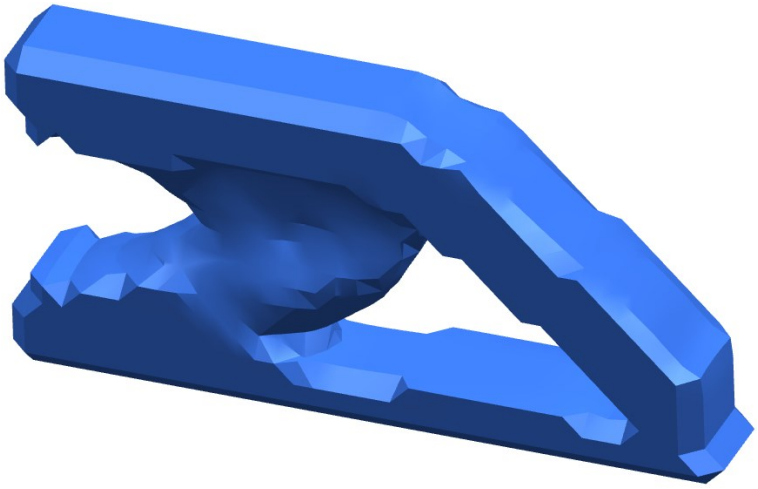

(f) Freeform topological design

Fig. 5.14 Automated inverse process

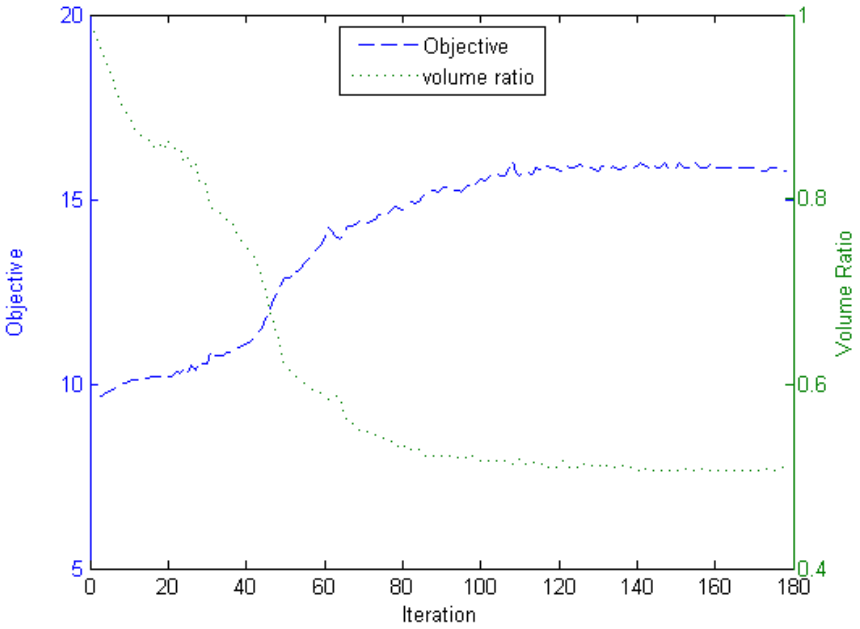

Fig. 5.15 Convergence history

The design process goes through two rounds of feature modeling and sizing optimization. The intermediate designs are presented in Fig. 5.14(b-d), and the final optimal solution is demonstrated in Fig. 5.14e. It is noted that γ is assigned the value 1.6, and so the first round volume constraint is 0.8. To properly evaluate the optimal solution, a discrete level set topology optimization process is performed and the freeform topological design is shown in Fig. 5.14f. Through comparison, there can draw the conclusion that the two optimal solutions are very similar in material distribution, and so they can be predicted of close stiffness performance.

The overall convergence history is presented in Fig. 5.15, and the final feature modeling history is shown in Fig. 5.16. It is noted that *f1*, *f2* represent the front and the back faces, respectively.

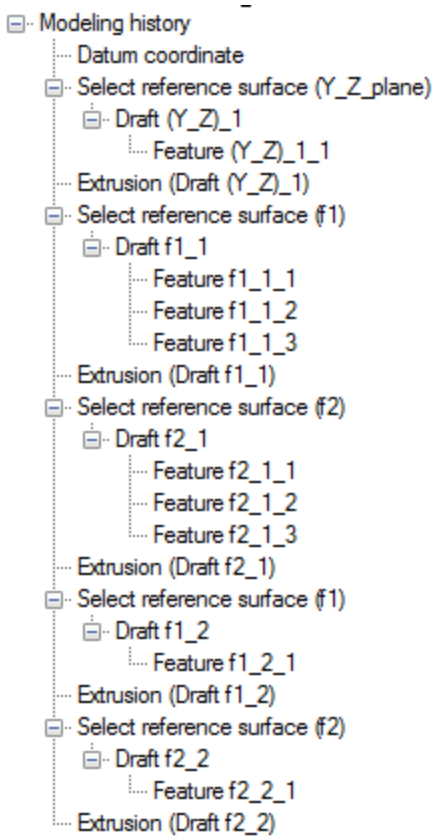

Fig. 5.16 Final feature modeling history

5.5 Conclusion

This Chapter investigates the CAD/CAE integration through FGFEM and B-rep geometry based topology optimization. Contributions have been made including the following technical improvements:

(1) The modified FGFEM is developed which achieves the balance between the computation efficiency of conventional FGFEM and the numerical accuracy of X-FEM.

(2) For the last, but the most important, the B-rep geometry based topology optimization method is developed to support the inverse integration. The benefit is clear that the geometry model and the analysis/optimization model are unified in B-rep format, which eliminates the mutual translation effort. For technical details, image processing is applied to interpret the SED distribution into certain drafting pattern; then, extrusion creates new feature primitives based on the drafting pattern; sizing optimization converges the sizing configuration into the final optimal

solution, and the boundary shape characteristics are maintained through the velocity field regulation.

For future work, more complex design schemes are to be investigated. For instance, the non-manifold B-rep model may be applied to represent complex BCs and distinguish the design and non-design domains; additionally, curved boundary segments are under exploration which would greatly enhance the current design capability.

Chapter 6 Optimization-for-manufacture

As introduced in Chapter 1, a new scheme of optimization-for-manufacture (OFM) is proposed to upgrade the conventional design-for-manufacture (DFM), in order to expedite the overall design flow and improve the design quality.

In Section 2.2, the available manufacture-oriented topology optimization methods have been reviewed, which attempts to make the topological design manufacturable. Chapter 3-5 demonstrated three different geometry feature-based approaches, but they never involved feature-attached engineering meanings. Therefore, in this chapter, the OFM scheme will be further development by involving the manufacturing feature-associated semantic information into the optimization process, which makes quantitative manufacturability evaluation (ME) possible.

6.1 Introduction to OFM

The design flow of OFM was presented in Fig. 1.2b. In this section, more details will be introduced:

1) For both functionality evaluation (FE) and manufacturability evaluation (ME), analytical expressions are mandatory and at least first-order derivation about the topological variables should be feasible, because deterministic optimization methods are preferred in implementation of OFM and the gradient information are necessary.

   In this work, 2.5D machining is the focus. Normally, 2.5D machining features employ the sectional profiles in regular shapes (2.5D form feature), e.g. rectangle, circle, or combinations. This type of profile is parametrically defined, and therefore, it is trivial to analytically express the associated FE and ME. On the other hand, the sectional profiles could be in freeform shapes (2.5D freeform feature), as well. They are defined by Splines, and numerous control points determine the exact shapes. In this situation, the non-intuitive relationship between the FE/ME and the control points makes it difficult to derive the analytical expressions. To fix this issue, discrete level set representation [Osher and Fedkiw 2003] is employed for the 2.5D freeform features. It is perfect for the OFM methodology, because the level set method has been actively applied to both cutting path

planning [Zhuang et al. 2010b; Shen et al. 2010] and design optimization [Wang et al. 2003; Allaire et al. 2004]. Both FE like structural stiffness, and ME like cutting path length, can be analytically expressed based on the level set function, regardless of the geometry's irregularity. Additionally, continuous first-order derivation is feasible. Details will be illustrated in the later sections

2) Then, about the optimization variables, sizing and shape parameters are commonly employed by structural optimization problems. For instance, Edke and Chang [2006] optimized the shape parameters through gradient based method to simultaneously improve the structural performance and reduce the manufacturing cost. However, topological changes cover the most design freedoms, and therefore, they theoretically enable the greatest functionality and manufacturability enhancement. Hence, topological variables (distributed level set values) are designated as the optimization target of the OFM methodology.
3) Configuration of the optimization problem is flexible. According to case based requirements, FE and ME can be configured into a single objective function, which makes it a multi-objective optimization problem. Or on the other way around, either FE or ME is applied as the objective function while the other one as the constraint. In either way, there is no significant difference in solution complexity.

Given the history of OFM, the early efforts focus on parametric sizing and shape optimization with simultaneously optimized functionality and manufacturability [Chang and Tang 2001; Edke and Chang 2006]. In the topology optimization field, there are efforts which guarantees the result is manufacturable [Zuo et al. 2006; Gersborg and Andreasen 2011; Guest and Zhu 2012; Lu and Chen 2012; Xia et al 2010a; Allaire et al. 2013]. However, quantitative involvement of ME is never addressed.

Therefore, this chapter develops the OFM methodology based on the level set topology optimization method. Material removal rate (MRR), the ratio of removed area/cutting path length, is applied as the ME criteria. It is analytically formulated based on the level set function through cutting path planning. Obviously, MRR marks the cutting efficiency and is expected to be maximized. Coupled with the structural compliance which is also expressed by the level set function, a weighted objective function and a multi-objective optimization problem could be

constructed. Through solution, the structural compliance and the cutting efficiency can be simultaneously optimized. During the optimization, local curvature of the feature profiles is constrained with an upper bound, which is determined by the smallest cutting tool radius. In this way, the topological design can be guaranteed manufacturable with the current cutting tool set.

6.2 Manufacturability improvement through single-sided curvature flow

6.2.1 Level set based cutting path planning

For 2.5D machining, cutting path planning employs two general patterns: zig-zag and parallel-offset. The latter is employed in this work for its simplicity and popularity (Bieterman and Sandstrom 2003). With the parallel-offset pattern, cutting paths follow the sectional profile of the removed volume, and can be directly derived through profile offset. Several numerical methods have been developed for the offset, and level set method is just an effective and efficient one.

Level set method defines the design domain discretely on the mesh nodes, and Eq. (6.1) is solved to initialize the nodal values as a signed distance field, as shown in Fig. 6.2a.

$$|\nabla \Phi(\boldsymbol{X})| = 1 \tag{6.1}$$

In this way, the nodal values offer the closest distance information of any point to the structural boundary (zero-value level set contour), as well as the sign which marks the point with solid material (positive) or material to be removed (negative). Therefore, as shown in Fig. 6.2a, the cutting paths could be naturally generated with the negative-value level set contours, and interval between neighboring contours is decided by the cutting tool radius (with the assumption that the feedrate is equal to radius of the cutting tool).

The benefit of level set cutting path planning is clear that, the employed signed distance field can make the profile offset naturally happen, and some conventional problems such as path singularity and self-interaction can be avoided (Shen et al. 2010).

Some cutting related information can be analytically expressed as:

$$Removed\ area = \int_D H(-\Phi)d\Omega$$

$$Cutting\ path\ length = \int_D \delta(-\Phi - R)d\Omega + \int_D \delta(-\Phi - 2R)d\Omega + \int_D \delta(-\Phi - 3R)d\Omega \ldots \quad (6.2)$$

in which R is the cutting tool radius.

6.2.2 Cutting efficiency improvement

The cutting related evaluations in Eq. (6.2) cannot be individually applied as the ME; instead, the MRR is more meaningful as it clearly marks the cutting efficiency. Therefore, to simultaneously maximize the stiffness and improve the cutting efficiency, the objective function of the compliance minimization problem is changed into:

$$Min. J(\boldsymbol{u}, \Phi) = \int_D \frac{1}{2}\boldsymbol{D}\boldsymbol{e}(\boldsymbol{u})\boldsymbol{e}(\boldsymbol{u})H(\Phi)d\Omega - w \cdot Removed\ area/Cutting\ path\ length \quad (6.3)$$

in which w is a weighting factor.

To solve the new optimization problem, sensitivity analysis is mandatory. However, in Eq. (6.3), it is non-trivial to calculate the sensitivity result about the second term and perform the related design update, because of its high non-linearity. To fix this issue, a novel approach is developed to eliminate the need of sensitivity analysis about the second term in Eq. (6.3), while still properly perform the design update.

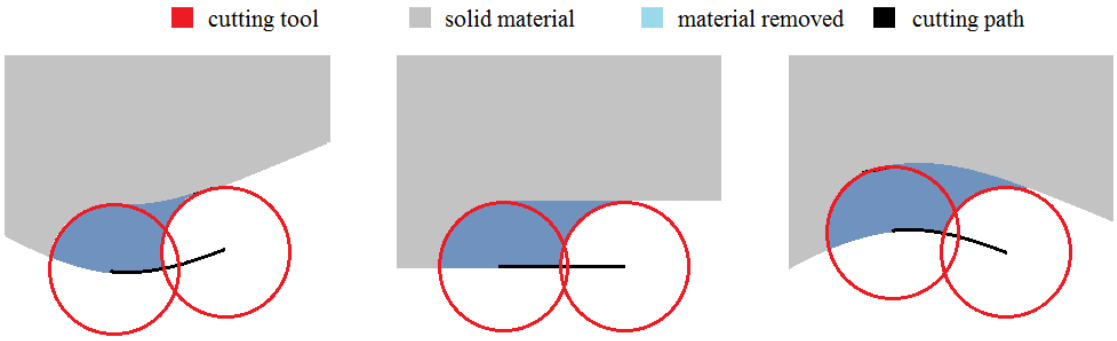

(a) $\kappa < 0$ (b) $\kappa = 0$ (c) $\kappa > 0$

Fig. 6.1 Relationship between MRR and the local cutting path curvature

In Fig. 6.1, the relationship between MRR and the local cutting path curvature is demonstrated. It can be seen that, under the same cutting speed and feed rate, MRR is in proportion to the local cutting path curvature, which means big local curvature is preferred given high cutting efficiency. Therefore, by increasing the mean curvature, the overall cutting efficiency could be improved.

Under the level set framework, curvature flow is an important mechanism of interface control. As introduced in [Osher and Fedkiw 2003], Eq. (6.4) is applied to realize the mean curvature flow, in which b is a positive constant and κ is the curvature. If $\kappa > 0$, the interface will move in the direction of concavity; and if $\kappa < 0$, the interface will move in the direction of convexity.

$$\begin{gathered} \boldsymbol{v} = -b\kappa\boldsymbol{n} \\ \kappa = \nabla \cdot \boldsymbol{n} = \nabla \cdot \left(-\frac{\nabla \Phi(\boldsymbol{X})}{|\nabla \Phi(\boldsymbol{X})|}\right) \end{gathered} \tag{6.4}$$

An example of the mean curvature flow is demonstrated in Fig. 6.2, and the flow drives the curvature to be evenly distributed. However, mean curvature flow cannot achieve the effect of mean curvature increase. A new curvature flow control method is needed and therefore is developed in this work. Details will be illustrated in next sub-section.

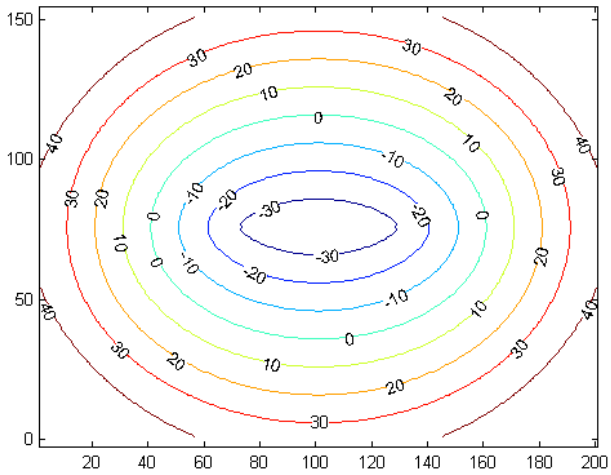

(a) The initial level set contours

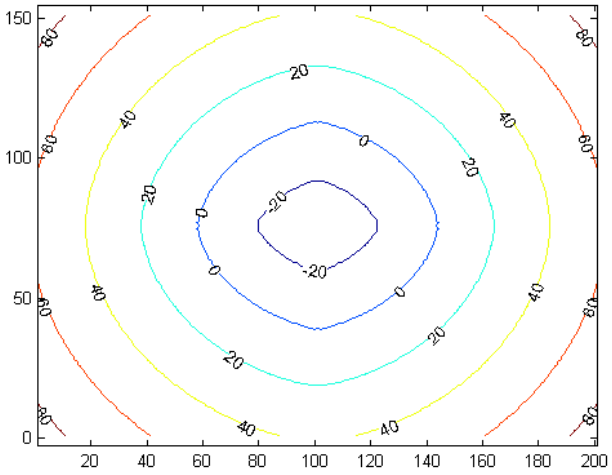

(b) Result of the mean curvature flow

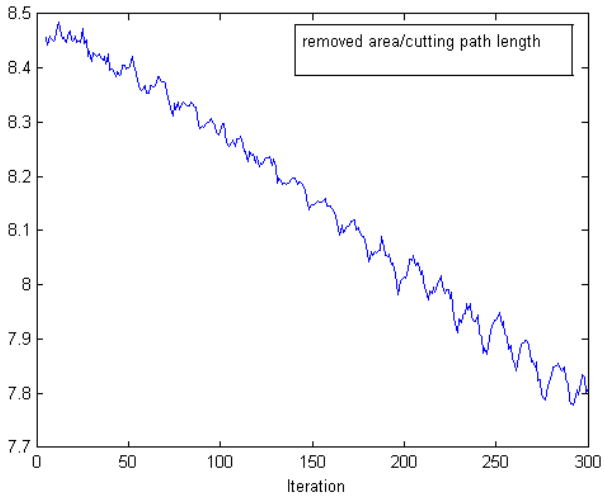

(c) History of MRR

Fig. 6.2 Mean curvature flow

6.2.3 Single-sided curvature flow

As shown in Fig. 6.2a, curvature distribution among the contours follow a similar pattern of the zero-value contour, which indicates that mean curvature of all cutting contours can be increased by simply increasing that of the zero-value level set contour [Zhuang et al. 2010b]. To achieve this goal, single-sided curvature flow would work, as shown in Eq. (6.5). Different from Eq. (6.4), *b* is not designed as a constant; instead, it is positive when local curvature is negative, and

it is negative when local curvature is positive. In this way, regardless of the sign, all local curvature will change in the incremental direction.

$$\begin{gathered} \boldsymbol{v} = -b\kappa\boldsymbol{n} \\ b < 0 \quad if \quad \kappa > 0 \\ b > 0 \quad if \quad \kappa < 0 \end{gathered} \tag{6.5}$$

Additionally, constraint on the maximum local curvature is mandatory for two reasons. First, the numerical process may be unstable because of the unconstrained curvature increase. For instance, in Fig. 6.3, result of the unconstrained evolvement from Fig. 6.2a is demonstrated and it is unreasonable as a cutting path for the many small branches. Second, it is physically interpretable because there is generally a lower bound of cutting tool radius of which the reciprocal is just the upper bound of maximum local curvature. Therefore, the maximum local curvature constraint is formulated as:

$$\kappa < \overline{\kappa} = 1/\underline{R} \tag{6.6}$$

in which $\underline{R}$ is the lower bound of cutting tool radius and $\overline{\kappa}$ is the upper bound of maximum local curvature.

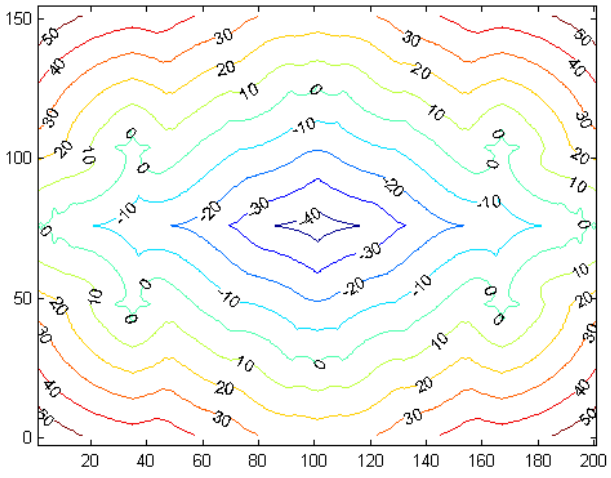

Fig. 6.3 Single-sided curvature flow without constraint

In Fig. 6.4, result of the constrained evolvement from Fig. 6.2a is demonstrated. In order to compare the mean curvature flow and the single-sided curvature flow, the MRRs are tracked for both evolvement processes and the histories are presented in Fig. 6.2c and Fig. 6.4b, respectively.

It can be clearly seen that, MRR of the mean curvature flow is decreasing which means reducing cutting efficiency; instead, MRR of the single sided curvature flow keeps increasing which conforms to our expectation.

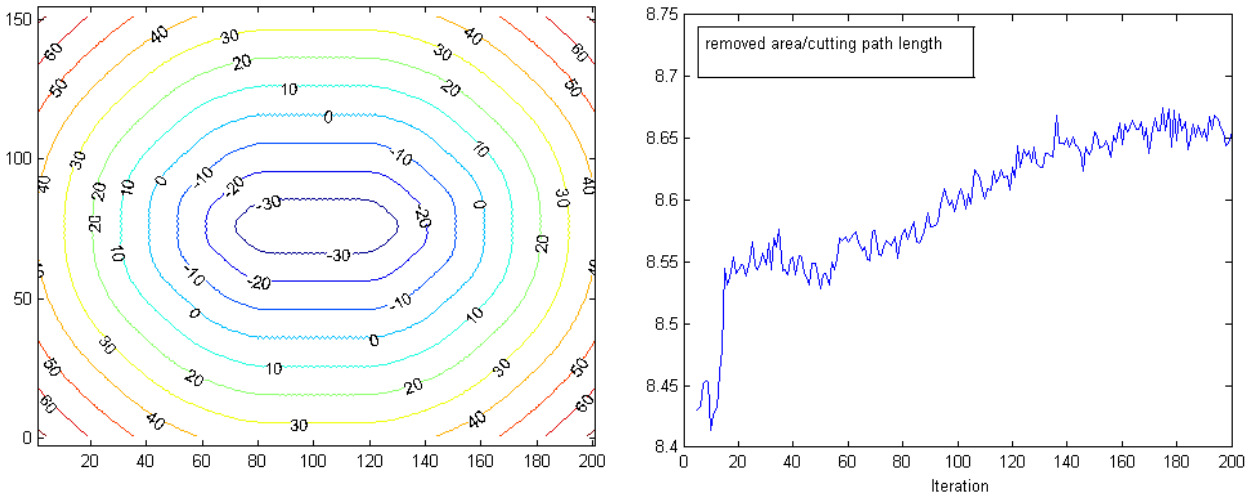

(a) Result of the single-sided curvature flow (b) History of MRR

Fig. 6.4 Single-sided curvature flow with constraint ($\overline{\kappa} = 0.1$)

6.2.4 The convection-diffusion equation

As mentioned in [Osher and Fedkiw 2003], by involving the curvature flow into the conventional level set topology optimization method, the Hamilton-Jacobi equation is adapted into the convection-diffusion format, that:

$$\Phi_t + \boldsymbol{V} \cdot \nabla\Phi = b\kappa|\nabla\Phi| \tag{6.7}$$

6.3 Case studies

6.3.1 The Michell structure case

First, the benchmark Michell structure case is studied. In Fig. 6.5a, the initial boundary condition is demonstrated. The two bottom ends are fixed and a unit force is loaded in the bottom center. The homogeneous material employs the Young's Modulus of 1.3 and the Poisson ratio of 0.4. In Fig. 6.5b, the initial level set field is shown. A few holes are predefined in the design domain as

extra boundaries for structural evolvement. The optimization problem is designed to minimize the structural compliance under the maximum volume constraint of 0.4. The single-sided curvature flow will be incorporated into the optimization process, and different upper bounds of the maximum local curvature will be applied.

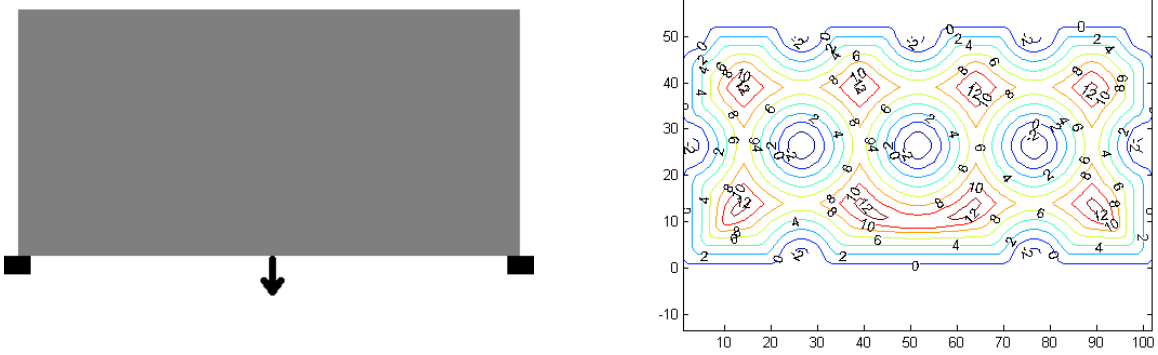

(a) Initial design domain and boundary conditions

(b) Initial level set field

Fig. 6.5 Initial setup of the Michell structure case

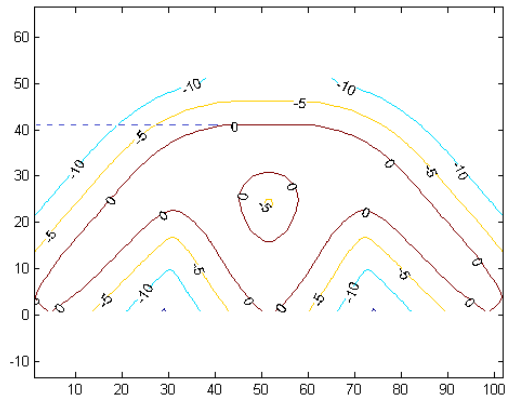

(a) No curvature flow control (obj = 6.48)

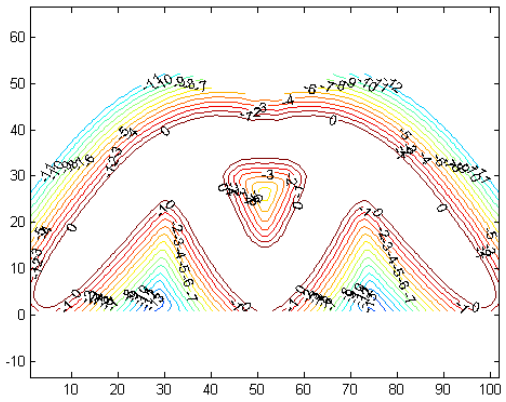

(b) $\underline{R} = 1$ (obj = 6.63)

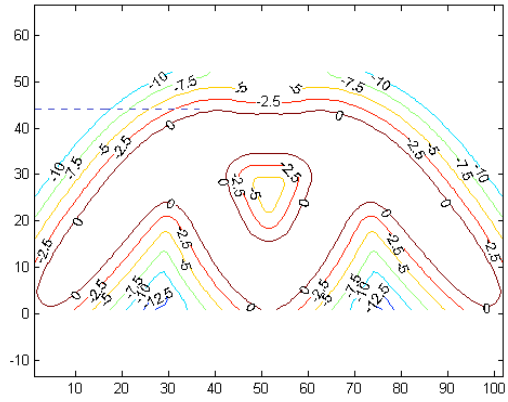

(c) $\underline{R} = 2.5$ (obj = 6.66)

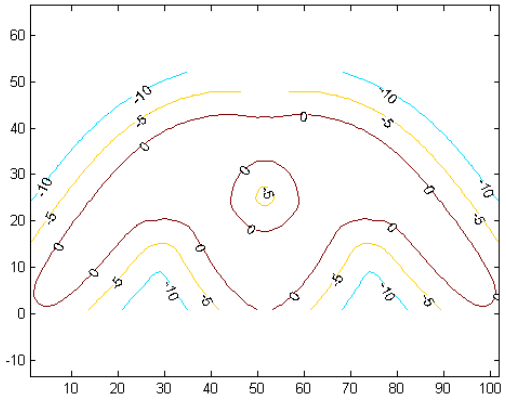

(d) $\underline{R} = 5$ (obj = 6.69)

Fig. 6.6 Optimization results with different upper bounds of the maximum local curvature constraint

The optimization results are demonstrated in Fig. 6.6, about which a few discussions are made below:

1. As shown in Fig. 6.6, incorporation of the single-sided curvature flow scarifies the result optimality, and this is under expectation because of the problem's multi-objective nature.
2. Through qualitative analysis of the optimization results shown in Fig. 6.6, it can be observed that the top edges of the optimized structures in Fig. 6.6(b-d) are measured of approximately 44 in vertical coordinate; in contrast, the top edge of the optimized

structure in Fig. 6.6a is only about 41. Then, it is concluded that incorporation of the single-sided curvature flow reduces the cutting area on top of the structure (see Fig. 6.6(b-d)), where the cutting paths employ negative curvatures and low cutting efficiency; and reversely, the cutting area with positive path curvatures increases given the consistent overall removed area. Therefore, the overall cutting efficiency increases by incorporating the single-sided curvature flow.

3. Quantitatively, cutting efficiency is measured by MRR. For Fig. 6.6(b-d), different cutting tool radiuses are applied, and correspondingly, the MRRs are calculated according to Eq. (10) and the specific $\underline{R}$ values. The calculated MRRs are shown in Table 6.1. To emphasize the manufacturability improvement, the MRRs are also calculated on the optimization result without curvature flow control (Fig. 6.6a) with the same $\underline{R}$ values, and the numbers are also listed in Table 6.1.

   Through comparison of the two sets of data, an increase rate of 1.58%, 3.09%, and 4.21% have been achieved with the $\underline{R}$ values of 1, 2.5, and 5, respectively. It is observed that the cutting efficiency improvement is more obvious with bigger cutting tool radius.

Table 6.1 MRR improvement

	$\underline{R} = 1$	$\underline{R} = 2.5$	$\underline{R} = 5$
MRR without curvature flow control	0.9553	2.5639	5.8627
MRR with single-sided curvature flow control	0.9704	2.6431	6.1094
MRR increase rate	1.58%	3.09%	4.21%

4. The maximum local curvature constraint is strictly satisfied in Fig. 6.6(b-d) with different upper bounds.

6.3.2 The cantilever case

In Fig. 6.7a, the initial boundary condition is demonstrated. The left side is fixed and a unit force is loaded in the bottom center. The homogeneous material employs the Young's Modulus of 1.3 and the Poisson ratio of 0.4. In Fig. 6.7b, the initial level set field is shown. A few holes are

predefined inside the design domain as extra boundaries for structure evolvement. The optimization problem is designed to minimize the structural compliance under the maximum volume constraint of 0.5. The single-sided curvature flow will be incorporated into the optimization process, and the same upper bounds of the maximum local curvature as used in the last case will be re-applied.

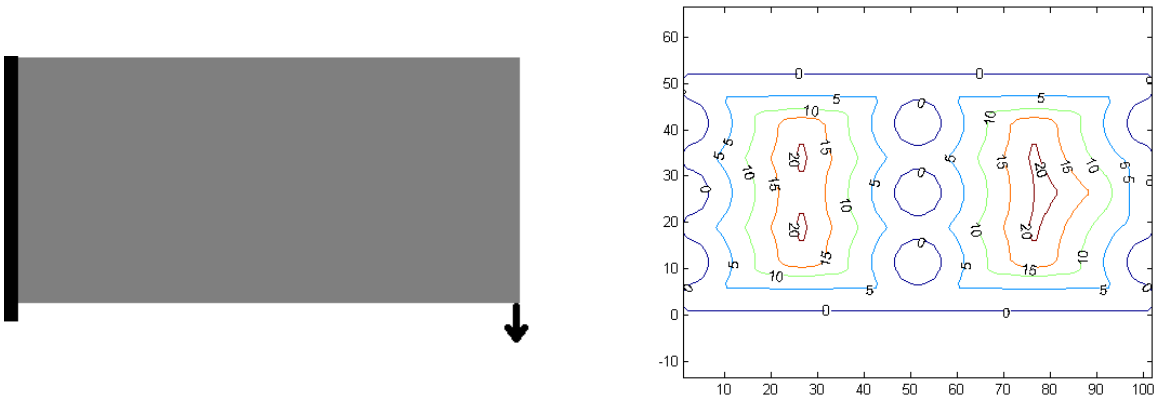

(a) Initial design domain and boundary conditions

(b) Initial level set field

Fig. 6.7 Initial setup of the cantilever case

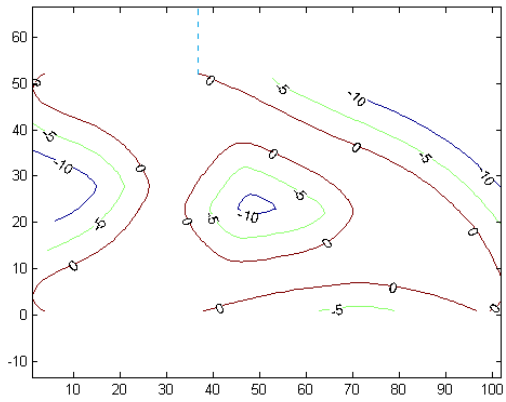

(a) No curvature flow control (obj = 61.94)

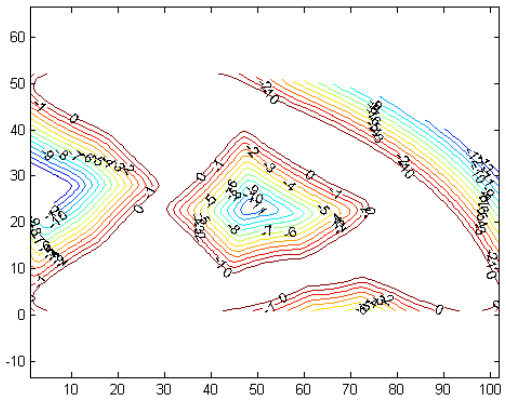

(b) $\underline{R} = 1$ (obj = 63.01)

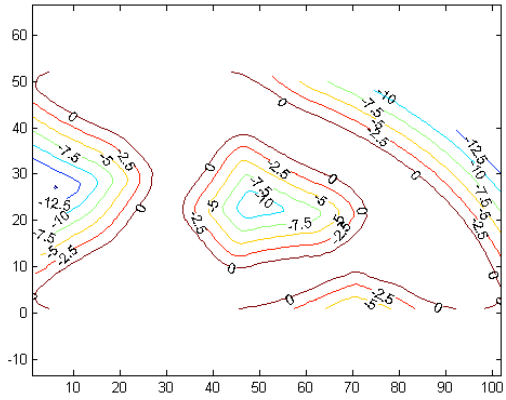

(c) $\underline{R} = 2.5$ (obj = 62.93)

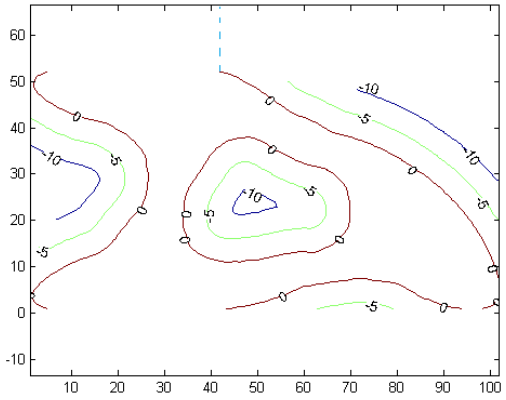

(d) $\underline{R} = 5$ (obj = 62.06)

Fig. 6.8 Optimization results with different upper bounds of the maximum local curvature

The optimization results are demonstrated in Fig. 6.8, about which a few discussions are made below:

1. As shown in Fig. 6.8, incorporation of the single-sided curvature flow scarifies the result optimality, and this is under expectation because of the problem's multi-objective nature.
2. Through qualitative analysis of the optimization results as shown in Fig. 6.8, it can be observed that the cutting paths in the top-right void employ negative curvatures which mean low cutting efficiency. In Fig. 6.8(b-d), incorporation of the single-sided curvature flow reduces the area of it, especially compared to the result in Fig. 6.8a without

curvature flow control. This can be interpreted as improvement of the overall cutting efficiency.

3. Quantitatively, cutting efficiency is measured by MRR. For Fig. 6.8(b-d), different cutting tool radiuses are applied, and correspondingly, the MRRs are calculated according to Eq. (6.2) and the specific $\underline{R}$ values. The calculated MRRs are shown in Table 6.2. To emphasize the manufacturability improvement, the MRRs are also calculated on the optimization result without curvature flow control (Fig. 6.8a) with the same $\underline{R}$ values, and the numbers are also listed in Table 6.2.

   Through comparison of the two sets of data, an increase rate of 1.04%, 1.60%, and 1.64% have been achieved with the $\underline{R}$ values of 1, 2.5, and 5, respectively. Again, it is observed that the cutting efficiency improvement is more obvious with bigger cutting tool radius.

4. The maximum local curvature constraint is strictly satisfied in Fig. 6.8(b-d) with different upper bounds.

Table 6.2 MRR improvement

	$\underline{R} = 1$	$\underline{R} = 2.5$	$\underline{R} = 5$
MRR without curvature flow control	0.9732	2.7170	6.4228
MRR with single-sided curvature flow control	0.9833	2.7605	6.5283
MRR increase rate	1.04%	1.60%	1.64%

6.4 Technical improvement

In Section 6.3, incorporating the single-sided curvature flow has improved manufacturability. However, it is also observed that, the improvement is case-based and sometimes not very obvious. For the reason, the authors believe that the current single-sided curvature flow control is not consistently effective to the positive-curvature area.

As presented in Eq. (6.5), the curvature flow velocity is proportional to the local curvature value. Therefore, for the negative-curvature area, the curvature-dependent velocities could accelerate

the curvature change in a positive direction (see Fig. 6.9a); however, for positive-curvature area, the curvature-dependent velocities could intensify the uneven curvature distribution (see Fig. 6.9b) which may cause failure of the overall curvature increase. To fix this issue, the authors applied a weighting function to normalize the positive curvatures.

(a) Negative curvature (b) Positive curvature

Fig. 6.9 Curvature-dependent velocities

The weighting function is (Guest et al. 2004; Dunning et al. 2011):

$$\kappa^N(\boldsymbol{X}) = \frac{\sum_{i\in S}\kappa^i(\boldsymbol{X}^i)\omega(\boldsymbol{X}^i,\boldsymbol{X})}{\sum_{i\in S}\omega(\boldsymbol{X}^i,\boldsymbol{X})}$$
$$\omega(\boldsymbol{X}^i,\boldsymbol{X}) = \begin{cases} \dfrac{r-|\boldsymbol{X}^i-\boldsymbol{X}|}{r} & if\ \boldsymbol{X}^i \in S \\ 0 & otherwise \end{cases} \tag{6.8}$$

in which, S and r represent the circular area (with center $\boldsymbol{X}$) and its radius, respectively; $\boldsymbol{X}$ and $\kappa^N(\boldsymbol{X})$ mean the coordinates and the normalized curvature of point $\boldsymbol{X}$; and $\boldsymbol{X}^i$ and $\kappa^i(\boldsymbol{X}^i)$ mean the coordinates and the curvature of the ith point located inside the circular area. Through normalization, the curvature of each point $\boldsymbol{X}$ is normalized and the uneven curvature distribution could be alleviated, which reduces the numerical instability of applying the single-sided curvature flow. It is noticing that, the normalization will only happen to the positive-curvature areas.

With the normalization, the cantilever example is re-studied with $\underline{R} = 5$, and the optimization result is shown in Fig. 6.10. It can be observed that, the negative-curvature area is drastically reduced compared to Fig. 6.8d, and the MRR is 7.0667 which means an increase rate of 10.03%

compared to the result in Fig. 6.8a. However, the maximum local curvature constraint is slightly violated in some areas, and this issue will be fixed in our future work.

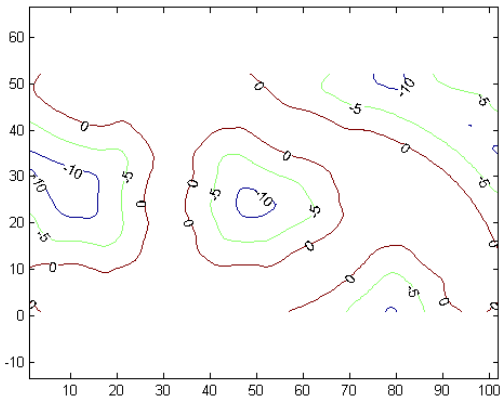

Fig. 6.10 Optimization result with normalized positive curvatures

6.5 Conclusion

This chapter introduces a novel OFM methodology, and related technical details are deeply discussed. Conceptually, OFM configures both functionality and manufacturability requirements into a single optimization problem. Through solution of this problem, both aspects can be optimally and concurrently satisfied. The authors believe that OFM will benefit the design community with a high level of design automation, and also the guaranteed design quality. Very likely, it could partially replace DFM in the near future.

A specific implementation of OFM is demonstrated. A novel, hybrid application of level set topology optimization and level set cutting path planning is carefully investigated. Especially for the latter, MRR is formulated based on the level set function to mark the cutting efficiency. Additionally, the single-sided curvature flow is developed to replace the complex sensitivity analysis for proper design update. To the authors' knowledge, these two techniques have never been simultaneously-applied for multi-objective problem solving. According to the numerical results, the hybrid application can simultaneously improve the cutting efficiency and enhance the structural stiffness. Moreover, some non-manufacturable details such as very big local curvature are eliminated by adding extra constraints.

Chapter 7 Two-scale extension to injection molding part design

The previous chapters have presented the feature-based topology optimization methods given the background of machining and injection molding. These methods share the commonality that they deal with homogeneous materials only, while heterogeneous objects are not investigated. In fact, for injection molding plastic parts, heterogeneous material distribution is increasing in popularity, e.g. the multi-material plastic part and the fiber reinforced plastic part. Therefore, this chapter will focus on the fiber-reinforced plastic part design and make the two-scale extension of the level set topology optimization.

7.1 Design of fiber-reinforcement

Fiber-reinforced plastics are popular these days, and widely applied in designing light-weighted parts with superior mechanical properties, such as "components of automobiles, housings of electrical devices and internal structural components of precision instruments" [Yashiro et al. 2011].

However, design of fiber-reinforced plastic parts is still in an immature state. The industrial practice mainly explores the experience-based approach, which is partially supported by commercial software tools. For instance, the ratio of fiber added is manually determined based on the functional requirement, and used as the input for injection molding simulation; software tools like Moldflow® and Moldex3D® can estimate the fiber orientation and output the result to structural analysis tools such as NX Nastran® or Ansys Workbench®; based on the structural analysis result, it is manually determined again whether to change the ratio or to improve the injection molding process parameters; the procedures above will be repeated until satisfaction. The current design practice is quite ineffective and nearly impossible to find the structural optimum, as well as the optimal fiber orientation distribution. From the authors' opinion, the reason leading to the current status is the lack of Computer-Aided Conceptual Design (CACD), as well as the immaturity of the CACD/CAD/CAE integrated design framework.

The introduction of fiber-reinforcement complicates the CACD stage and is time-consuming, because fiber orientation distribution needs to be accurately decided to satisfy the mechanical requirement under the minimum fiber consumption, which is almost impossible to determine manually. An appropriate method satisfying this scheme is free material optimization (FMO), which conventionally exists as a branch of topology optimization. For FMO, the optimization variables are the local material density, as well as the discrete elastic stiffness tensor; therefore, the structure design, as well as the locally attainable materials can be decided simultaneously [Kocvara et al. 2008]. Currently, the works on FMO are mainly developed under the density-based framework [Bendsoe et al. 1994; Pedersen and Pedersen 2013; Bruggi and Taliercio 2013], for which blurred structural boundary and intermediate densities exist in the result which makes it difficult to be directly-usable. In this work, FMO is re-developed under the level set framework, because of its clear-cut boundary representation and the pure "black and white" design [Wang et al. 2003; Allaire et al. 2004]. Correspondingly, the level set geometry and material optimization method is developed, and will be employed as the main component of the CACD module.

The CACD/CAD/CAE integration emerges as another problem to be solved. As mentioned earlier, the current design practice employs all the individual engineering modules; however, too many subjective decisions are needed to make them work as a system, which negatively influences the design efficiency and quality. The system framework should be re-produced with more automated design modules, as well as more objective decision makings.

7.2 CACD/CAD/CAE integrated design framework

Conventionally, research efforts mainly focus CAD/CAE integrated design frameworks [Hamri et al. 2010; Wang et al. 2014]; but for fiber-reinforced plastic parts, the CACD, CAD, structural analysis CAE, injection molding CAE are all indispensable engineering modules. Therefore, a well-defined system framework of integrating these modules is extremely important but is still absent. Hence, a new system framework is defined in Fig. 7.1. Individual modules and the systematic workflow will be introduced in details in the following paragraphs.

The CACD module employs the level set geometry and material optimization method, which produces the optimal conceptual design, including both the geometric feature model and the fiber

orientation distribution. Therefore, this is the initial step producing the complete information to form the heterogeneous object (HO) model.

Then, the CAD module reads in the HO model. Normally, there could be more design details to be manually completed which cannot be addressed in the CACD stage.

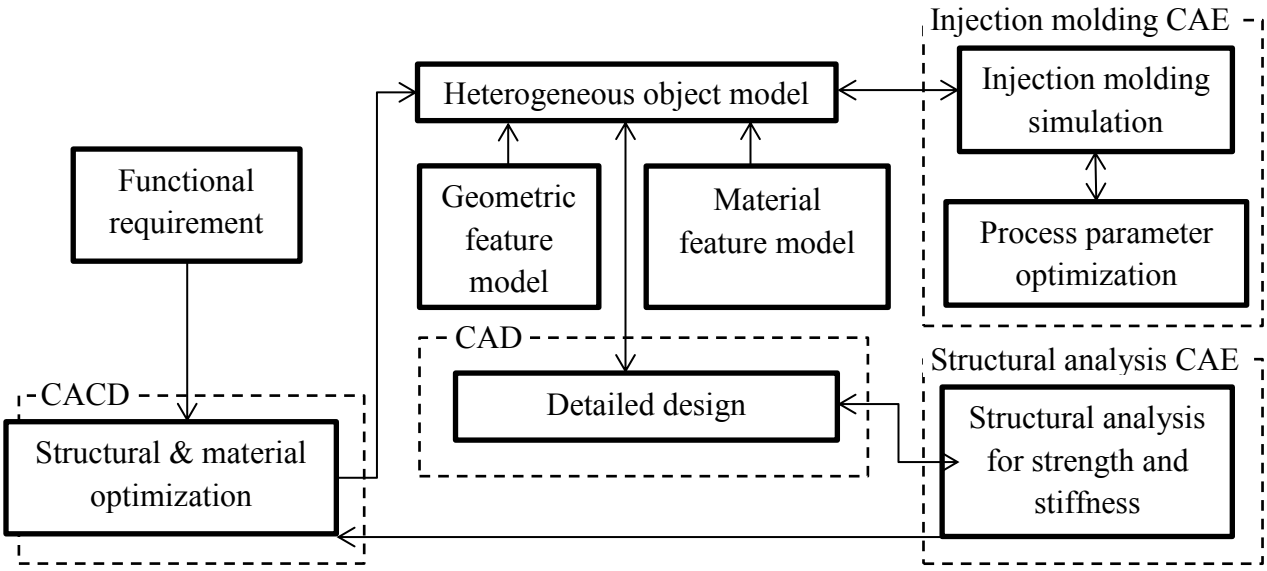

Fig. 7.1 CACD/CAD/CAE integrated design framework

The injection molding CAE module imports the geometric feature model and part of the material feature model. Then, injection molding simulation is performed, through which the most-likely fiber orientation distribution can be predicted; definitely, the predicted distribution will be different from the optimal solution. However, injection molding process parameters can be controlled to globally re-distribute the fibers. Another optimization process based on RSM (Response surface method) will be performed to find the best-suit process parameters, which approach the predicted fiber orientation distribution to the optimal solution.

The structural analysis CAE module supports the CACD module, and also functions to validate the final structural strength and stiffness. Normally, the fiber orientation distribution predicted by the injection molding process is in some degree distinct from the optimal solution, even after the RSM-based optimization. Therefore, a validation procedure is necessary before end of the design process.

It can be summarized that, all modules in this system share a common HO model, and they together form a complete and effective design process, not only satisfying the design requirements, but also deriving the close-to-optimum result. Design automation is realized in certain stages of this process, and dependency on manual decisions has been evidently reduced, both of which contribute to shorten the design process.

7.3 Heterogeneous object modeling

Heterogeneous object (HO) modeling is important for this integrated design framework, and actually, it is an active research field because of the extensive use of composite materials. As reviewed by [Kou and Tan 2007b], extensive research works have been done in the past two decades, and several HO models have been developed.

Voxel-based models [Jackson et al. 1999; Wu et al. 2008; Wang et al. 2009] discretize the geometry into voxels or the finite element mesh, and then impose constant or gradient material properties on each element. Therefore, the voxel-based models are suitable to be directly used in finite element analysis, and are potential to capture the highly-irregular material composition distribution.

Cellular model is an alternative of the geometry discretization which belongs to a bigger scale. Kumar et al. [1999] applied the *r*-set to model the geometry, and divided it into sub-regions, each of which was mapped with certain material class. Later, Shin and Dutta [2001] and Shin et al. [2003] presented a constructive representation of HOs by manipulating the heterogeneous primitives with heterogeneous Boolean operations. For cellular model, the material composition function is necessary for each cellular.

Control feature-based model, developed by Siu and Tan [2002], employed the source profile feature as reference, and distributed the FGMs according to the source-based material composition function. Later, the heterogeneous feature tree including multi-level source profile features, as well as the non-regular Boolean operations were applied for complex HO modeling [Kou and Tan 2005; Kou et al. 2006]. B-spline-based model can be regarded as an extension of the control feature-based model. Qian and Dutta [2004] proposed a feature-based approach for HO modeling, in which the form and material features were separately defined; the diffusion-based B-spline method was applied to determine the material composition distribution. Yang and

Qian [2007] applied the B-spline finite element method to unify the design and analysis model; the heterogeneous lofting algorithms were used to determine the material composition distribution between B-spline material profiles. Recently, Samanta et al. [2014] developed an optimization method for material composition blending between complex material directrices.

Other HO models like the distance field-based model [Biswas et al. 2004; Zhou et al. 2009] and the radial basis function-based model [Yoo 2013] are also robust in HO representation given certain scenarios.

In summary, two remaining issues were mentioned by [Kou and Tan 2007b]. First, the highly-irregular material composition distribution is still not well addressed, as the majority of HO models are designed for the multi-material or FGM distribution. The second issue is the poor integration of CAD/CAE/CAM. There is limited work addressing the CAD/CAE integration [Kou and Tan 2007a], and the efforts on CAD/CAM integration mainly focus on additive manufacturing. In this research, the concentration will be the modeling of fiber-reinforcement, which definitely belongs to the highly-irregular material composition distribution, and is manufactured through injection molding instead of additive manufacturing. Therefore, a new HO model is needed.

Level set model [Wang and Wang 2004; Wang and Wang 2005] is relatively a novel HO representation. To be specific, each level set function is a close contour which represents the material interface; because of overlapping, n level set functions can represent 2^n material phases, which make it extremely suitable for multi-material structures. Recently, the level set approach was also applied in representation and optimization of structures filled with FGMs [Xia and Wang 2008]; in their work, fixed mesh model is used to discretize the level set material area, and store the abundant local material composition information. Although the work of [Xia and Wang 2008] targets at structures with FGMs, it has demonstrated the potential of level set model in representing the highly-irregular material composition distribution. Additionally, it also offers an optimization approach to generate the highly-irregular material composition distribution without relying on sources or functions.

Therefore, the author proposes a new HO model -- the CAD-CAE associative feature model. This new HO model stores the geometry and material information separately: the geometric

feature model is built in the CAD module by using level set functions, while the material feature model depends on the fixed finite element mesh. By adopting the associative feature concept [Ma and Tong 2003; Ma et al. 2008], these two feature models are tightly bonded for complete information representation. Then, by developing the level set geometry and material optimization method, it enables the concurrent and optimal generation of the geometry and material information regardless of the complexity. Therefore, this new HO model is general in modeling the highly-irregular material composition distribution, as well as complex geometry.

The CAD-CAE associative feature model is different from the voxel based model, because the geometry and material information are simultaneously generated and independently stored, instead of generating the geometry first and then making the discretization and filling in with material information of the voxel-based model.

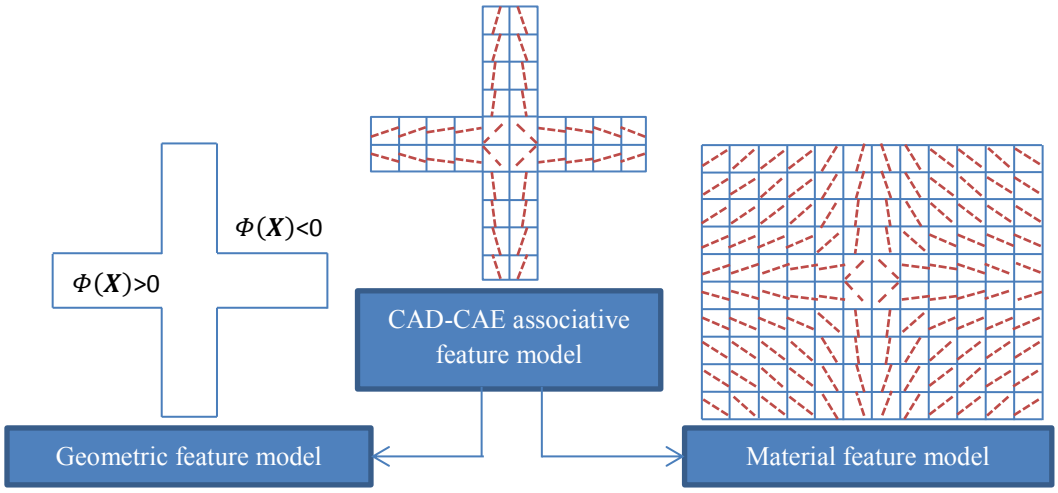

Fig. 7.2 CAD-CAE associative feature model

7.4 Computer-aided conceptual design

7.4.1 Strength-constrained optimization problem

For fiber-reinforced plastic, the mechanical properties are difficult to determine, as they are influenced by several factors, which include: the fiber type [Unterweger et al. 2014a; Unterweger et al. 2014b], the fiber/matrix interaction [Zhandarov and Mader 2005], and the fiber length and orientation distribution [Fu and Lauke 1996; Facca et al. 2007; Fotouh et al. 2014]. Taking fiber type for example, glass fiber (GF) is traditionally applied to enhance the strength and stiffness, as

well as the impact resistance; carbon fiber is popular as it can offer better enhancement in these mechanical properties; there are also other fiber types with smaller density which therefore can make even lighter-weighted structures; natural fiber is also frequently used as they are cost-effective and environmental-friendly [Fotouh et al. 2014]. However, in this chapter, the emphasis will be optimizing the fiber orientation distribution, instead of the exploration on the micromechanical properties of fiber-reinforced plastic. Therefore, a few simplifications are made about the mechanical model: first, the fiber properties are specified but not the exact fiber type; then, the fiber-matrix de-bonding is neglected for the sake of simplicity [Ghasemi et al. 2014], although this issue is solvable [Brighenti 2005; Birghenti and Scorza 2012; Gerdeen and Rorrer 2012].

Based on the homogenization theory, macro mechanical properties of the fiber-reinforced plastic could be determined [Brighenti 2005; Birghenti and Scorza 2012; Bruggi and Taliercio 2013; Ghasemi et al. 2014], and the elasticity tensor is,

$$\boldsymbol{D} = (1-\eta)\boldsymbol{D_0} + \eta \boldsymbol{D_{f0}} \tag{7.1}$$

where η represents the volume ratio of the fiber; $\boldsymbol{D_0}$ is the elasticity tensor of the isotropic matrix material and $\boldsymbol{D_{f0}}$ is the elasticity tensor of the fiber in case that the fiber direction coincides with the *x*-axis (as shown in Fig. 7.3a).

Specifically, $\boldsymbol{D_0}$ and $\boldsymbol{D_{f0}}$ are expressed by Eq. (7.2) and (7.3), in which E_{iso} and ν are the Young's modulus and Poisson ratio of the matrix material and E_{ani} is the Young's modulus of the fiber along the longitudinal direction.

$$\boldsymbol{D_0} = \frac{E_{iso}}{1-\nu^2}\begin{vmatrix} 1 & \nu & 0 \\ \nu & 1 & 0 \\ 0 & 0 & \dfrac{(1+\nu)}{2} \end{vmatrix} \tag{7.2}$$

$$\boldsymbol{D_{f0}} = \begin{vmatrix} E_{ani} & 0 & 0 \\ 0 & 0 & 0 \\ 0 & 0 & 0 \end{vmatrix} \tag{7.3}$$

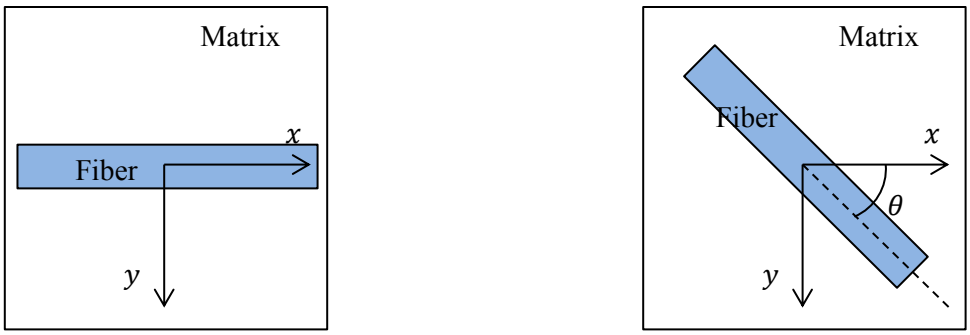

(a) (b)

Fig. 7.3 Fiber-reinforced material

Concerning the flexibility of the fiber orientation as shown in Fig. 7.3b, the transformation matrix $\boldsymbol{T}(\theta)$ is needed to conduct the coordinate transformation [Bruggi and Taliercio 2013].

$$\boldsymbol{T}(\theta) = \begin{vmatrix} cos^2\theta & sin^2\theta & -2cos\theta sin\theta \\ sin^2\theta & cos^2\theta & 2cos\theta sin\theta \\ cos\theta sin\theta & -cos\theta sin\theta & cos^2\theta - sin^2\theta \end{vmatrix} \tag{7.4}$$

Therefore, the elastic tensor of fiber in arbitrary orientation is transformed into,

$$\boldsymbol{D_f} = \boldsymbol{T}(\theta)\boldsymbol{D_{f0}}\boldsymbol{T}(\theta)^T \tag{7.5}$$

Consequently, the elastic tensor of the fiber-reinforced material is finalized as shown in Eq. (7.6), in which α is the volume ratio of the fiber contents.

$$\boldsymbol{D} = (1-\alpha)\boldsymbol{D_0} + \alpha\boldsymbol{D_f} \tag{7.6}$$

Another important point is the concept of strength, which is definitely complicated for anisotropic materials, instead of the direct von Mises measure for isotropic materials. Details about the failure criteria of anisotropic composite material are explored in [Hinton et al. 2004; Talreja 2014]. For the sake of simplicity, the elastic energy density (EED) is applied to measure the local strength following the work of [Pedersen and Pedersen 2013].

$$Q_e = \frac{1}{2}\boldsymbol{D}\boldsymbol{e}(\boldsymbol{u})\boldsymbol{e}(\boldsymbol{u}) \tag{7.7}$$

Therefore, the topology optimization problem of mass minimization under strength constraints is formulated as,

$$Min. \quad J(\Phi) = \int_D H(\Phi) d\Omega + \mu D_T(\Phi)$$

$$s.t. \quad a(\boldsymbol{u}, \boldsymbol{v}, \Phi) = l(\boldsymbol{v}, \Phi), \qquad \forall \boldsymbol{v} \in U$$

$$Q_e \leq Q_{lim} \qquad e = 1,2, \dots, m$$

$$D_T = \int_D \left\{ \left[\left(\Phi(\boldsymbol{X}) - \frac{T}{2} \right)^+ \right]^2 - \left[\left(\Phi(\boldsymbol{X}) - \frac{T}{2} \right)^- \right]^2 \right\} H(\Phi) d\Omega \tag{7.8}$$

The notations: $(f)^+ = max(f, 0);\ (f)^- = min(f, 0)$

$$a(\boldsymbol{u}, \boldsymbol{v}, \Phi) = \int_D \boldsymbol{De}(\boldsymbol{u}) \boldsymbol{e}(\boldsymbol{v}) H(\Phi) d\Omega$$

$$l(\boldsymbol{v}, \Phi) = \int_D \boldsymbol{pv} H(\Phi) d\Omega + \int_D \boldsymbol{\tau v} \delta(\Phi) |\nabla \Phi| d\Omega$$

In Eq. (7.8), the objective function is composed of two terms. The first term measures the material volume inside the design domain, which is to be minimized to save material. The second term $D_T(\Phi)$ is the thickness control functional which has been introduced in Chapter 3. The reason for employing the second term is that constant rib thickness is a necessary requirement of injection molding to ensure uniform cooling. μ is the weighting factor of the thickness control.

The first constraint is the weak form of the displacement field governing equation. The second constraint is the local strength constraint in which Q_e is the elementary EED measure, m is the total number of elements, and Q_{lim} is the maximum allowed local EED value. It is feasible to solve the local strength constraints even in high quantity; however, the relevant computational expense will be high. Therefore, in this work, the normalized p-norm functions [Le et al. 2010; Verbart et al. 2012] are adopted to transform the numerous local strength measures into one global strength measure, in this way to save computational effort without sacrificing the strength control accuracy.

$$cQ = c(\sum_{e=1}^{m} {Q_e}^p)^{\frac{1}{p}} \leq Q_{lim}$$
$$c^I = \frac{{Q_{max}}^{I-1}}{Q^{I-1}} \tag{7.9}$$

In Eq. (7.9), p is the norm parameter to construct the global measure and c is the normalization parameter to improve the accuracy of the global measure. Q_{max} represents the maximum local EED in the relevant iteration. The superscripts represent the iteration index.

In this work, the norm parameter $p = 8$ is used. As summarized by [Le et al. 2010], small p values cannot effectively capture the peak local EED; high p values require long iterations to converge and may cause some numerical problems. Therefore, p values of 6 to 8 are recommended. On the other hand, the normalized regional p-norm functions are recommended by the authors, because of better EED control accuracy. To be specific, the design domain is divided into regions based on the interlacing rule [Le et al. 2010; Verbart et al. 2012], which forms each region by clustering discrete EEDs spanning the whole EED range. Therefore, one global measure is divided into a few regional measures, which could more accurately evaluate the maximum local EED within each region. Additionally, the EED level based division method [Holmberg et al. 2013] is under exploration, which simply cluster the local EEDs into regions based on the EED levels. It has demonstrated the potential to flexibly control the EED distribution, because the clustering intervals are customizable and different control strategies could be applied to regions.

7.4.2 Sensitivity analysis

In order to solve the optimization problem, a sensitivity analysis is needed to derive the boundary velocity V_n to evolve the structure boundary in the steepest descent direction. In this section, the material derivative and the adjoint method are employed to perform the shape sensitivity analysis.

The Lagrange function of the optimization problem is defined in Eq. (7.10).

$$L = J(\Phi) + a(\boldsymbol{u}, \boldsymbol{w}, \Phi) - l(\boldsymbol{w}, \Phi) + \lambda[c\left(\int_D {Q_e}^p H(\Phi) d\Omega\right)^{\frac{1}{p}} - Q_{lim}] \tag{7.10}$$

Then, material derivative of the Lagrange function is given as,

$$L' = J'(\Phi) + a'(\boldsymbol{u}, \boldsymbol{w}, \Phi) - l'(\boldsymbol{w}, \Phi) + \lambda[c\left(\int_D {Q_e}^p H(\Phi) d\Omega\right)^{\frac{1}{p}}]' \tag{7.10}$$

in which,

$$J'(\Phi) = \int_D (1 + \mu G)\delta(\Phi) V_n |\nabla \Phi| d\Omega$$

$$G = \left[\left(\Phi(\boldsymbol{X}) - \frac{T}{2}\right)^+\right]^2 - \left[\left(\Phi(\boldsymbol{X}) - \frac{T}{2}\right)^-\right]^2 \tag{7.11}$$

$$+ \int_{ray_{\partial\Omega}(\boldsymbol{Y}) \cap \Omega} \left[2\left(\Phi(\boldsymbol{Z}) - \frac{T}{2}\right)^+ - 2\left(\Phi(\boldsymbol{Z}) - \frac{T}{2}\right)^-\right]\left(1 - d_\Omega(\boldsymbol{Z})\kappa(\boldsymbol{Y})\right) d\boldsymbol{Z}$$

$$\begin{aligned} a'(\boldsymbol{u}, \boldsymbol{w}, \Phi) &= \int_D [\boldsymbol{Ae}(\boldsymbol{u}')e(\boldsymbol{w}) + \boldsymbol{Ae}(\boldsymbol{u})\boldsymbol{e}(\boldsymbol{w}')] H(\Phi) d\Omega \\ &+ \int_D \boldsymbol{Ae}(\boldsymbol{u})\boldsymbol{e}(\boldsymbol{w})\delta(\Phi) V_n |\nabla \Phi| d\Omega \end{aligned} \tag{7.12}$$

$$\begin{aligned} l'(\boldsymbol{w}) &= \int_D \boldsymbol{p}\boldsymbol{w}' H(\Phi) d\Omega + \int_D [\boldsymbol{p}\boldsymbol{w} - \boldsymbol{\tau}\boldsymbol{w}\nabla \cdot (\frac{\nabla \Phi}{|\nabla \Phi|})]\delta(\Phi) V_n |\nabla \Phi| d\Omega \\ &+ \int_D \boldsymbol{\tau}\boldsymbol{w}'\delta(\Phi)|\nabla \Phi| d\Omega \end{aligned} \tag{7.13}$$

$$[c\left(\int_D {Q_e}^p H(\Phi) d\Omega\right)^{\frac{1}{p}}]' = K[\int_D {Q_e}^p \delta(\Phi) V_n |\nabla \Phi| d\Omega + \int_D p{Q_e}^{p-1} {Q_e}' H(\Phi) d\Omega] \tag{7.14}$$

$$K = \frac{c}{p}\left(\int_D {Q_e}^p H(\Phi) d\Omega\right)^{\frac{1}{p}-1}$$

$$Q_e' = \boldsymbol{Ae}(\boldsymbol{u}')\boldsymbol{e}(\boldsymbol{u})$$

Put Eq. (7.11-7.14) into Eq. (7.10). Collect all the terms including $\boldsymbol{w}'$, and the sum is shown in Eq. (7.15) which is naturally equal to zero.

$$\int_{\Omega} [\boldsymbol{Ae}(\boldsymbol{u})\boldsymbol{e}(\boldsymbol{w}') - \boldsymbol{pw}']H(\Phi)d\Omega - \int_{D} \boldsymbol{\tau w}'\delta(\Phi)|\nabla\Phi|d\Omega = 0 \tag{7.15}$$

Then, collect the terms containing $\boldsymbol{u}'$ and make the sum equal to zero, that is,

$$\int_{D} [\boldsymbol{Ae}(\boldsymbol{u}')\boldsymbol{e}(\boldsymbol{w}) + \lambda K p {Q_e}^{p-1}\boldsymbol{Ae}(\boldsymbol{u}')\boldsymbol{e}(\boldsymbol{u})]H(\Phi)d\Omega = 0 \tag{7.16}$$

Through solving Eq. (7.16), the solution of the adjoint variable $\boldsymbol{w}$ can be derived.

By collecting the remaining terms, the sensitivity analysis result is obtained as,

$$\begin{gathered} L' = \int_{D} \beta\delta(\Phi)V_n|\nabla\Phi|d\Omega \\ \beta = 1 + \mu G + \boldsymbol{Ae}(\boldsymbol{u})\boldsymbol{e}(\boldsymbol{w}) + \lambda K {Q_e}^{p} \end{gathered} \tag{7.17}$$

where β is the shape gradient density. Then, by following Eq. (7.18),

$$V_n = -\beta \tag{7.18}$$

L can be guaranteed to change in the descent direction, as shown in Eq. (7.19),

$$L' = \int_{D} -\beta^2\delta(\Phi)|\nabla\Phi|d\Omega \leq 0 \tag{7.19}$$

When come to the fiber orientations, the sensitivity analysis will be as,

$$\frac{\partial L}{\partial \theta} = \int_{D} [\frac{\partial \boldsymbol{A}}{\partial \theta}\boldsymbol{e}(\boldsymbol{u})\boldsymbol{e}(\boldsymbol{w}) + \lambda K p {Q_e}^{p-1}\frac{1}{2}\frac{\partial \boldsymbol{A}}{\partial \theta}\boldsymbol{e}(\boldsymbol{u})\boldsymbol{e}(\boldsymbol{u})]H(\Phi)d\Omega \tag{7.20}$$

Therefore, by following Eq. (7.21), the change of L can be guaranteed in the steepest descent direction as shown in Eq. (7.22).

$$\frac{\partial \theta}{\partial t} = -[\frac{\partial \boldsymbol{A}}{\partial \theta}\boldsymbol{e}(\boldsymbol{u})e(\boldsymbol{w}) + \lambda K p {Q_e}^{p-1}\frac{1}{2}\frac{\partial \boldsymbol{A}}{\partial \theta}\boldsymbol{e}(\boldsymbol{u})\boldsymbol{e}(\boldsymbol{u})] = \frac{1}{2}\lambda K p {Q_e}^{p-1}\boldsymbol{A}'\boldsymbol{e}(\boldsymbol{u})\boldsymbol{e}(\boldsymbol{u}) \tag{7.21}$$

where

$$\lambda K p {Q_e}^{p-1} \geq 0$$

$$\frac{\partial L}{\partial \theta}\frac{\partial \theta}{\partial t} = \int_D -[\frac{\partial \boldsymbol{A}}{\partial \theta}\boldsymbol{e}(\boldsymbol{u})\boldsymbol{e}(\boldsymbol{w}) + \lambda K p {Q_e}^{p-1}\frac{1}{2}\frac{\partial \boldsymbol{A}}{\partial \theta}\boldsymbol{e}(\boldsymbol{u})\boldsymbol{e}(\boldsymbol{u})]^2 H(\Phi)d\Omega \leq 0 \tag{7.22}$$

7.4.3 Design update and the optimal criteria

Design update through solving the Hamilton-Jacobi equation has been introduced earlier in Section 2.1, and therefore will not be repeated here.

On the other hand, the fiber orientations are updated by using Eq. (7.23).

$$\theta = \theta + \frac{\partial \theta}{\partial t}\Delta t \tag{7.23}$$

It should be noted that, the time interval used to update the fiber orientations is not necessarily identical to that of the level set function.

As for optimal criteria, $L' = 0$ and $cQ - Q_{lim} \leq 0$ should be satisfied. The former implies at least a local optimum, and the latter means the strength constraint is satisfied.

7.4.4 Overall flow chart

In summary of the complete numerical implementation procedures, it is a two-scale optimization problem of coupled geometry and material optimization. The overall flow chart is presented in Fig. 7.4.

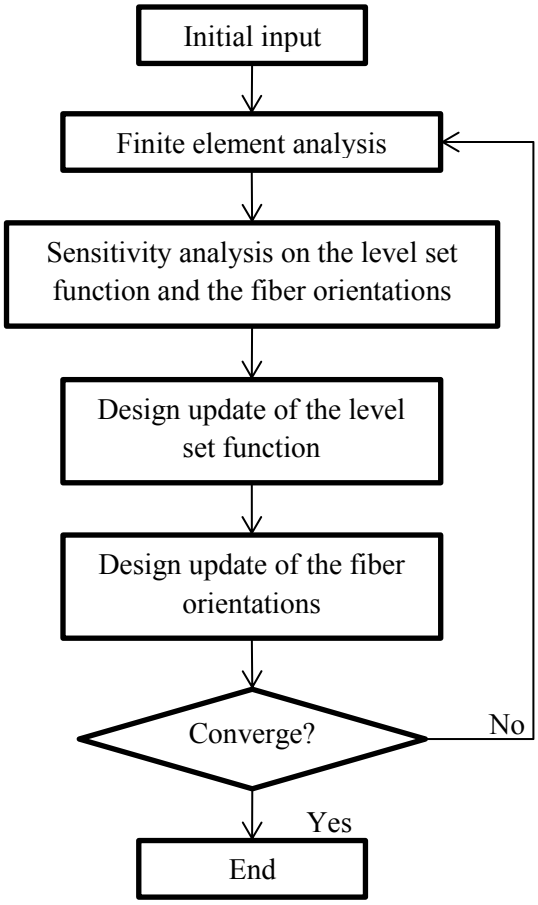

Fig. 7.4 Overall flow chart

7.5 Injection molding CAE

With fiber-reinforcement, the strength and resistance to deformation of the polymer can be greatly enhanced along the fiber orientation, while this is not the case for the normal direction. Therefore, control of the fiber orientation distribution to approach the designed pattern is significant in realizing the expected strength enhancement. As mentioned in [SadAbadi and Ghasemi 2007; Li et al. 2014], the fiber orientation can be easily induced along a given direction, and two important rules are generally followed,

(1) Shear flows tend to align fibers in the flow direction;

(2) Extensional flows tend to align fibers in the elongation direction.

Therefore, the fiber orientation is greatly influenced by the way the polymer flows through the mold, which is dependent on three general factors: rheology of the melt material, the injection

molding process parameters and also the mold geometry [SadAbadi and Ghasemi 2007; Li et al. 2014]. Concerning the accessibility, adjustment of the injection molding process parameters is commonly employed to control the fiber orientation distribution.

SadAbadi and Ghasemi [2007] evaluated the influence of process parameters including injection flow rate, mold wall temperature, packing pressure and also fiber content on the fiber orientation distribution; they drew the conclusion that the injection flow rate has more influence than mold wall temperature on the fiber orientation distribution, and packing pressure has almost no effect on it. Chen et al. [2011] used Taguchi methods to find the optimal setting of process parameters including the filling time, melt temperature, mold temperature, and injection speed to maximize the shear layer thickness. Li et al. [2014] reviewed the mold temperature's influence on the fiber orientation distribution.

Therefore, according to these previous works and also the authors' experience, four process parameters – the gate location, injection flow rate, mold temperature and melt temperature – all influence the fiber orientation distribution, and have been defined as the optimization variables.

RSM is employed in this work, as it is an effective tool for the optimization of injection molding process parameters [Tzeng et al. 2012]. RSM [Myers and Montgomery 1995] is a method to approximate the relationship between the performance and optimization variables. It can optimize the process parameters within a continuous parameter space, which overcomes Taguchi's limitation of only finding the best set of specified process parameter level combination. The specific procedures of applying the RSM to optimize the process parameters are listed below,

(1) Define the factor levels of each variable, and use the central composite design to construct the experiment design [Myers and Montgomery 1995].

(2) Define the objective function as shown in Eq. (7.24).

$$Obj. = \frac{1}{m}\sum_{e}^{m}\sqrt{\frac{Q_e}{\max(Q_1, Q_2, \dots, Q_m)}}\,|\theta_{se} - \theta_{oe}| \tag{7.24}$$

m is the total sample element number, θ_{se} and θ_{oe} are the fiber orientations of sample element e from the simulation result and the optimized result, respectively. It should be

noted that in Eq. (7.24), there is an additional term to adjust the weight of the absolute orientation difference of each sample element, which will weaken the influence of the sample elements with low EED. Therefore, Eq. (7.24) actually represents the weighted average orientation difference.

(3) Perform the numerical experiments and evaluate the results according to the predefined objective function. The quadratic polynomial function is used to approximate the objective function.

(4) Based on the quadratic relationship, obtain the best parameter set.

7.6 Case study

As shown in Fig. 7.5, the plastic gripper with an outer diameter 68mm will be re-designed with fiber-reinforcement. This gripper is used for fixing rods within pipeline. The reasons for the redesign lie in two points: the current design tends to fail during assembly; and, the ribs as well as the walls are overly thick which brings difficulties to the injection molding process. Therefore, it is necessary to introduce fiber-reinforcement, and modify the current design to be stronger and light-weight.

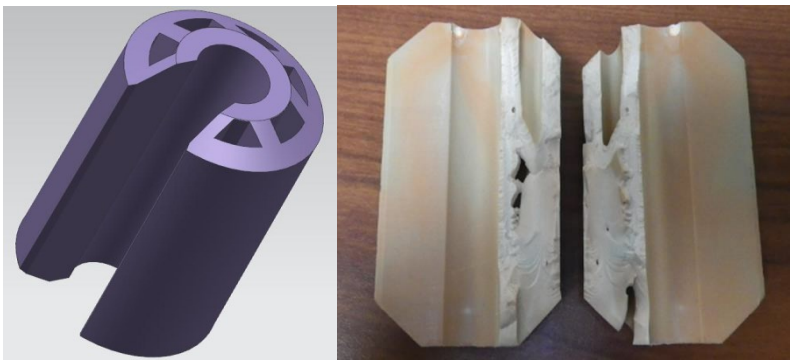

Fig. 7.5 3D model of the gripper and one failure sample

7.6.1 Conceptual design

Before starting the new design, the author would investigate the current design to find out the worst case leading to the failure. It can be determined through qualitative analysis that the

ultimate loading condition occurs when the part bears the largest deformation, which is equivalent to a pair of vertical force imposing on the inner convex corners oppositely, just as shown in Fig. 7.6a. According to the material properties listed in Table 7.1, the maximum allowable von Mises stress is 75MPa. Based on the conditions mentioned above, it can be determined that, the forces and the deformations at the loading points are ±73.25N (per mm in thickness) and ±1.76 mm respectively; the maximum local EED is $4.25*10^{-4}$J, as shown in Fig. 7.6c. It would be special for this case to be used in optimization, as the constant deformations of ±1.76 mm at the loading points should be imposed as the loading condition because of the assembly process.

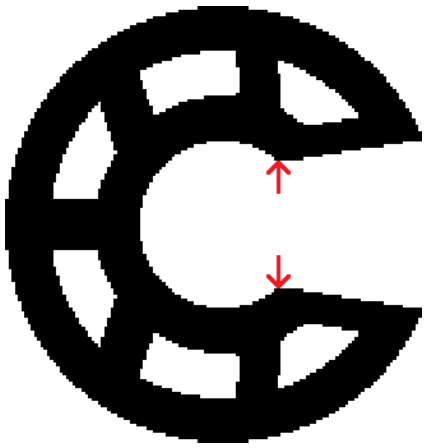

(a) The ultimate loading condition

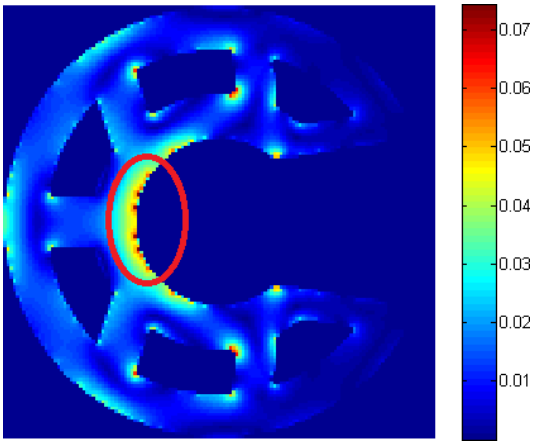

(b) von Mises stress distribution under the ultimate loading condition (GPa)

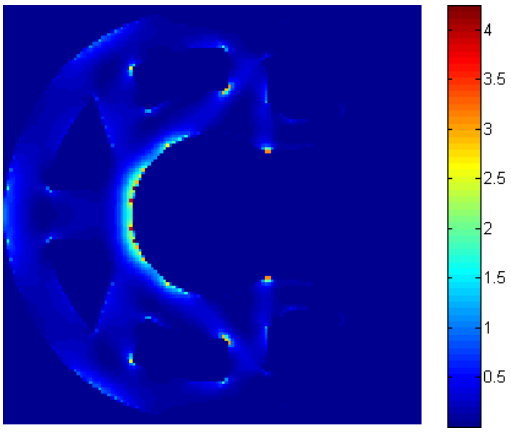

(c) EED distribution under the ultimate loading condition ($*10^{-4}$)

Fig. 7.6 Structural analysis of the current design

Table 7.1 Matrix material properties

Material	Young's modulus	Poisson ratio
Nylon-66	3.4Gpa	0.28
Tensile strength	Safety factor	Maximum allowable von Mises stress
105Mpa	1.4	75Mpa

For the new design, 20 percent glass fibers (in volume) will be introduced. The fiber employs the density of 2.4g/cm^3, Young's modulus and tensile strength along the longitudinal direction of 50GPa and 2.85GPa (including safety factor of 1.4), respectively. With this setup, the maximum local EED should still be constrained within the value of $4.25*10^{-4}$J.

Given the loading condition, optimization with constant deformations as input should be the right scheme, but it will make the conceptual design process even more complex [Niu et al. 2011]; therefore, the assumed loading forces of ±183.13N (per mm in thickness) will be used, which are 2.5 times of the current design. The reasonability of this assumption will be validated later.

The design domain is the gray area as shown in Fig. 7.7a, for which the outer profile will be reserved during the optimization process; thickness of the ribs or walls are intended to be controlled constantly of 5mm instead of the 7mm of the current design.

After proper setup of the problem, we go through the level set geometry and material optimization process and derive the result as shown in Fig. 7.7b; the relevant EED distribution and fiber orientation distribution are shown in Fig. 7.7(c-d), respectively. Table 7.2 presents a data comparison between the current design and the new design, and a few advantages of the new design can be summarized as follows,

- The new design is light-weight, which achieves a material volume save of 11.67 percent;
- The thinner ribs and walls, as well as the bigger space between the ribs make the cooling process design easier and help produce better part quality.

- The majority of the fibers employ the orientations aligning the axial directions of the ribs, which means the fibers are functioning effectively.
- The deformations of the ultimate loading points of the current design are ±1.76mm, while the values of the new design are ±1.74mm. Therefore, it can be concluded that our approximation about the ultimate loading forces for the new design is reasonable.

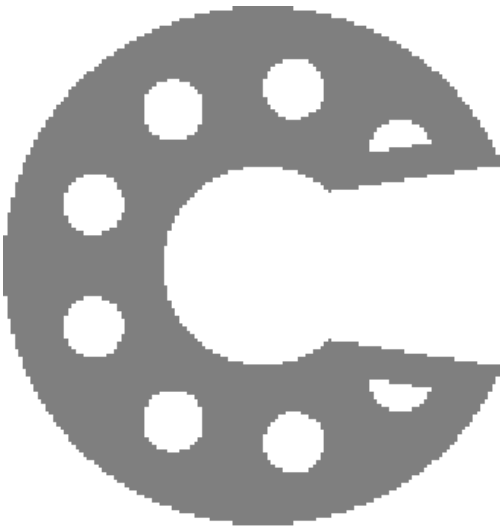

(a) The design domain

(b) Structure

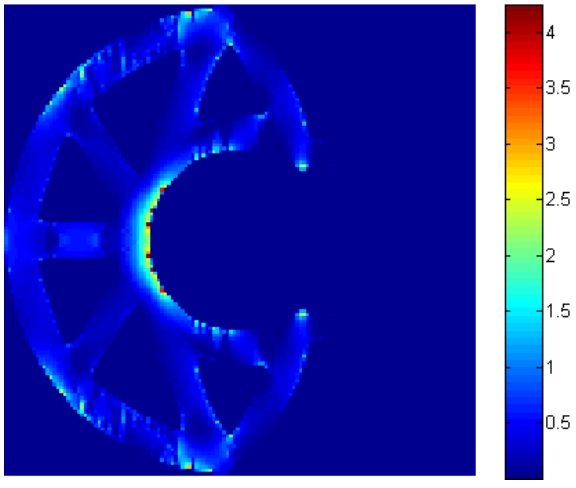

(c) EED distribution under the ultimate loading condition (*10^{-4})

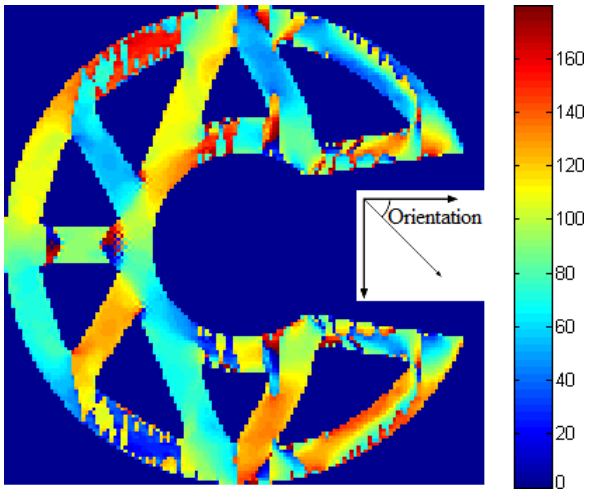

(d) Fiber orientation distribution

Fig. 7.7 The new design

Table 7.2 A comparison between the current design and the new design

	Ultimate loadings (per mm in thickness)	Maximum local EED	Thickness of ribs or walls	Material volume ratio
Current design	±73.25N	$4.25*10^{-4}$J	7mm	0.7969
New design	±183.13N	$4.25*10^{-4}$J	5mm	0.7039

7.6.2 Optimization of the injection molding process

To optimize the injection molding process, each variable has been assigned with three levels as presented in Table 7.3. It should be noted that, the gate location variable means the distance from the left gate to the left end; relatively, the right gate is in a symmetric position.

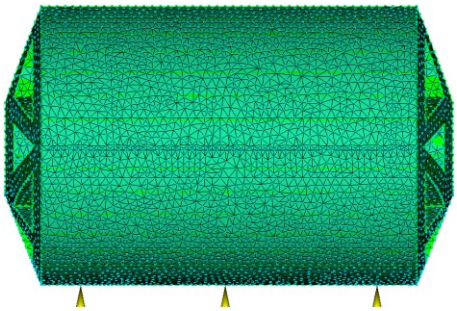

Fig. 7.8 The injection gate distribution

Table 7.3 Levels of optimization variables

	Gate location (cm)	Injection flow rate (cm^3/s)	Mold temperature (℃)	Melt temperature (℃)
-1 level	10	32	60	260
0 level	15	36	90	280
1level	20	40	120	300

Central composite design, as the most popular class of second-order experiment design method, has been applied. The corresponding experiment design is shown in Table 7.4.

Table 7.4 The experiment design and the evaluated objection values

Experiment No.	Gate location x_1	Injection flow rate x_2	Mold temperature x_3	Melt temperature x_4	Evaluated objective value
1	-1	-1	-1	-1	7.57
2	-1	-1	-1	1	7.81
3	-1	-1	1	-1	8.01
4	-1	1	-1	-1	7.68
5	-1	-1	1	1	7.94
6	-1	1	-1	1	7.99
7	-1	1	1	-1	7.90
8	-1	1	1	1	8.10
9	1	-1	-1	-1	8.49
10	1	-1	-1	1	8.63
11	1	-1	1	-1	8.70
12	1	1	-1	-1	8.55
13	1	-1	1	1	8.78
14	1	1	-1	1	8.78
15	1	1	1	-1	8.83
16	1	1	1	1	8.89
17	-1	0	0	0	7.84
18	1	0	0	0	8.68
19	0	-1	0	0	8.66
20	0	1	0	0	8.73
21	0	0	-1	0	8.71
22	0	0	1	0	7.73
23	0	0	0	-1	8.63
24	0	0	0	1	8.73
25	0	0	0	0	8.61

The numerical experiment results are evaluated by the objective function as shown in Eq. (7.24), and the corresponding values are attached in Table 7.4. All numerical experiments are conducted with the commercial software Moldflow®. To avoid errors, all properties of the materials are maintained consistent between the conceptual design and the numerical experiments.

Through single variable analysis, the individual effect of each variable on the weighted average orientation difference has been derived and presented in Fig. 7.9. It can be seen that, the gate location has a major influence on the fiber orientations, followed by the mold temperature; the injection flow rate and melt temperature only have limited influence.

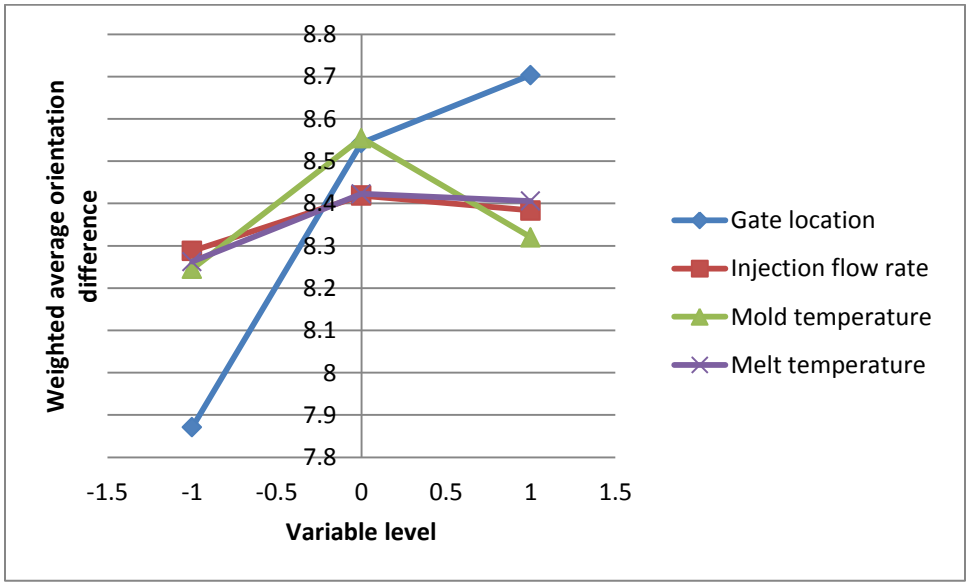

Fig. 7.9 The individual effect of each variable on the weighted average orientation difference

Through regression analysis, the quadratic polynomial function is constructed as,

$$\begin{aligned} Obj. = {} & 8.5215 + 0.4161x_1 + 0.0478x_2 + 0.0372x_3 + 0.0717x_4 \\ & + 0.0069x_1x_2 - 0.0094x_1x_3 - 0.0106x_1x_4 - 0.0131x_2x_3 + 0.0256x_2x_4 \\ & - 0.0406x_3x_4 \\ & - 0.2615{x_1}^2 + 0.1735{x_2}^2 - 0.3015{x_3}^2 + 0.1585\beta_{15}{x_4}^2 \end{aligned} \tag{7.25}$$

Using this quadratic relationship, the best parameter set is obtained as presented in Table 7.5.

Table 7.5 The best parameter set

Gate location (cm)	Injection flow rate (cm^3/s)	Mold temperature (℃)	Melt temperature (℃)	Predicted objective value	Evaluated objective value
10	35.48	60	272.4	7.4692	7.6753

7.6.3 Validation of the final result

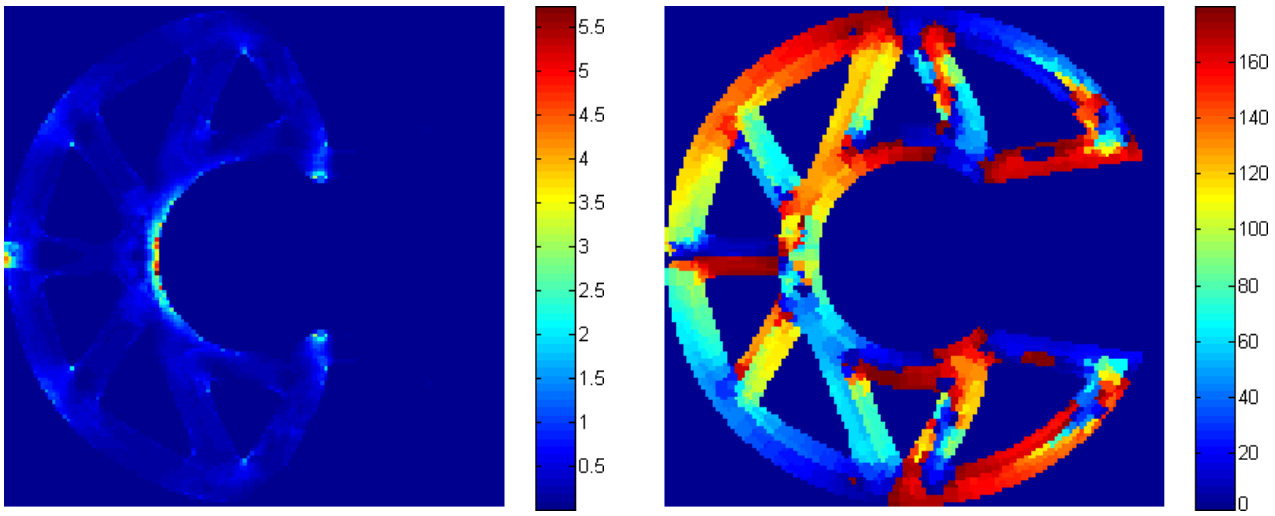

(a) $x_1 = 10$

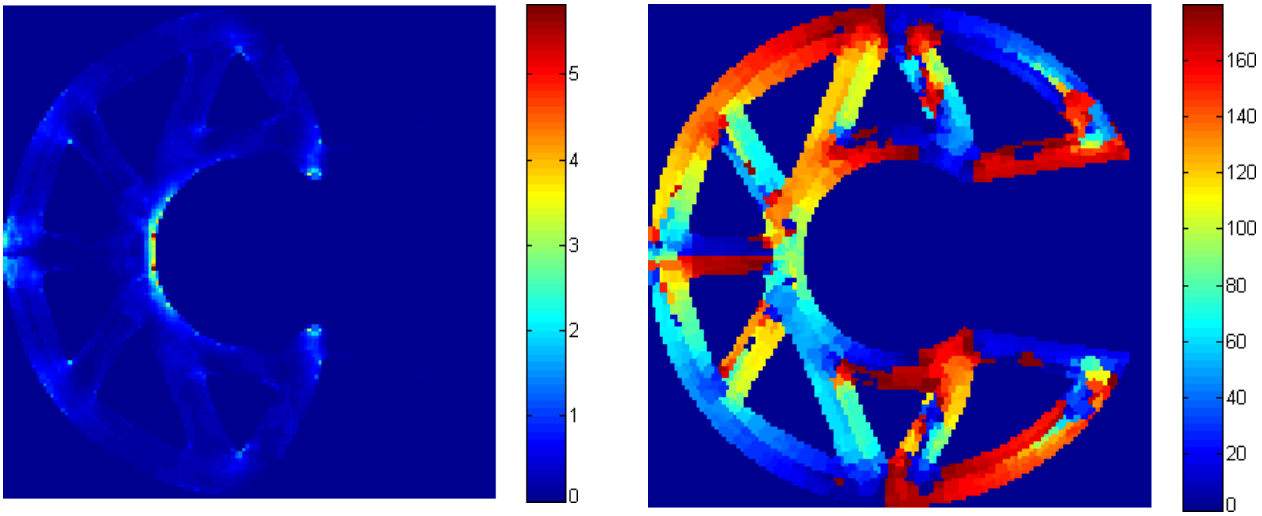

(b) $x_1 = 20$

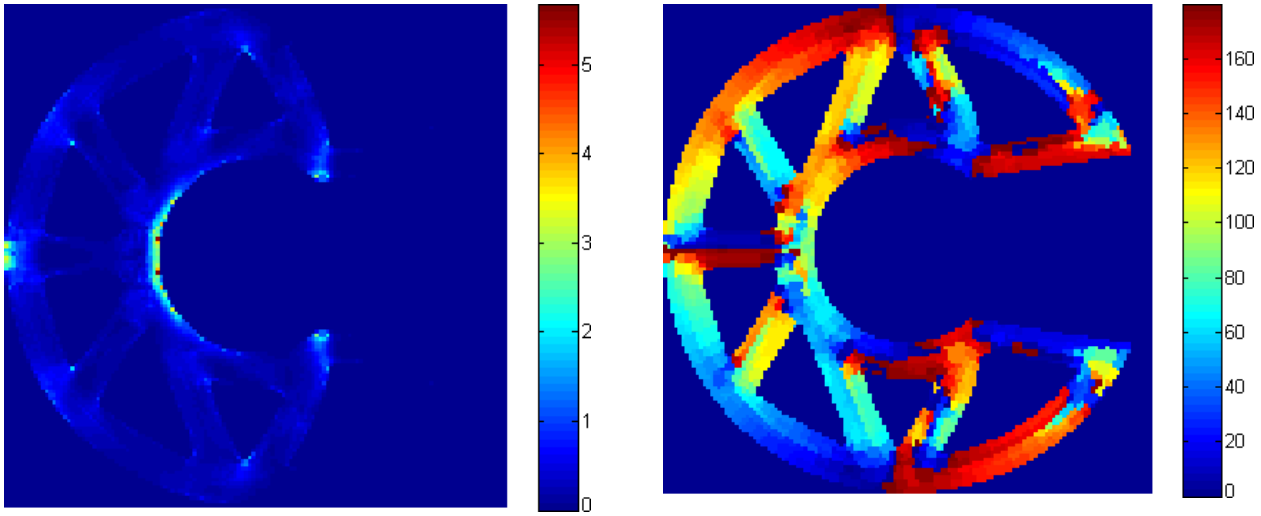
5
4
3
2
1
0
160
140
120
100
80
60
40
20
0

(c) $x_1 = 30$

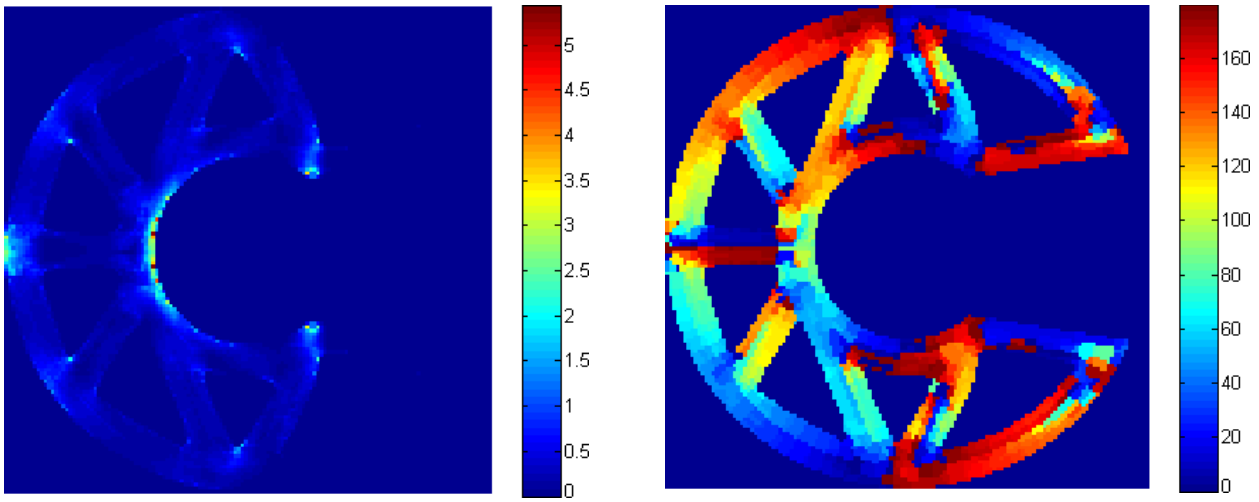
5
4.5
4
3.5
3
2.5
2
1.5
1
0.5
0
160
140
120
100
80
60
40
20
0

(d) $x_1 = 40$

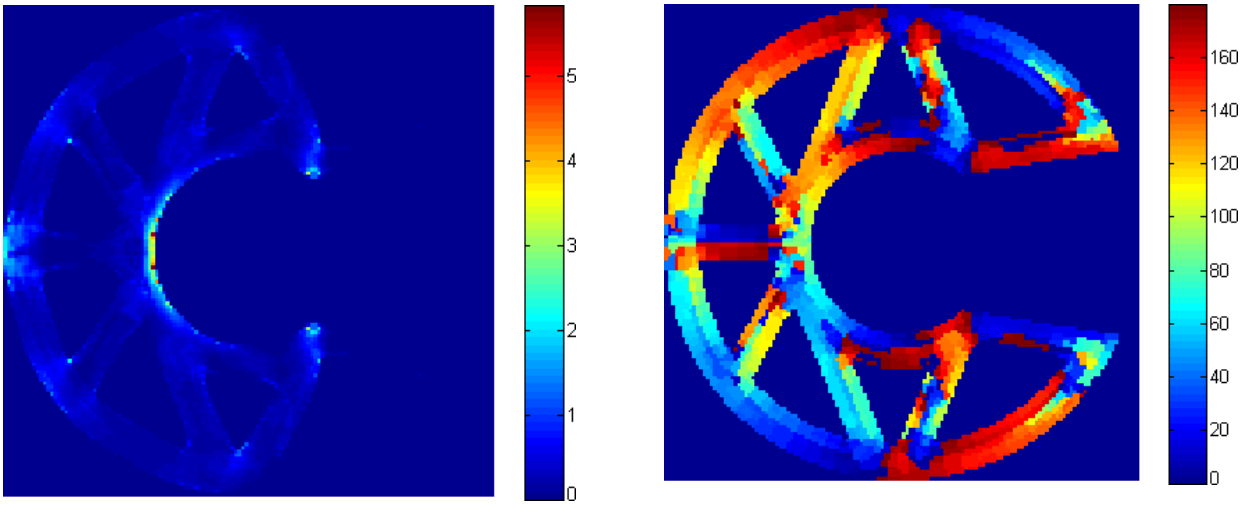

(e) $x_1 = 50$

Fig. 7.10 Sectional strength analysis for simulated best parameter set: the EED (*10^{-4}) and orientation distributions

To validate the result, the authors uniformly extract 5 sections with x_1 equal to 10, 20, 30, 40 and 50, respectively. The strength analysis is conducted separately on each section with the constant deformation input; correspondingly, the EED and orientation (in-plane) distributions are demonstrated in Fig. 7.10. It can be seen that the in-plane fiber orientation distributions are analogous at each section; the maximum EEDs distribute within the range of [5.43*10^{-4}J, 5.81*10^{-4}J], which means the safety factor reduction from 1.4 to a range of [1.197, 1.238] through the sections or effectively 1.197. These phenomena are within the expectation of the authors, and thus acceptable, because the RSM is used to reduce the relaxation of the optimized strength, instead of the complete elimination. Therefore, the safety factor should be selected higher than the recommended value at the CACD stage.

The worst case is also tested, and the safety factor is reduced to the range of [1.050, 1.197] through the sections or effectively 1.050. Therefore, it is proved that the RSM can effectively enhance the part strength by optimizing the injection molding process parameters.

7.7 Conclusion

This chapter contributes a systematic design framework for optimizing fiber-reinforced plastic parts. It addresses several design aspects simultaneously, i.e. geometry modeling, optimal material design, and manufacturing.

As for specific contributions, a summary is given as below:

- A new HO model is proposed to address the highly-irregular material composition distribution;
- A two-scale level set geometry and material optimization method is developed;
- This work optimizes the manufactured fiber orientation distribution through controlling the global process parameters, which is practically very meaningful as fiber reinforcement is increasingly employed in plastic industry.

In summary, this new CACD/CAD/CAE integrated design framework can improve the design and manufacturing of fiber-reinforced plastic parts. For future work, the author will pursue the partial fiber reinforcement design under this systematic design framework.

Chapter 8 Slotted liner design – A novel application to local industry

8.1. Introduction

The primary focus of this work has been on machining and injection molding parts. However, the principles can also be applied in other areas. One such area is the design of slotted liners.

Pipeline is the common device for transporting materials, e.g. water, slurry, oil, and gas. Frequently, openings are manufactured on the pipelines to exchange flows with the environment, and they can be any shapes like slots and holes. Normally, the openings are expected of a dense layout in order to reduce the flow resistance. However, the dense opening layout reduces structure stiffness, and excessive deformation may cause failure of functioning.

A typical application is the slotted liner (see Fig. 8.1), a sand control device applied in Steam Assisted Gravity Drainage (SAGD) wells for thermal heavy oil recovery. The slots opened on the pipeline serve as the flow channel of the injected steam to spread into the ambient soil, or the channel to collect the melted oil. Simultaneously, the spindle-like shape blocks the sands from getting in. On working condition, slotted liner may be imposed of heavy loadings (such as the internal high pressure caused by injected steam, the external force caused by soil collapse, and the torque caused by assembling), with which the slots may severely deform and fail to block the sands or communicate the flows.

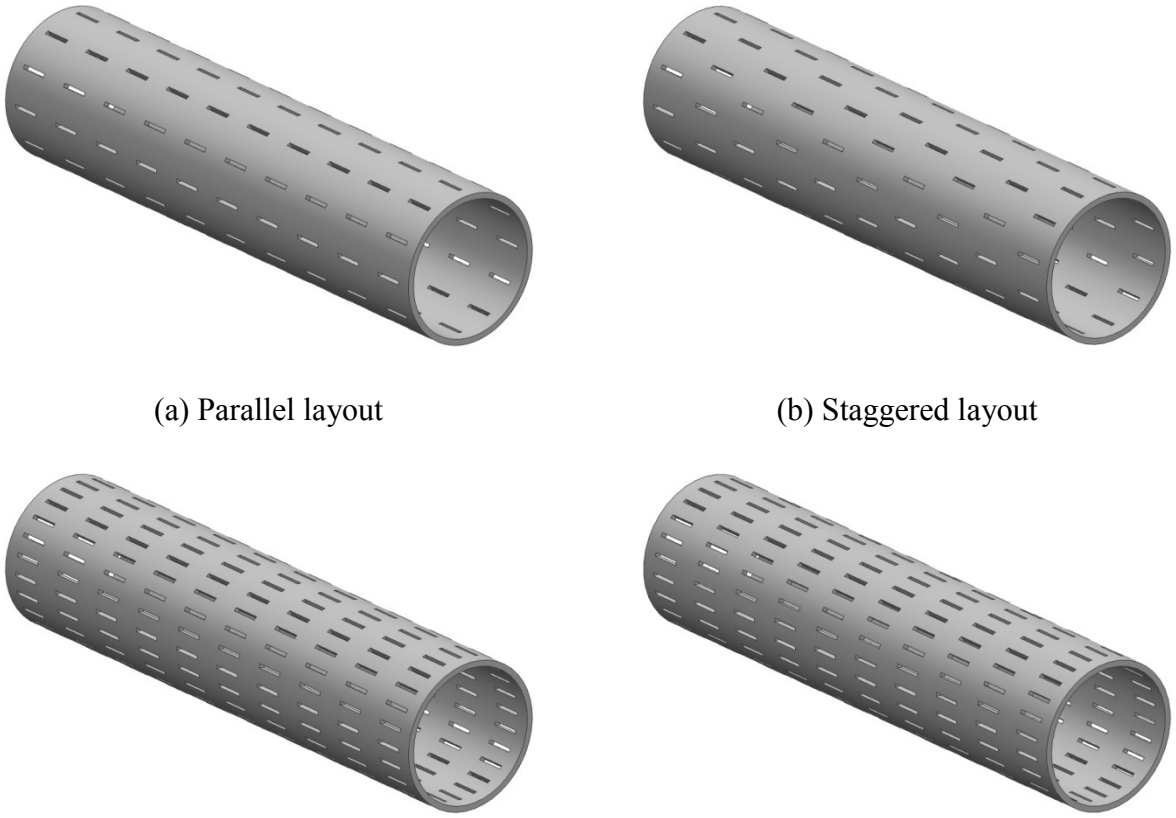

(a) Parallel layout (b) Staggered layout

(c) Dense parallel layout (d) Dense staggered layout

Fig. 8.1 A few types of slotted liner

To make it intuitive, two sets of finite element analysis (FEA) are performed to evaluate the stiffness weakening by adding slots: one is on the raw pipe without slots while the other with full slotted elements. The pipe is loaded as shown in Fig. 8.2c with the two ends fixed. It is meshed into 15*36 elements of equal size 3*1. Each element could either include one longitudinal-direction slot or no opening. To demonstrate the FEA results clearly, the pipeline (Fig. 8.2a) is partitioned into the planar view (Fig. 8.2b) through the axis A-A. Consequently, the FEA results are presented in Fig. 8.2d and 8.2e, respectively. It can be observed that the strain energy densities within the slotted elements are much bigger, which means severer deformations.

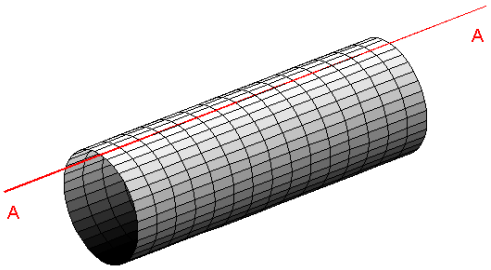

(a) The pipeline

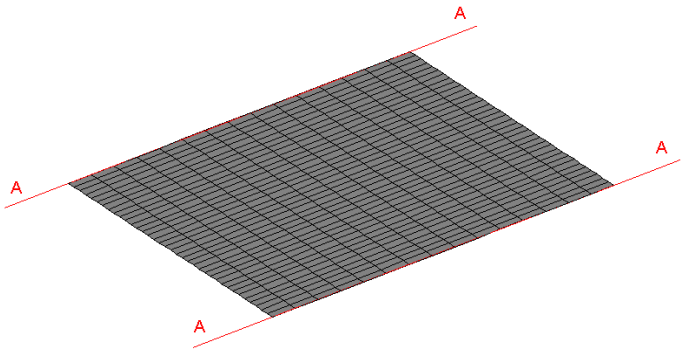

(b) The planar view

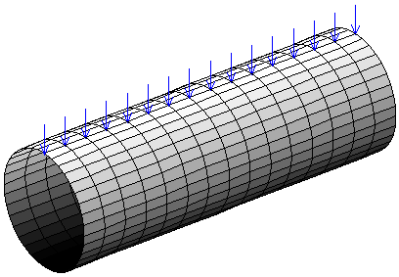

(c) Loading condition

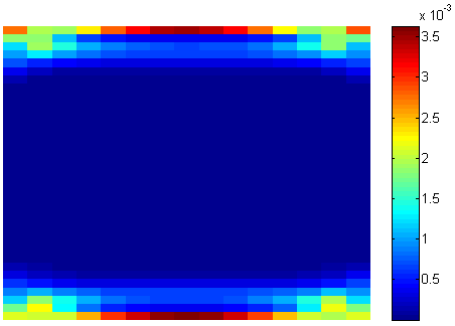

(d) Strain energy distribution without slots

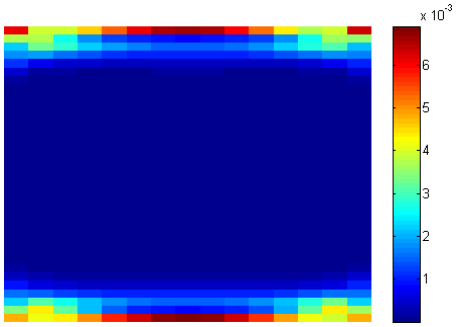

(e) Strain energy distribution with full slots

Fig. 8.2 Finite element analyses on the pipe without and with slots

Given the conflicting design requirements discussed above, designing the pipeline opening layout relying on the trial and error method is extremely tedious and nearly impossible to find the optimum. Additionally, if multiple opening types are applied in one case, the design activity

would be even more complex. Therefore, the following research objectives have been proposed to upgrade the current situation:

- The structural stiffness is to be maximized through optimally placing the openings;
- Minimum opening quantity constraint should be applied for proper functioning;
- The design process should be fully automated for efficiency.

In order to realize these objectives, the author develops a novel design method of the pipeline opening layout, by configuring it into a multi-material level set topology optimization problem. Innovatively, the meshed elements are divided into two categories - with or without openings, and each is treated as one independent material phase. If multiple opening types are involved, they will be treated as different material phases. Homogenization process is implemented on the slotted elements to derive the homogenized elasticity properties. Then, by properly defining the level set functions and configuring the problem formulation, the optimal multi-material distribution could be derived through the solution process.

8.2 General introduction to multi-material level set modeling

To model multiple material phases, it requires multiple level set functions. Generally, there are two schemes: the 'color' level set [Wang and Wang 2004] and the MMLS [Wang et al. 2015].

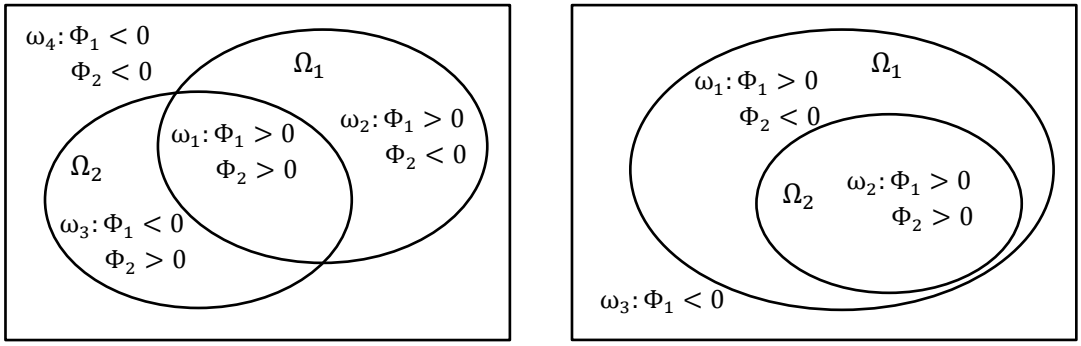

Fig. 8.3 Multi-material level set modeling schemes

The 'color' level set scheme has the characteristic of only requiring m level set functions to represent $n = 2^m$ material phases. As presented in Fig. 8.3a, there are two level set domains: $\Omega_i = \{\boldsymbol{X} \mid \Phi_i(\boldsymbol{X}) > 0\}\ (i = 1, 2)$, four material phases:

$\omega_j = \{\boldsymbol{X} \mid \boldsymbol{H} = \left[H\left(\Phi_1(\boldsymbol{X})\right), H\left(\Phi_2(\boldsymbol{X})\right)\right] = constant\ vector\}$ $(j = 1, 2, 3, 4)$. Taking elasticity tensor for example, the material interpolation is,

$$\begin{aligned}\boldsymbol{D}(\boldsymbol{X}) = {} & H\left(\Phi_1(\boldsymbol{X})\right)H\left(\Phi_2(\boldsymbol{X})\right)\boldsymbol{D}^1 + H\left(\Phi_1(\boldsymbol{X})\right)\left[1 - H\left(\Phi_2(\boldsymbol{X})\right)\right]\boldsymbol{D}^2 \\ & + \left[\boldsymbol{1} - H\left(\Phi_1(\boldsymbol{X})\right)\right]H\left(\Phi_2(\boldsymbol{X})\right)\boldsymbol{D}^3 + \left[\boldsymbol{1} - H\left(\Phi_1(\boldsymbol{X})\right)\right]\left[1 - H\left(\Phi_2(\boldsymbol{X})\right)\right]\boldsymbol{D}^4\end{aligned} \tag{8.1}$$

in which $\boldsymbol{D}^1$, $\boldsymbol{D}^2$, $\boldsymbol{D}^3$, and $\boldsymbol{D}^4$ are the elasticity tensors of material phase 1, 2, 3, and 4, respectively.

The MMLS is relatively a different scheme, which represents $m + 1$ material phases by m level set functions. As presented in Fig. 8.3b, the two level set domains: $\Omega_i = \{\boldsymbol{X} \mid \Phi_i(\boldsymbol{X}) > 0\}$ $(i = 1, 2)$ form three material phases: ω_j $(j = 1, 2, 3)$. And the material interpolation is,

$$\boldsymbol{D}(\boldsymbol{X}) = H\left(\Phi_1(\boldsymbol{X})\right)\left[1 - H\left(\Phi_2(\boldsymbol{X})\right)\right]\boldsymbol{D}^1 + H\left(\Phi_1(\boldsymbol{X})\right)H\left(\Phi_2(\boldsymbol{X})\right)\boldsymbol{D}^2 + \left[1 - H\left(\Phi_1(\boldsymbol{X})\right)\right]\boldsymbol{D}^3 \tag{8.2}$$

By using both modeling schemes, the completeness $D = \bigcup_{k=1}^{n} \omega_k$ and uniqueness $\omega_k \cap \omega_l = \emptyset$ $(k \neq l)$ are satisfied.

In this work, Eq. (8.2) is applied. The two-material and three-material topology optimizations will be investigated, respectively. For two-material scheme, material interpolation of the elasticity tensor is demonstrated in Eq. (8.3).

$$\boldsymbol{D}(\boldsymbol{X}) = H\left(\Phi(\boldsymbol{X})\right)\boldsymbol{D}^1 + \left[1 - H\left(\Phi(\boldsymbol{X})\right)\right]\boldsymbol{D}^2 \tag{8.3}$$

8.3 Homogenization of the shell element with opening

In this section, the shell finite element model is briefly introduced. Based on the classical thin plate theory (often referred to as krichoff's theory), the 4-node shell element is used and the transverse shear stresses τ_{xz} and τ_{yz} are assumed to be zero.

Given a shell element, the strain energy stored is:

$$J = \frac{1}{2}\left[\int_{\Omega} \boldsymbol{D}_s \boldsymbol{e}_s(\widetilde{\boldsymbol{u}})\boldsymbol{e}_s(\widetilde{\boldsymbol{u}})\, d\Omega + \int_{\Omega} \boldsymbol{D}_b \boldsymbol{e}_b(\overline{\boldsymbol{u}})\boldsymbol{e}_b(\overline{\boldsymbol{u}})\, d\Omega\right] \tag{8.4}$$

where $\boldsymbol{D}_s$ and $\boldsymbol{D}_b$ are the elasticity tensors with respect to membrane stress and bending, respectively. $\boldsymbol{e}_s(\widetilde{\boldsymbol{u}})$ and $\boldsymbol{e}_b(\overline{\boldsymbol{u}})$ are the membrane and bending strains. $\widetilde{\boldsymbol{u}}$ is equal to (u, v) which is the in-plane displacement**;** $\overline{\boldsymbol{u}}$ is equal to (w, θ_x, θ_y) in which w is the out-of-plane displacement, (θ_x, θ_y) represents the rotation.

Specifically,

$$\boldsymbol{D}_s = \frac{Eh}{1-v^2}\begin{bmatrix} 1 & v & \\ v & 1 & \\ & & (1-v)/2 \end{bmatrix} \quad \boldsymbol{D}_b = \frac{Eh^3}{12(1-v^2)}\begin{bmatrix} 1 & v & \\ v & 1 & \\ & & (1-v)/2 \end{bmatrix} \tag{8.5}$$

in which $E = 1.3$ is the Young's modulus, $v = 0.3$ is the Poisson's ratio, h is the shell element thickness.

For the sake of simplicity, the strain energy is written into:

$$J = \frac{1}{2}\int_{\Omega} \overline{\boldsymbol{D}}\boldsymbol{e}(\boldsymbol{u})\boldsymbol{e}(\boldsymbol{u})\, d\Omega \tag{8.6}$$

in which,

$$\overline{\boldsymbol{D}} = \begin{bmatrix} \boldsymbol{D}_s & \\ & \boldsymbol{D}_b \end{bmatrix} \quad \boldsymbol{e}(\boldsymbol{u}) = \begin{bmatrix} \boldsymbol{e}_s(\widetilde{\boldsymbol{u}}) \\ \boldsymbol{e}_b(\overline{\boldsymbol{u}}) \end{bmatrix} \quad \boldsymbol{u} = \begin{bmatrix} \widetilde{\boldsymbol{u}} \\ \overline{\boldsymbol{u}} \end{bmatrix} \tag{8.7}$$

Therefore, governing equation of the shell finite element model is:

$$a(\boldsymbol{u}, \boldsymbol{v}) = l(\boldsymbol{v})$$

$$a(\boldsymbol{u}, \boldsymbol{v}) = \int_{\Omega} \overline{\boldsymbol{D}}\boldsymbol{e}(\boldsymbol{u})\boldsymbol{e}(\boldsymbol{v})d\Omega \tag{8.8}$$

$$l(\boldsymbol{v}) = \int_{\Omega} \boldsymbol{p}\boldsymbol{v}d\Omega + \int_{\partial\Omega} \boldsymbol{f}\boldsymbol{v}dS$$

With respect to the slotted element, it is necessary to be homogenized to derive the elasticity properties. As shown in Fig. 8.4, the element is replaced by filling in some weak but homogeneous material. After homogenization, the elasticity tensors are changed into Eq. (8.9),

which demonstrates anisotropic elasticity properties. For homogenization purpose, the slotted element is re-meshed into 30*10 sub-elements, and the slot takes the size of 20*2.

(a) Slotted element (b) Homogenized element

Fig. 8.4 Homogenization of the slotted element

$$\boldsymbol{D}_s^{slot} = h\begin{bmatrix} 1.1362 & 0.1418 & \\ 0.1418 & 0.5030 & \\ & & 0.1122 \end{bmatrix} \quad \boldsymbol{D}_b^{slot} = \frac{h^2}{12}\boldsymbol{D}_s^{slot} \tag{8.9}$$

About the holed element (Fig. 8.5), the same homogenization process is gone through and the homogenized elasticity tensor is presented in Eq. (8.10).

Fig. 8.5 Holed element

$$\boldsymbol{D}_s^{hole} = h\begin{bmatrix} 0.9934 & 0.2789 & \\ 0.2789 & 1.1452 & \\ & & 0.2759 \end{bmatrix} \quad \boldsymbol{D}_b^{hole} = \frac{h^2}{12}\boldsymbol{D}_s^{hole} \tag{8.10}$$

8.4 Multi-material level set topology optimization

8.4.1 Problem formulation

Here, the two-material scheme is considered with the regular and the slotted elements. The energy-minimization problem is defined by Eq. (8.11).

$$Min. \quad J(\boldsymbol{u},\Phi) = \int_D \frac{1}{2}\overline{\boldsymbol{D}}\boldsymbol{e}(\boldsymbol{u})\boldsymbol{e}(\boldsymbol{u})H(\Phi)d\Omega + \int_D \frac{1}{2}\boldsymbol{D}^{slot}\boldsymbol{e}(\boldsymbol{u})\boldsymbol{e}(\boldsymbol{u})[1-H(\Phi)]d\Omega$$

$$s.t. \quad a(\boldsymbol{u},\boldsymbol{v},\Phi) = l(\boldsymbol{v}), \ \ \boldsymbol{v} \in U$$

$$\int_D H(\Phi)d\Omega \le V_{max} \tag{8.11}$$

$$a(\boldsymbol{u},\boldsymbol{v},\Phi) = \int_D \overline{\boldsymbol{D}}\boldsymbol{e}(\boldsymbol{u})\boldsymbol{e}(\boldsymbol{v})H(\Phi)d\Omega + \int_D \boldsymbol{D}^{slot}\boldsymbol{e}(\boldsymbol{u})\boldsymbol{e}(\boldsymbol{v})[1-H(\Phi)]d\Omega$$

$$l(\boldsymbol{v}) = \int_D \boldsymbol{p}\boldsymbol{v}d\Omega + \int_{\partial D} \boldsymbol{\tau}\boldsymbol{v}dS$$

in which, V_{max} is the upper bound of the volume ratio of the regular elements.

8.4.2 Sensitivity analysis

In order to solve the optimization problem, sensitivity analysis is required to calculate the boundary velocity V_n which ensures the material/material interface evolvement in the steepest descent direction. The material derivative and the adjoint method are employed to perform the shape sensitivity analysis.

The Lagrange function is defined as,

$$L = J(\boldsymbol{u},\Phi) + a(\boldsymbol{u},\boldsymbol{w},\Phi) - l(\boldsymbol{w}) + \lambda(\int_D H(\Phi)d\Omega - V_{max}) \tag{8.12}$$

Material derivative of the Lagrange function is given as,

$$L' = J'(\boldsymbol{u},\Phi) + a'(\boldsymbol{u},\boldsymbol{w},\Phi) - l'(\boldsymbol{w}) + \lambda(\int_D H(\Phi)d\Omega)' \tag{8.13}$$

in which,

$$J'(\boldsymbol{u},\Phi)=\int_D \overline{\boldsymbol{D}}\boldsymbol{e}(\boldsymbol{u})\boldsymbol{e}(\boldsymbol{u}')H(\Phi)d\Omega+\frac{1}{2}\int_D \overline{\boldsymbol{D}}\boldsymbol{e}(\boldsymbol{u})\boldsymbol{e}(\boldsymbol{u})\delta(\Phi)V_n|\nabla\Phi|d\Omega$$
$$+\int_D \boldsymbol{D}^{slot}\boldsymbol{e}(\boldsymbol{u})\boldsymbol{e}(\boldsymbol{u}')[1-H(\Phi)]d\Omega \tag{8.14}$$
$$-\frac{1}{2}\int_D \boldsymbol{D}^{slot}\boldsymbol{e}(\boldsymbol{u})\boldsymbol{e}(\boldsymbol{u})\delta(\Phi)V_n|\nabla\Phi|d\Omega$$

$$a'(\boldsymbol{u},\boldsymbol{w},\Phi)=\int_D \overline{\boldsymbol{D}}\boldsymbol{e}(\boldsymbol{u}')\boldsymbol{e}(\boldsymbol{w})H(\Phi)d\Omega+\int_D \overline{\boldsymbol{D}}\boldsymbol{e}(\boldsymbol{u})\boldsymbol{e}(\boldsymbol{w}')H(\Phi)d\Omega$$
$$+\int_D \overline{\boldsymbol{D}}\boldsymbol{e}(\boldsymbol{u})\boldsymbol{e}(\boldsymbol{w})\delta(\Phi)V_n|\nabla\Phi|d\Omega+\int_D \boldsymbol{D}^{slot}\boldsymbol{e}(\boldsymbol{u}')\boldsymbol{e}(\boldsymbol{w})[1-H(\Phi)]d\Omega$$
$$+\int_D \boldsymbol{D}^{slot}\boldsymbol{e}(\boldsymbol{u})\boldsymbol{e}(\boldsymbol{w}')[1-H(\Phi)]d\Omega \tag{8.15}$$
$$-\int_D \boldsymbol{D}^{slot}\boldsymbol{e}(\boldsymbol{u})\boldsymbol{e}(\boldsymbol{w})\delta(\Phi)V_n|\nabla\Phi|d\Omega$$

$$l'(\boldsymbol{w})=\int_D \boldsymbol{p}\boldsymbol{w}'d\Omega+\int_{\partial D}\boldsymbol{\tau}\boldsymbol{w}'dS \tag{8.16}$$

$$\lambda\left(\int_D H(\Phi)d\Omega\right)'=\lambda\int_D \delta(\Phi)V_n|\nabla\Phi|d\Omega \tag{8.17}$$

Put Eq. (8.14-8.17) into Eq. (8.13). Collect all the terms including $\boldsymbol{w}'$, and the sum is shown in Eq. (8.18) which is naturally equal to zero.

$$\int_D \overline{\boldsymbol{D}}\boldsymbol{e}(\boldsymbol{u})\boldsymbol{e}(\boldsymbol{w}')H(\Phi)d\Omega+\int_D \boldsymbol{D}^{slot}\boldsymbol{e}(\boldsymbol{u})\boldsymbol{e}(\boldsymbol{w}')[1-H(\Phi)]d\Omega$$
$$-\int_D \boldsymbol{p}\boldsymbol{w}'d\Omega-\int_{\partial D}\boldsymbol{\tau}\boldsymbol{w}'dS=0 \tag{8.18}$$

Then, collect the terms containing $\boldsymbol{u}'$ and make the sum equal to zero, that is,

$$\int_D \overline{\boldsymbol{D}}\boldsymbol{e}(\boldsymbol{u})\boldsymbol{e}(\boldsymbol{u}')H(\Phi)d\Omega+\int_D \boldsymbol{D}^{slot}\boldsymbol{e}(\boldsymbol{u})\boldsymbol{e}(\boldsymbol{u}')[1-H(\Phi)]d\Omega$$
$$+\int_D \overline{\boldsymbol{D}}\boldsymbol{e}(\boldsymbol{u}')\boldsymbol{e}(\boldsymbol{w})H(\Phi)d\Omega+\int_D \boldsymbol{D}^{slot}\boldsymbol{e}(\boldsymbol{u}')\boldsymbol{e}(\boldsymbol{w})[1-H(\Phi)]d\Omega=0 \tag{8.19}$$

Through solving Eq. (8.19), the solution of the adjoint variable $\boldsymbol{w} = -\boldsymbol{u}$ can be derived. By collecting the remaining, the sensitivity analysis result is obtained as,

$$L' = \int_D R\delta(\Phi)V_n|\nabla\Phi|d\Omega$$
$$R = -\frac{1}{2}\overline{\boldsymbol{D}}\boldsymbol{e}(\boldsymbol{u})\boldsymbol{e}(\boldsymbol{u}) + \frac{1}{2}\boldsymbol{D}^{slot}\boldsymbol{e}(\boldsymbol{u})\boldsymbol{e}(\boldsymbol{u}) + \lambda \tag{8.20}$$

where R is called shape gradient density. Then, by following Eq. (8.21),

$$V_n = -R \tag{8.21}$$

L could be guaranteed to change in the descent direction, as shown in Eq. (8.22),

$$L' = \int_D -R^2\delta(\Phi)|\nabla\Phi|d\Omega \leq 0 \tag{8.22}$$

8.5 Numerical examples

In this section, numerical examples are studied to prove the effectiveness of the multi-material level set topology optimization method. For all these examples, they share the same discretization of being uniformly meshed into 60*36 shell elements with constant element size 3*1, while the boundary conditions are case based.

Augmented Lagrange multiplier is used to address the volume ratio constraint.

It is noticed that all the optimization results are demonstrated in the planar view which is generated following Fig. 8.2.

Case 1. Point load

The first case employs point load as shown in Fig. 8.6a. The left end of the pipe is fixed. Two materials are applied in this case: as shown in Fig. 8.6b, the black color represents the regular elements while the grey color represents the slotted elements. The objective is to minimize the energy stored in the structure under the regular material volume constraint of 30 percent.

Optimization result is demonstrated in Fig. 8.6c. Because the pipeline opening layout normally employs repetition in both longitudinal and circumference directions, a 3*4

(longitudinal*circumference) repetition is applied to the problem setup. Correspondingly, the optimization result is shown in Fig. 8.6d.

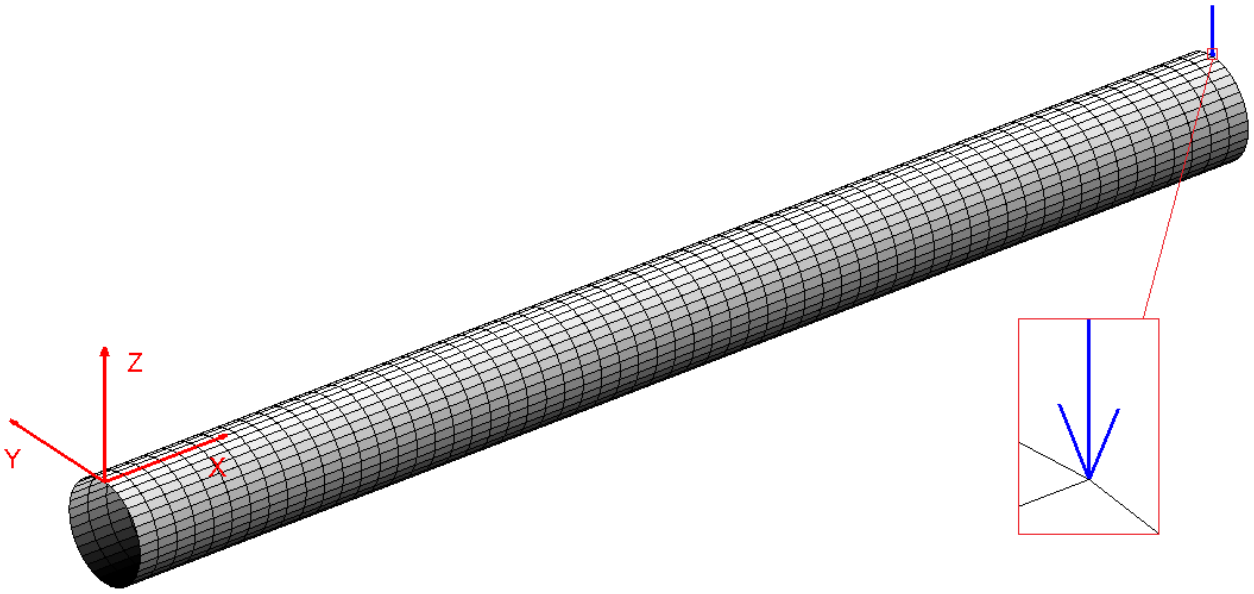

(a) Boundary condition

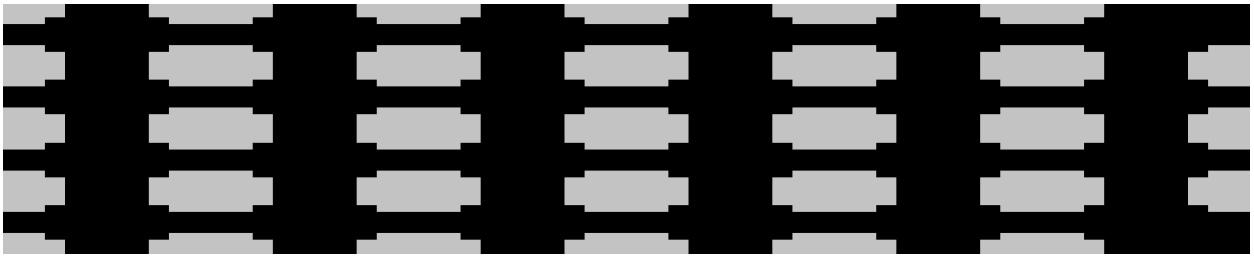

(b) Initial design

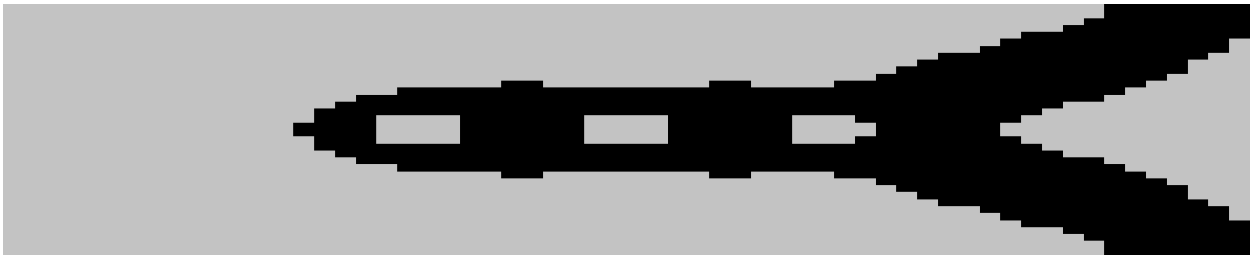

(c) Optimization result without repetition constraint

(d) Optimization result with 3*4 repetition constraint

Fig. 8.6 Topology optimization of the pipeline opening layout under point load

Case 2. Linear load

The second case employs linear load as shown in Fig. 8.7a. Both ends of the pipe are fixed. Again, the two materials are applied. The objective is still to minimize the energy stored in the structure under the regular material volume constraint of 30 percent.

Optimization result is demonstrated in Fig. 8.7c, and the result with 3*4 repetitions is shown in Fig. 8.7d.

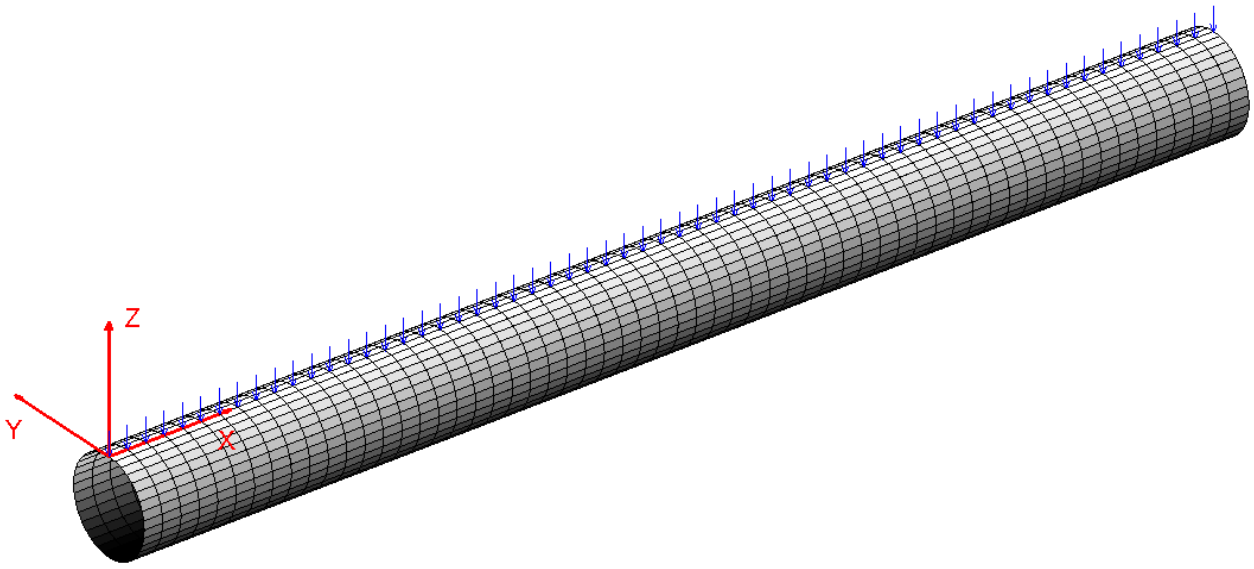

(a) Boundary condition

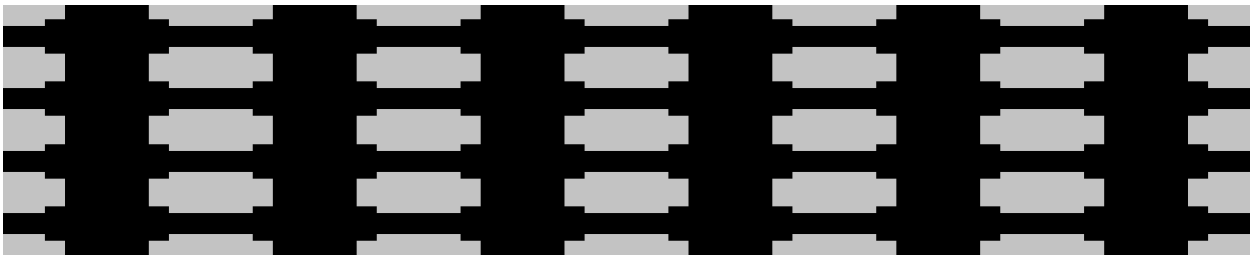

(b) Initial design

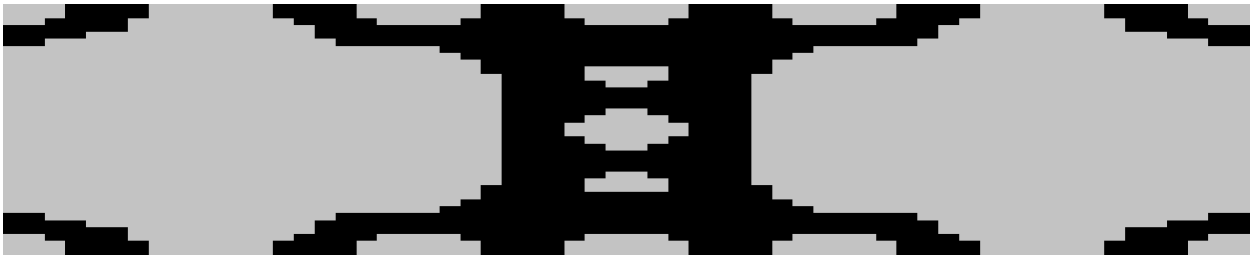

(c) Optimization result without repetition constraint

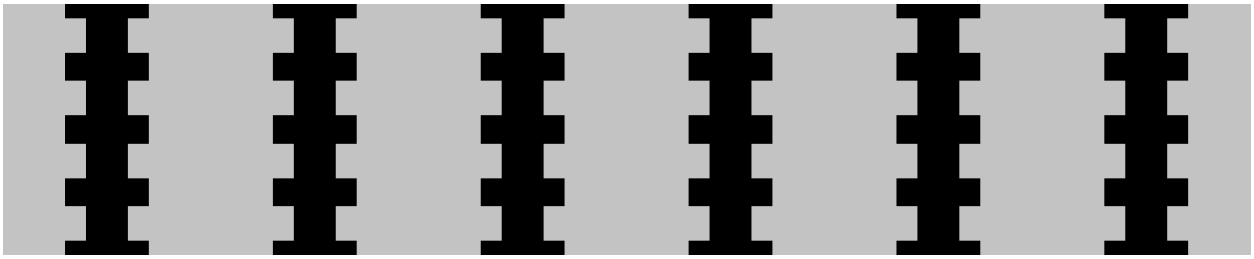

(d) Optimization result with 3*4 repetition constraint

Fig. 8.7 Topology optimization of the pipeline opening layout under linear load

Case 3. Torque load

This case employs the torque load as shown in Fig. 8.8a. The left end of the pipe is fixed. Again, the two materials are applied. The objective and the material volume constraint keep the same as case 2.

Optimization result is demonstrated in Fig. 8.8c, and the result with 3*4 repetitions is shown in Fig. 8.8d.

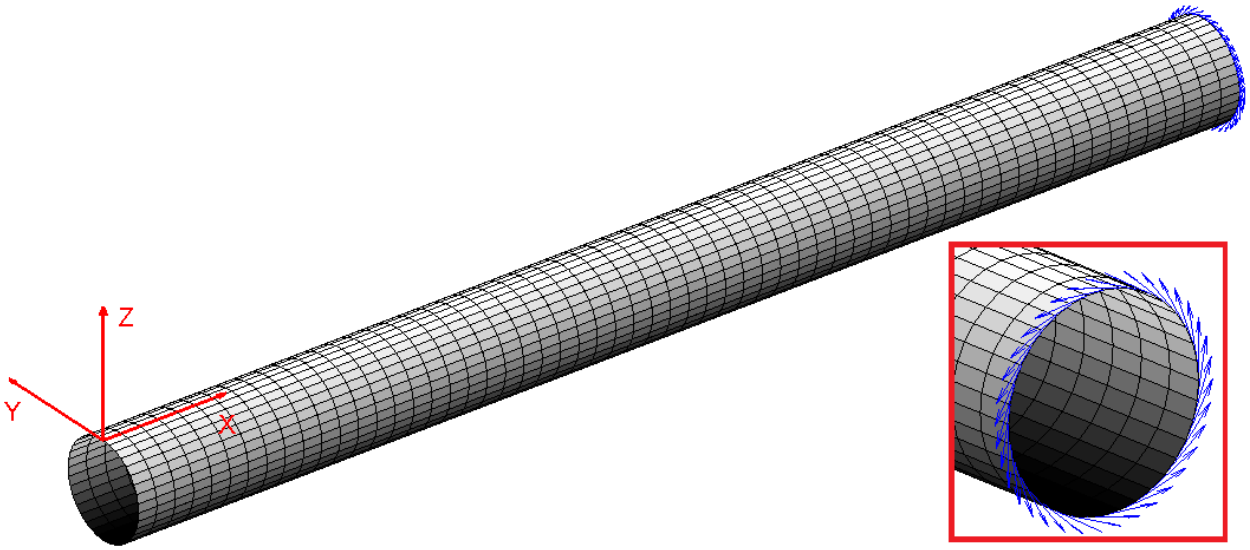

(a) Boundary condition

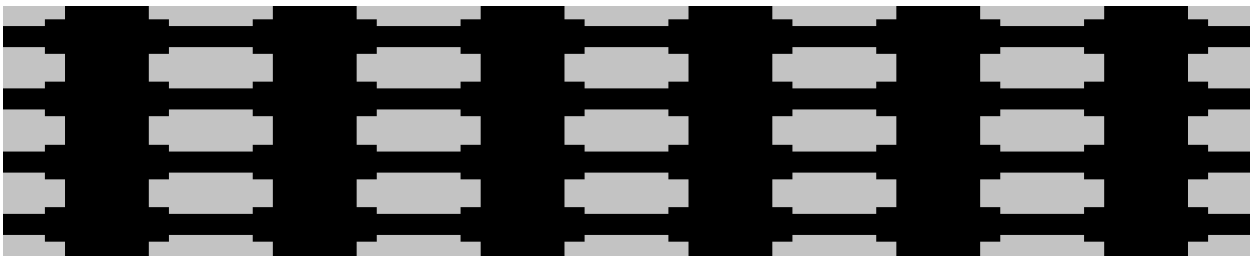

(b) Initial design

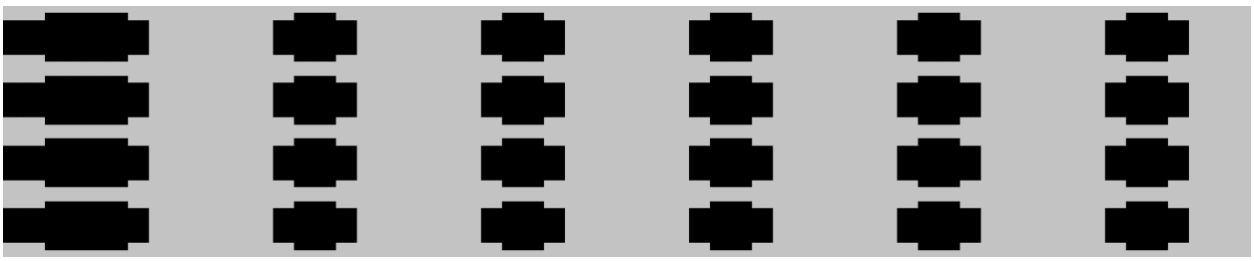

(c) Optimization result without repetition constraint

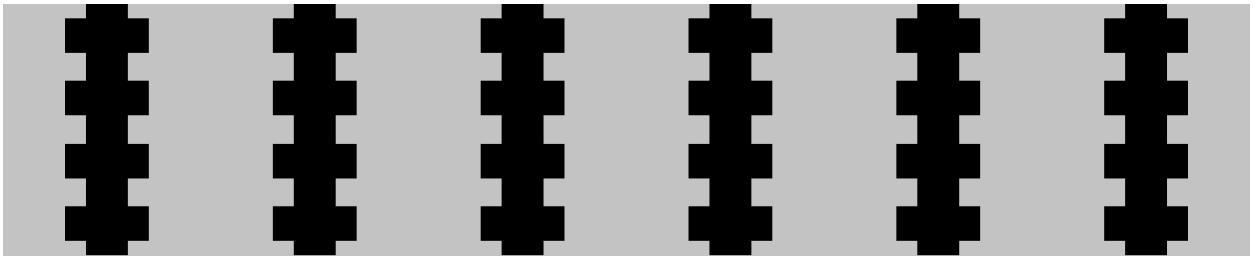

(d) Optimization result with 3*4 repetition constraint

Fig. 8.8 Topology optimization of the pipeline opening layout under torque load

Case 4. Pressure load

This case employs internal pressure load as shown in Fig. 8.9a. Both ends of the pipe are fixed. Again, the two materials are applied. The objective is still to minimize the energy stored in the structure but the regular material volume constraint is set to be 40 percent.

Optimization result is demonstrated in Fig. 8.9c. It can be observed that this result already satisfies the 3*4 repetition requirement. Therefore, the 3*4 repetition constraint is not applied in this case.

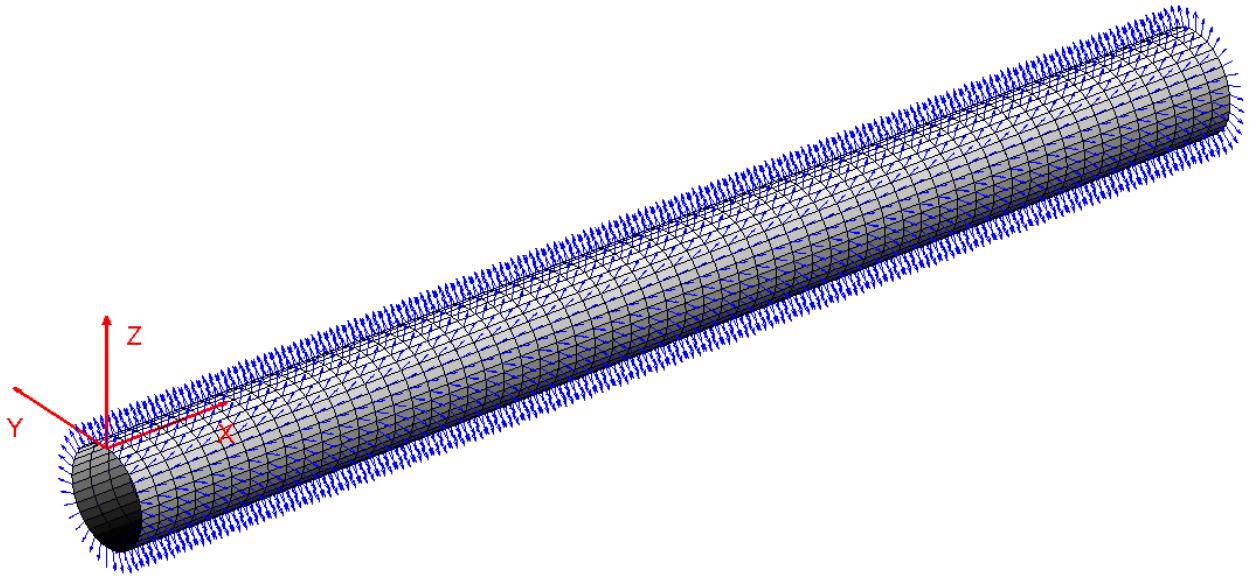

(a) Boundary condition

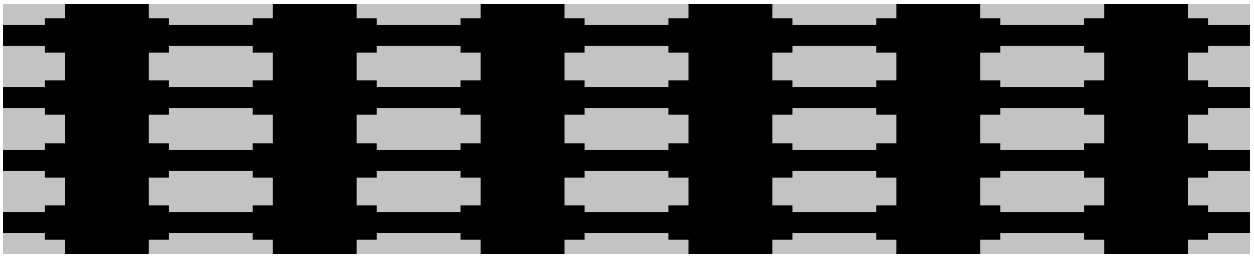

(b) Initial design

(c) Optimization result without repetition constraint

Fig. 8.9 Topology optimization of the pipeline opening layout under pressure load

In summary of the case studies, the relevant data are listed in Table 8.1.

Table 8.1 Data of the optimization results

Case	Energy	Volume ratio	Loading magnitude
Point load without repetition constraint	2.2053	0.300	0.1
Point load with repetition constraint	2.2175	0.300	0.1
Linear load without repetition constraint	3.6964	0.300	0.01/(3 unit distance)
Linear load with repetition constraint	3.9938	0.300	0.01/(3 unit distance)
Torque load without repetition constraint	1.9123	0.300	0.02/circumference distance
Torque load with repetition constraint	1.9129	0.311	0.02/circumference distance
Pressure load without repetition constraint	7.4361	0.400	0.01/(3 unit area)

Case 5. Three material phases

In this case, three material phases are applied: the regular material, the material with slots (see Fig. 8.4), and the material with holes (see Fig. 8.5). The boundary condition in case 2 is applied. The objective is to minimize the energy stored in the structure under volume constraints of 20 percent of the regular material and 30 percent of the material with holes. Eq. (8.2) is applied for

material interpolation and therefore, two level set functions are employed to model three material phases as presented in Eq. (8.23).

$$\boldsymbol{D}(\boldsymbol{X},\Phi_1,\Phi_2) = H\big(\Phi_1(\boldsymbol{X})\big)\big[1-H\big(\Phi_2(\boldsymbol{X})\big)\big]\boldsymbol{D}^{hole} + H\big(\Phi_1(\boldsymbol{X})\big)H\big(\Phi_2(\boldsymbol{X})\big)\boldsymbol{D} + \big[1-H\big(\Phi_1(\boldsymbol{X})\big)\big]\boldsymbol{D}^{slot} \tag{8.23}$$

Optimization result is demonstrated in Fig. 8.10b. Red color represents the material with holes and black color represents the regular material. Convergence history is demonstrated in Fig. 8.11.

It can be observed that: the regular material distribute around loading areas which is reasonable because of its full stiffness; the material with holes mainly distribute across the circumference in the pipeline middle, which is also reasonable because it is relatively stiff in the circumferential direction as presented in Eq. (8.9), especially compared to the material with slots.

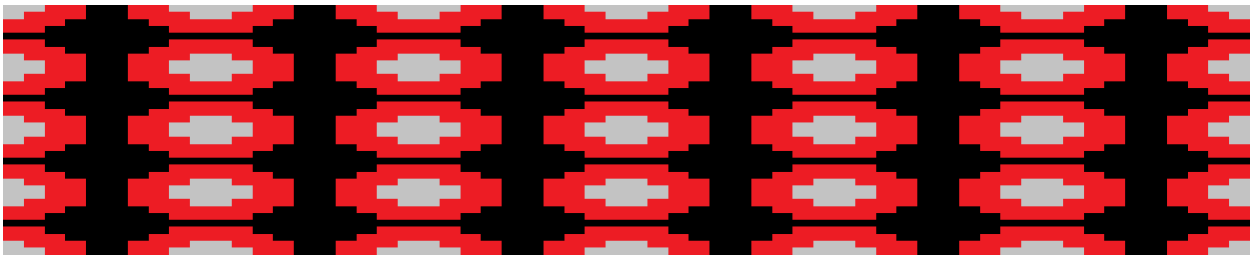

(a) Initial design

(b) Optimization result

Fig. 8.10 Topology optimization of the pipeline opening layout with three material phases (red: material with holes)

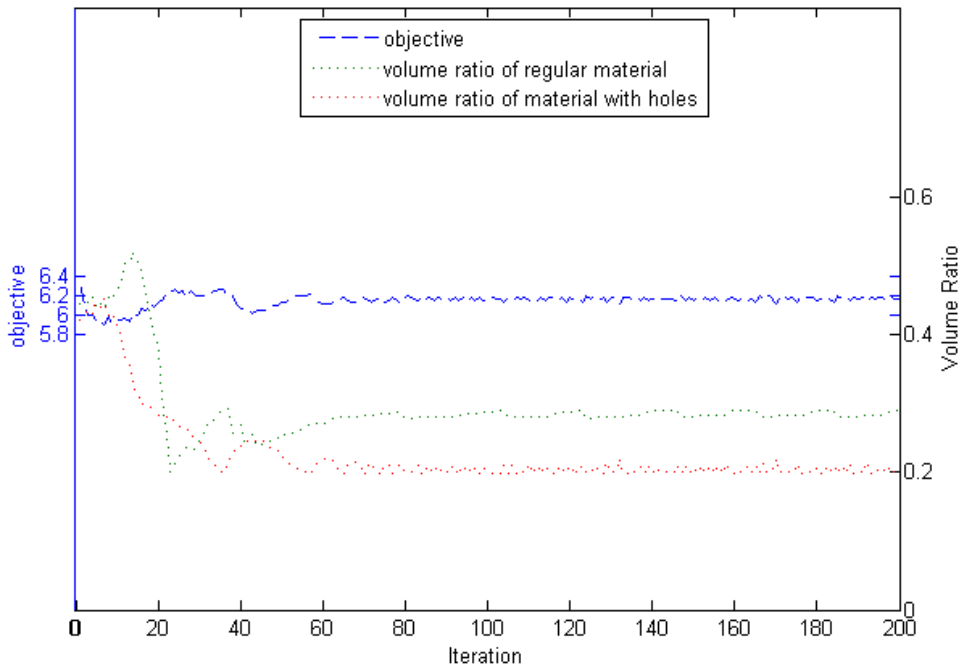

Fig. 8.11 Convergence history

8.6 Conclusion

This Chapter presents a novel application of multi-material level set topology optimization to design the pipeline opening layout. Innovatively, the shell elements are categorized into different types and regarded as distinct material phases, which transform the discrete layout design problem into a continuous multi-material topology optimization problem. The problem is solved by level set method. Effectiveness has been proven by a few case studies.

For future works, orientations of the openings may be designated as optimization variables as well, which could further enhance the structure stiffness without sacrificing the opening quantity. Additionally, fluid flow simulation could be more closely involved to minimize the flow resistance. As widely recognized, it is non-trivial to prove the global optimum for the non-linear optimization problems. Therefore, it would be meaningful to compare the optimized design with some existing designs to prove the improvement.

Chapter 9 Conclusion

Topology optimization has been popular in the structural optimization field for its great design freedom, high design efficiency, and wide applicability. Among the topology optimization methods, level set topology optimization is gaining its unique position because of the clear boundary representation and the diversified level set function definitions. On this basis, this research makes new contributions to the development of level set method, especially for the geometry feature-based methods, the B-rep geometry based method, the OFM methodology, and the two-scale extension. Additionally, this research explores the multidisciplinary application of level set topology optimization in a variety of industrial fields, including machining, injection molding, additive manufacturing, oil recovery, etc. Therefore, this chapter would summarize the contributions in details and propose the future directions.

9.1 Geometry feature-based methods (Chapter 3&4)

Explicit feature-based method only has very limited development, i.e. explicit feature-based input is required to generate explicit feature-based design, because the capability is limited to manipulate the existing feature primitives but not generate new ones. However, it is non-trivial to obtain the explicit feature-based input in practice. Therefore, one objective of this work was to develop a new explicit feature-based method [Liu and Ma 2015], which demonstrates the good characteristics that it is capable of generating new feature primitives, it can handle the scale control, and it is well adaptive to both 2D and 3D schemes.

Then, for implicit feature control, the current situation is that there is only limited control effect realized by complex control functional. Therefore, a new but simple thickness control functional has been developed [Liu et al. 2015] which is easy in implementation and achieves equal or even better control effects.

9.2 B-rep geometry based method (Chapter 5)

A better way to fill the gap between topology optimization and feature-based design is to develop CAD based topology optimization method. Currently, some CAD tools are incorporated with sizing and shape optimization functions but not topology optimization, because there is

isomorphism restriction of B-rep model which would be violated by topology changes. Comparatively, CSG geometry based topology optimization is more popular [Chen et al. 2007, 2008a; Mei et al. 2008; Liu and Ma 2015] for its insensitivity to topology changes [Chen et al. 2008a]. However, CSG model is constructed by implicitly represented feature primitives, which is not widely supported by CAD systems. Therefore, it would be beneficial to develop B-rep geometry based topology optimization method for the integration purpose.

For B-rep geometry based topology optimization, there are several challenging research issues. First, it should enable the generation of new geometric entities, for which topological derivative [Gopalakrishn and Suresh 2008; Robinson et al. 2012] and velocity field regulation [Liu and Ma 2015] are potential methods. Second, scale control is critical. Taking stiff part design for example, allowing smaller voids can always enhance the stiffness but two small details are undesirable from the perspective of manufacturing. Therefore, an appropriate stopping criterion of new geometric entity generation should be set up. Third, the feature modeling history should be properly constructed. The modeling history records the feature modeling operations and the semantic constraints between features (such as the mounting relationship), which is an essential part of the CAD model. Therefore, it should be properly constructed in order to record the design intent and ease the later-stage design change management.

To the author's knowledge, B-rep geometry based topology optimization method was rarely investigated. It has been proven that, the novel B-rep geometry based method works well with all the three requirements satisfied. Even though there is still room for further improvement, the author believes this method to be a convincing contribution.

9.3 OFM scheme (Chapter 6)

The engineering significance of applying feature technology is that, it enables the involvement of downstream engineering requirements in the early design stage by making use of both the geometric and semantic information contained by the engineering features [Ma 2013]. However, the scope of the current feature-based topology optimization methods are limited to manipulating the geometry only, but ignores the underlying semantic information, as revealed by the literature survey. Therefore, the OFM scheme is proposed to fix this problem.

OFM is one of the most promising research directions of topology optimization. Specifically, OFM is an interdisciplinary scheme combining technologies of DFM and topology optimization. It makes full use of the manufacturing related sematic information to drive the topology optimization process, and therefore addresses the manufacturing requirements in the early conceptual design stage. Here, the manufacturing requirements are not limited to ensuring the part manufacturable; instead, manufacturing time and cost, as well as other quantitative evaluations are to be involved in the objective function and constraints. Beneficially, OFM could greatly shorten the cycle time from conceptual design to the ready-for-manufacturing part design.

There are several underlying issues for the OFM scheme. First, geometry feature-based topology optimization methods should be improved as feature technology is the basis of OFM. Second, it is critical to analytically formulate the manufacturing requirements, for which some other technologies may be involved such as the feature-based machining cost estimation. This issue is sometimes challenging, i.e. it is non-trivial to analytically express the machining time and cost of complex topology structure. Third, the optimization algorithm should connect the database to access the available resources like machines and cutting tools, because the resource related parameters are involved in the optimization problem.

9.4 Industrial application (Chapter 7&8)

This research has innovatively applied the level set topology optimization method for part and device design to a variety of industrial fields, including injection molding, machining and the local oil industry. These contributions are significant that, the motivation of topology optimization development is to serve the industry with high-quality engineering design and high design efficiency, and it is expected that topology optimization could be integrated into various engineering fields. As demonstrated in this research, level set topology optimization has been successfully addressed 2.5D machining part design, fiber-reinforced plastic part design, and slotted liner design, which could greatly benefit engineers in these fields.

9.5 Limitations and future work

Even though this research has made progress in several aspects, limitations of the developed methods still exist. For the explicit feature-based level set method, the feature library is simple and there may be efficiency issue for a large-scale feature library. Additionally, the convergence

stability should be improved. For the implicit feature-based level set method, there is still space to improve the control effect, especially for complex 3D problems. For the two-scale extension, optimization of the local material composition is easily trapped at local optimum. And for the slotted liner design, there are still problems about mesh refinement and fluid flow interaction.

In the future work, we will fix the afore-mentioned limitations, and more importantly, the following works will be focused. The first is to accomplish the integration of topology optimization and CAx system. Development of CAD based topology optimization method is very potential, and there is still room for further improvement of the B-rep geometry based method. Second, the development of the OFM scheme is just starting, and only one sample application has been demonstrated. Apparently, OFM is very promising, and it warrants much more investigation to really get matured and hence benefits the design and manufacturing community. Additionally, there are still many technical challenges to be resolved in order to implement topology optimization into day-to-day industry practice.

Reference

Afonso SMB, Sienz J, Belblidia F (2005) Structural optimization strategies for simple and integrally stiffened plates and shells, Engineering Computation 22:429-452.

Allaire G, Dapogny C, Delgado G, Michailidis G (2014a) Multi-phase structural optimization via a level-set method, ESAIM: Control, Optimization, and Calculus of Variations 20:576-611.

Allaire G, Jouve F, Michailidis G (2013) Casting constraints in structural optimization via a level-set method, 10th World Congress on Structural and Multidisciplinary Optimization, Orlando, Florida, USA.

Allaire G, Jouve F, Michailidis G (2014b) Thickness control in structural optimization via a level set method, DOI: http://hal.archives-ouvertes.fr/hal-00985000

Allaire G, Jouve F, Toader AM (2004) Structural optimization using sensitivity analysis and a level-set method, Journal of Computational Physics 194:363–393.

Ansola R, Canales J, Tarrago JA, Rasmussen J (2002) An integrated approach for shape and topology optimization of shell structures, Computers & Structures 80:449-458.

Ansola R, Canales J, Tarrago JA, Rasmussen J (2004) Combined shape and reinforcement layout optimization of shell structures. Structural and Multidisciplinary Optimization 27:219-227

Belblidia F, Bulman S (2002) A hybrid topology optimization algorithm for static and vibrating shell structures, International Journal for Numerical Methods in Engineering 54:835-852.

Belytschko T, Parimi C, Moes N, Sukumar N, Usui S (2003) Structured extended finite element methods for solid defined by implicit surfaces, International Journal for Numerical Methods in Engineering 56:609-635.

Bendsoe MP, Guedes JM, Haber RB, Pedersen P, Taylor JE (1994) An analytical model to predict optimal material properties in the context of optimal structural design, Journal of Applied Mechanics 61:930-937.

Bendsoe MP, Sigmund O (1999) Material interpolation schemes in topology optimization. Arch. Appl. Mech. 69:635-654

Bendsoe MP, Sigmund O (2003) Topology optimization – theory, methods and applications, Springer.

Bi ZM, Wang LH (2010) Advances in 3D data acquisition and processing for industrial applications, Robotics and Computer-Integrated Manufacturing 26:403-413.

Bieterman MB, Sandstrom DR (2003) A curvilinear tool-path method for pocket machining, Journal of Manufacturing Science and Engineering 125:709-715.

Biswas A, Shapiro V, Tsukanov I (2004) Heterogeneous material modeling with distance fields, Computer Aided Geometry Design 21:215-242.

Brighenti R (2005) Fiber distribution optimization in fiber-reinforced composites by a genetic algorithm, Composite Structures 71:1-15.

Brighenti R, Scorza D (2012) A micro-mechanical model for statistically unidirectional and randomly distributed fiber-reinforced solids, Mathematics and Mechanics of Solids 17:876-893.

Bruggi M, Taliercio A (2013) Topology optimization of the fiber-reinforcement retrofitting existing structures, International Journal of Solids and Structures 50:121-136.

Cai SY, Zhang WH, Zhu JH, Gao T (2014) Stress constrained shape and topology optimization with fixed mesh: A B-spline finite cell method combined with level set function, Computer Methods in Applied Mechanics and Engineering 278:361-387.

Chang KH, Tang PS (2001) Integration of design and manufacturing for structural shape optimization, Advances in Engineering Software 32:555-567.

Chen CS, Chen TJ, Chen SC, Chien RD (2011) Optimization of the injection molding process for short-fiber-reinforced composites, Mechanics of Composite Materials 47:357-368.

Chen JQ, Freytag M, Shapiro V (2008a) Shape sensitivity of constructively represented geometric models, Computer Aided Geometry Design 25:470-488.

Chen JQ, Shapiro V, Suresh K, Tsukanov I (2007) Shape optimization with topological changes and parametric control, International Journal for Numerical Methods in Engineering 71:313-346.

Chen SK, Wang MY, Liu AQ (2008b) Shape feature control in structural topology optimization, Computer-Aided Design 40:951-962.

Cheng GD, Mei YL, Wang XM (2006) A feature-based structural topology optimization method, In: IUTAM symposium on topological design optimization of structures, machines and materials, Springer, 137:505-514.

Cho CS, Choi EH, Cho JR, Lim OK (2011) Topology and parameter optimization of a foaming jig reinforcement structure by the response surface method, Computer-Aided Design 43:1707-1716.

Choi KK, Kim NH (2005a) Structural sensitivity analysis and optimization I: Linear systems, Springer.

Choi KK, Kim NH (2005b) Structural sensitivity analysis and optimization II: Nonlinear systems and applications, Springer.

Deaton JD, Grandhi RV (2014) A survey of structural and multidisciplinary continuum topology optimization: post 2000, Structural and Multidisciplinary Optimization 49:1-38.

Deng YB, Liu ZY, Wu JF, Wu YH (2013b) Topology optimization of steady Navier-Stokes flow with body force, Computer Methods in Applied Mechanics and Engineering 255:306-321.

Deng YB, Zhang P, Liu YS, Wu YH, Liu ZY (2013a) Optimization of unsteady incompressible Navier-Stokes flows using variational level set method, International Journal for Numerical Methods in Fluids 71:1475-1493.

Deng YM, Britton GA, Lam YC, Tor SB, Ma YS (2002) Feature-based CAD-CAE integration model for injection moulded product design, International Journal of Production Research 40:3737-3750.

Dunning PD, Kim HA, MullineuxG (2011) Investigation and improvement of sensitivity computation using the area-fraction weighted fixed grid FEM and structural optimization, Finite Element Analysis and Design 47:933-941.

Edke MS, Chang KH (2006) Shape optimization of heavy load carrying components for structural performance and manufacturing cost, Structural and Multidisciplinary Optimization 31:344-354.

Eschenauer HA, Olhoff N (2001) Topology optimization of continuum structures: A review, Applied Mechanics Review 54:331:390.

Facca AG, Kortschot MT, Yan N (2007) Predicting the tensile strength of natural fiber reinforced thermoplastics, Composites Science and Technology 67:2454-2466.

Ferreira RTL, Rodrigues HC, Guedes JM, Hernandes JA (2014) Hierarchical optimization of laminated fiber reinforced composites, Composite Structures 107:246-259.

Fotouh A, Wolodko JD, Lipsett MG (2014) A review of aspects affecting performance and modeling of short-natural-fiber-reinforced polymers under monotonic and cyclic loading conditions, Polymer Composites 36:397-406.

Fu SY, Lauke B (1996) Effects of fiber length and fiber orientation distributions on the tensile strength of short-fiber-reinforced polymers, Composites Science and Technology 56:1179-1190.

Gao T, Zhang WH (2011) A mass constraint formulation for structural topology optimization with multiphase materials, International Journal for Numerical Methods in Engineering 88:774-796.

Garcia-Ruiz MJ, Steven GP (1998) Fixed grid finite elements in elasticity problems, Engineering Computation 16:145-164.

Gerdeen JC, Rorrer RAL (2012) Engineering design with polymers and composites, CRC Press, Boca Raton.

Gero JS (1990) Design prototypes: a knowledge representation schema for design, AI Magazine 11:26-36.

Gersborg AR, Andreasen CS (2011) An explicit parameterization for casting constraints in gradient driven topology optimization, Structural and Multidisciplinary Optimization 44:875-881.

Ghasemi H, Brighenti R, Zhuang XY, Muthu J, Rabczuk T (2014) Optimal fiber content and distribution in fiber-reinforced solids using a reliability and NURBS based sequential optimization approach, Structural and Multidisciplinary Optimization 51:99-112.

Gibiansky LV, Sigmund O (2000) Multiphase composites with extremal bulk modulus. Journal of Mechanics and Physics of Solids 48:461-498.

Gopalakrishnan SH, Suresh K (2008) Feature sensitivity: A generalization of topological sensitivity, Finite Elements in Analysis and Design 44:696-704.

Grindeanu I, Kim NH, Choi KK, Chen JS (2002) CAD-based shape optimization using a meshfree method, Concurrent Engineering 10:55-66.

Gu J, Li GY, Dong Z (2012) Hybrid and adaptive meta-model-based global optimization. Engineering Optimization 44:87-104.

Guest JK (2009a) Topology optimization with multiple phase projection, Computer Methods in Applied Mechanics Engineering 199:123-135.

Guest JK (2009b) Imposing maximum length scale in topology optimization, Structural and Multidisciplinary Optimization 37:463-473.

Guest JK, Prevost JH, Belytschko T (2004) Achieving minimum length scale in topology optimization using nodal design variables and projection functions, International Journal for Numerical Methods in Engineering 61:238-254.

Guest JK, Zhu M (2012) Casting and milling restrictions in topology optimization via projection-based algorithms, Proceedings of the ASME 2012 International Design Engineering Technical Conference & Computers and Information in Engineering Conference, Chicago, IL, USA.

Gujarathi GP, Ma YS (2011) Parametric CAD/CAE integration using a common data model, Journal of Manufacturing systems 30:118-132.

Guo X, Zhang WS, Zhong WL (2014a) Explicit feature control in structural topology optimization via level set method, Computer Methods in Applied Mechanics Engineering 272:354-378.

Guo X, Zhang WS, Zhong WL (2014b) Doing topology optimization explicitly and geometrically – A new moving morphable components based framework, Journal of Applied Mechanics 81:081009-1-12.

Guo X, Zhang WS, Zhong WL (2014c) Stress-related topology optimization of continuum structures involving multi-phase materials, Computer Methods in Applied Mechanics and Engineering 268:632-655.

Gupta SK, Nau DS (1995) Systematic approach to analyzing the manufacturability of machined parts, Computer-Aided Design 27:323-342.

Ha SH, Cho S (2005) Topological shape optimization of heat conduction problems using level set approach, Numerical Heat Transfer Part B 48:67-88.

Hamri O, Leon JC, Giannini F, Falcidieno B (2010) Software environment for CAD/CAE integration, Advances in Engineering Software 41:1211-1222.

Hardee E, Chang KH, Tu J, Choi KK, Grindeanu I, Yu XM (1999) A CAD-based design parameterization for shape optimization of elastic solids, Advances in Engineering Software 30:185-199.

Harzheim L, Graf G (2002) Topshape: An attempt to create design proposals including manufacturing constraints, International Journal of Vehicle Design 28:389-409.

Harzheim L, Graf G (2005) A review of optimization of cast parts using topology optimization. I-Topology optimization without manufacturing constraints, Structural and Multidisciplinary Optimization 30:491-497.

Harzheim L, Graf G (2006) A review of optimization of cast parts using topology optimization. II-Topology optimization with manufacturing constraints, Structural and Multidisciplinary Optimization 31:388-399.

Hassani B, Tavakkoli SM, Ghasemnejad H (2013) Simultaneous shape and topology optimization of shell structures, Structural and Multidisciplinary Optimization 48:221-233.

Hinton MJ, Kaddour AS, Soden PD (2004) Failure criteria in fiber reinforced polymer composites: The world-wide failure exercise, Elsevier, Amsterdam.

Ho HS, Lui BFY, Wang MY (2011) Parametric structural optimization with radial basis functions and partition of unity method, Optimization Methods and Software 26:533-553.

Ho HS, Wang MY, Zhou MD (2013) Parametric structural optimization with dynamic knot RBFs and partition of unity method, Structural and Multidisciplinary Optimization 47:353-365.

Holmberg E, Torstenfelt B, Klarbring A (2013) Stress constrained topology optimization, Structural and Multidisciplinary Optimization 48:33-47.

Hoque ASM, Halder PK, Parvez MS, Szecsi T (2013) Integrated manufacturing features and Desisgn-for-manufacture guidelines for reducing product cost under CAD/CAM environment, Computers & Industrial Engineering 66:988-1003.

Hsu MH, Hsu YL (2005) Interpreting three-dimensional structural topology optimization results, Computers & Structures 83:327-337.

Hughes TJR, Cottrell JA, Bazilevs Y (2005) Isogeometric analysis: CAD, finite elements, NURBS, exact geometry and mesh refinement, Computer Methods in Applied Mechanics and Engineering 194:4135-4195.

Hvejsel CF, Lund E (2011) Material interpolation schemes for unified topology and multi-material optimization, Structural and Multidisciplinary Optimization 43:811-825.

Jackson TR, Liu H, Patrikalakis NM, Sachs EM, Cima MJ (1999) Modeling and designing functionally graded material components for fabrication with local composition control, Materials & Design 20:63-75.

Kang M, Kim G, Eum K, Park MW, Kim JK (2014) A classification of multi-axis features based on manufacturing process, International Journal of Precision Engineering and Manufacturing 15:1255-1263.

Kang Z, Wang YQ (2013) Integrated topology optimization with embedded movable holes based on combined description by material density and level sets, Computer Methods in Applied Mechanics and Engineering 255:1-13.

Kerbrat O, Mognol P, Hascoet JY (2011) A new DFM approach to combine machining and additive manufacturing, Computers in Industry 62:684-692.

Kim H, Garcia MJ, Querin OM, Steven GP (2000) Introduction of fixed grid in evolutionary structural optimization, Engineering Computation 17:427-439.

Kim H, Querin OM, Steven GP, Xie YM (2003) Improving efficiency of evolutionary structural optimization by implementing fixed grid mesh, Structural and Multidisciplinary Optimization 24:441-448.

Kim NH, Chang Y (2005) Eulerian shape design sensitivity analysis and optimization with a fixed grid, Computer Methods in Applied Mechanics and Engineering 194:3291-3314.

Kocvara M, Stingl M, Zowe J (2008) Free material optimization: recent progress, Optimization 57:79-100.

Kou XY, Tan ST (2005) A hierarchical representation for heterogeneous object modeling, Computer-Aided Design 37:307-319.

Kou XY, Tan ST (2007a) A systematic approach for integrated computer aided design and finite element analysis of functionally graded material objects, Materials & Design 28:2549-2565.

Kou XY, Tan ST (2007b) Heterogeneous object modeling: A review, Computer-Aided Design 39:284-301.

Kou XY, Tan ST, Sze WS (2006) Modeling complex heterogeneous objects with non-manifold heterogeneous cells, Computer-Aided Design 38:457-474.

Kumar AV, Padmanabhan S, Burla R (2008) Implicit boundary method for finite element analysis using non-conforming mesh or grid, International Journal of Numerical Methods in Engineering 74:1421-1447.

Kumar V, Burns D, Dutta D, Hoffmann C (1999) A framework for object modeling, Computer-Aided Design 31:541-556.

Le C, Norato J, Bruns T, Ha C, Tortorelli D (2010) Stress based topology optimization for continua, Structural and Multidisciplinary Optimization 41:605-620.

Lee SH (2005) A CAD-CAE integration approach using feature-based multi-resolution and multi-abstraction modeling techniques, Computer-Aided Design 37:941-955.

Lee SJ, Bae JE, Hinton E (2000) Shell topology optimization using the layered artificial material model, International Journal for Numerical Methods in Engineering 47:843-867.

Li Q, Steven GP, Querin OM, Xie YM (1999) Optimization of thin shell structures subjected to thermal loading, Structural Engineering and Mechanics 7:401-412.

Li XP, Zhao GQ, Yang C (2014) Effect of mold temperature on motion behavior of short glass fibers in injection molding process, International Journal of Advanced Manufacturing Technology 73:639-645.

Liu CQ, Li YG, Wang W, Shen WM (2013) A feature-based method for NC machining feature estimation, Robotics and Computer-Integrated Manufacturing 29:8-14.

Liu JK, Ma YS (2015) 3D level-set topology optimization: a machining feature-based approach, Structural and Multidisciplinary Optimization 52:563-582.

Liu JK, Ma YS, Fu JY, Duke K (2015) A novel CACD/CAD/CAE integrated design framework for fiber-reinforced plastic parts, Advances in Engineering Software 87:13-29.

Liu T, Wang ST, Li B, Gao L (2014) A level-set-based topology and shape optimization under geometric constraints, Structural and Multidisciplinary Optimization 50:253-273.

Lu JN, Chen YH (2012) Manufacturable mechanical part design with constrained topology optimization, Journal of Engineering Manufacture 226:1727-1735.

Lund E (2009) Buckling topology optimization of laminated multi-material composite shell structures. Composite Structures 91:158-167.

Lund E, Stegmann J (2005) On structural optimization of composite shell structures using a discrete constitutive parameterization, Wind Energy 8:109-124.

Luo J, Gea HC (1998) A systematic topology optimization approach for optimal stiffener design. Structural Optimization 16:280-288.

Luo JZ, Luo Z, Chen SK, Tong LY, Wang MY (2008a) A new level set method for systematic design of hinge-free compliant mechanisms, Computer Methods in Applied Mechanics Engineering 198:318-331.

Luo YJ, Kang Z (2013) Layout design of reinforced concrete structures using two-material topology optimization with Drucker-Prager yield constraints, Structural and Multidisciplinary Optimization 47:95-110.

Luo Z, Tong LY, Kang Z (2009) A level set method for structural shape and topology optimization using radial basis functions, Computers & Structures 87:425-434.

Luo Z, Wang MY, Wang SY, Wei P (2008b) A level set-based parameterization method for structural shape and topology optimization, International Journal for Numerical Methods in Engineering 76:1-26.

Ma YS, Tong T (2003) Associative feature concept modeling for concurrent engineering integration. Computers in Industry 51:51-71.

Ma YS, Chen G, Thimm G (2008) Paradigm shift: unified and associative feature-based concurrent and collaborative engineering. Journal of Intelligent Manufacturing 19:626-641.

Ma YS (ed.) (2013) Semantic modeling and interoperability in product and process engineering, Springer.

Mei YL, Wang XM (2004) A level set method for structural topology optimization with multi-constraints and multi-materials, Acta Mechanica Sinica 20:507-518.

Mei YL, Wang XM, Cheng GD (2008) A feature-based topological optimization for structure design, Advances in Engineering Software 39:71-87.

Miao HK, Sridharan N, Shah JJ (2002) CAD-CAM integration using machining features, International Journal of Computer Integrated Manufacturing, 15:296-318.

Moes N, Dolbow J, Belytschko T (1999) A finite element method for crack growth without remeshing, International Journal for Numerical Methods in Engineering 46:131-150.

Munk DJ, Vio GA, Steven GP (2015) Topology optimization methods using evolutionary algorithms: a review, Structural and Multidisciplinary Optimization 52:613-631.

Myers RH, Montgomery DC (1995) Response surface methodology: Process and product optimization using designed experiments, Wiley-Interscience, New York.

Niu F, Xu SL, Cheng GD (2011) A general formulation of structural topology optimization for maximizing structural stiffness, Structural and Multidisciplinary Optimization 43:561-572

Nolan DC, Tierney CM, Armstrong CG, Robinson TT (2015) Defining simulation intent, Computer-Aided Design 59:50-63.

O'Driscoll M (2002) Design for manufacture, Journal of Materials Processing Technology 122:318-321.

Osher JA, Fedkiw RP (2003) Level set methods and dynamic implicit surfaces, Springer-Verlag, New York.

Osher S, Sethian JA (1988) Front propagating with curvature-dependent speed: algorithms based on Hamilton–Jacobi formulations, Journal of Computational Physics 79:12–49.

PareTO (2013) User manual, http://www.sciartsoft.com/files/Downloads/PareTO_User_Manual.pdf Accessed July 21st, 2014.

Park HS, Dang XP (2010) Structural optimization based on CAD-CAE integration and metamodeling techniques, Computer-Aided Design 42:889-902.

Park KS, Youn SK (2008) Topology optimization of shell structures using adaptive inner-front (AIF) level set method, Structural and Multidisciplinary Optimization 36:43-58.

Pedersen P, Pedersen NL (2013) On strength design using free material subjected to multiple load cases, Structural and Multidisciplinary Optimization 47:7-17.

Petersson J, Sigmund O (1998) Slope constrained topology optimization, International Journal for Numerical Methods in Engineering 41:1417-1434.

Poulsen TA (2003) A new scheme for imposing a minimum length scale in topology optimization, International Journal for Numerical Methods in Engineering 57:741-760.

Qian XP, Dutta D (2004) Feature-based design for heterogeneous objects, Computer-Aided Design 36:1263-1278.

Rabbani T, van den Heuvel F (2004) Methods for fitting CSG models to point clouds and their comparison, Computer graphics and imaging, Kauai, Hawaii, USA.

Robinson TT, Armstrong CG, Chua HS, Othmer C, Grahs T (2012) Optimizing parameterized CAD geometries using sensitivities based on adjoint functions, Computer Aided Design and Applications 9:253-268.

Rozvany GIN (2001) Aims, scope, methods, history and unified terminology of computer-aided topology optimization in structural mechanics, Structural and Multidisciplinary Optimization 21:90-108.

Rozvany GIN (2009) A critical review of established methods of structural topology optimization, Structural and Multidisciplinary Optimization 37:217-237.

SadAbadi H, Ghasemi M (2007) Effects of some injection molding process parameters on fiber orientation tensor of short glass fiber polystyrene composites, Journal of Reinforced Plastics and Composites 26:1729-1741.

Samanta K, Ozbolat IT, Koc B (2014) Optimized normal and distance matching for heterogeneous object modeling, Computer & Industrial Engineering 69:1-11.

Schevenels M, Lazarov BS, Sigmund O (2011) Robust topology optimization accounting for spatially varying manufacturing errors, Computer Methods in Applied Mechanics Engineering 200:3613-3627.

Schramm U, Zhou M (2006) Recent developments in the commercial implementation of topology optimization. In: IUTAM symposium on topological design optimization of structures, machines and materials, Springer, 137:239-248.

Seo YD, Kim HJ, Youn SK (2010a) Shape optimization and its extension to topological design based on isogeometric analysis, International Journal of Solids and Structures 47:1618-1640.

Seo YD, Kim HJ, Youn SK (2010b) Isogeometric topology optimization using trimmed spline surfaces, Computer Methods in Applied Mechanics and Engineering 199:3270-3296.

Sethian JA, Wiegmann A (2000) Structural boundary design via level set and immersed interface methods, Journal of Computational Physics 163:489-528.

Shah JJ, Mantyla M (1995) Parametric and feature-based CAD/CAM: concepts, techniques, and applications, John Wiley & Sons.

Shapiro V, Tsukanov I (1999) Implicit functions with guaranteed differential properties, Fifth ACM Symposium on Solid Modeling and Applications, Ann Arbor, MI, 258-269.

Shapiro V, Tsukanov I, Grishin A (2011) Geometric issues in computer aided design/computer aided engineering integration, Journal of Computing and Information Science in Engineering 11:021005-1-13.

Shen HY, Fu JZ, Chen ZC, Fan YQ (2010) Generation of offset surface for tool path in NC machining through level set methods, International Journal of Advanced Manufacturing Technology 46:1043-4047.

Shin K-H, Dutta D (2001) Constructive representation of heterogeneous objects, Journal of Computing and Information Science in Engineering 1:205-217.

Shin K-H, Natu H, Dutta D, Mazumder J (2003) A method for the design and fabrication of heterogeneous objects, Materials & Design 24:339-353.

Sigmund O (1997) On the design of compliant mechanisms using topology optimization, Mechanics of Structures and Machines 25:493-524.

Sigmund O (2001) Design of multiphysics actuators using topology optimization – Part 2: two-material structures, Computer Methods in Applied Mechanics and Engineering 190:6605-6627.

Sigmund O (2007) Morphology-based black and white filters for topology optimization, Structural and Multidisciplinary Optimization 33:401-424.

Sigmund O (2009) Manufacturing tolerant topology optimization, Acta Mechanica Sinica 25:277-239.

Sigmund O, Maute K (2013) Topology optimization approaches, Structural and Multidisciplinary Optimization 48:1031-1055.

Sigmund O, Petersson J (1998) Numerical instabilities in topology optimization: A survey on procedures dealing with checkerboards, mesh-dependencies and local minima, Structural Optimization 16:68-75.

Sigmund O, Torquato S (1997) Design of materials with extreme thermal expansion using a three-phase topology optimization method, Journal of Mechanics and Physics of Solids 45:1037-1067.

Siu YK, Tan ST (2002) 'Source-based' heterogeneous solid modeling, Computer-Aided Design 34:41-55.

Srikumaran S, Sivaloganathan S (2005) Proving manufacturability at the design stage using commercial modeling software: through feature mapping and feature accessibility, Computer-Aided Design and Application 2:507-516.

Stegmann J, Lund E (2005) Discrete material optimization of general composite shell structures, International Journal for Numerical Methods in Engineering 62:2009-2027.

Stromberg N (2010) Topology optimization of structures with manufacturing and unilateral contact constraints by minimizing an adjustable compliance-volume product, Structural and Multidisciplinary Optimization 42:341-350.

Sukumar N, Chopp DL, Moes N, Belytschko T (2001) Modeling holes and inclusions by level sets in the extended finite-element method, Computer Methods in Applied Mechanics and Engineering 190:6183-6200.

Talreja R (2014) Assessment of the fundamentals of failure theories for composite materials, Composites Science and Technology 105:190-201.

Thakur A, Banerjee AG, Gupta SK (2009) A survey of CAD model simplification techniques for physics-based simulation applications, Computer-Aided Design 41:65-80.

Thompson WB, Owen JC, de St. Germain HJ, Stark SR, Henderson TC (1999) Feature-based reverse engineering of mechanical parts, IEEE Transactions on Robotics and Automation 15:57-66.

Tzeng CJ, Yang YK, Lin YH, Tsai CH (2012) A study of optimization of injection molding process parameters for SGF and PTFE reinforced PC composites using neural network and response surface methodology, International Journal of Advanced Manufacturing Technology 63:691-704.

Unterweger C, Bruggemann O, Furst C (2014a) Synthetic fibers and thermoplastic short-fiber-reinforced polymers: Properties and characterization, Polymer Composites 35:227-236.

Unterweger C, Bruggemann O, Furst C (2014b) Effects of different fiber on the properties of short-fiber-reinforced polypropylene composites, Composites Science and Technology 103:49-55.

Vaidya A, Yu SH, St Ville H, Nguyen DT, Rajan SD (2006) Multiphysics CAD-based design optimization, Mechanics Based Design of Structures and Machines, 34:157-180.

van Dijk NP, Maute K, Langelaar M, van Keulen F (2013) Level-set methods for structural topology optimization: a review, Structural and Multidisciplinary Optimization 48:437-472.

Van Miegroet L, Duysinx P (2007) Stress concentration minimization of 2D filets using X-FEM and level set description, Structural and Multidisciplinary Optimization 33:425-438.

Verbart A, Langelaar M, Van Dijk N, van Keulen F (2012) Level set based topology optimization with stress constraints and consistent sensitivity analysis, 53rd AIAA/ASME/ASCE/AHS/ASC Structures, Structural Dynamics and Materials Conference, Honolulu, Hawaii.

Vermaak N, Michailidis G, Parry G, Estevez R, Allaire G, Brechet Y (2014) Material interface effects on the topology optimization of multi-phase structures using a level set method, Structural and Multidisciplinary Optimization 50:623-644.

Victoria M, Querin OM, Diaz C, Pascual M (2014) The effects of membrane thickness and asymmetry in the topology optimization of stiffeners for thin-shell structures, Engineering Optimization 46:880-894.

Wall WA, Frenzel MA, Cyron C (2008) Isogeometric structural shape optimization, Computer Methods in Applied Mechanics and Engineering 197:2976-2988.

Wang DH, Hu F, Ma ZY, Wu ZP, Zhang WH (2014) A CAD/CAE integrated framework for structural design optimization using sequential approximation optimization, Advances in Engineering Software 76:56-68.

Wang FW, Lazarov BS, Sigmund O (2011) On projection methods, convergence and robust formulations in topology optimization, Structural and Multidisciplinary Optimization 43:767-784.

Wang J, Gu DX, Yu ZY, Tan CB, Zhou LS (2012) A framework for 3D model reconstruction in reverse engineering, Computer & Industrial Engineering 63:1189-1200.

Wang GG, Dong ZM, Aitchison P (2001) Adaptive response surface method – a global optimization scheme for approximation-based design problems. Engineering Optimization 33:707-734.

Wang MY, Chen SK, Wang XM, Mei YL (2005) Design of multimaterial compliant mechanisms using level-set methods, Journal of Mechanical Design 127:941-956.

Wang MY, Wang XM (2004) 'Color' Level sets: a multi-phase method for structural topology optimization with multiple materials, Computer Methods in Applied Mechanics and Engineering 193:469-496.

Wang MY, Wang XM (2005) A level-set based variational method for design and optimization of heterogeneous objects, Computer-Aided Design 37:321-337.

Wang MY, Wang XM, Guo DM (2003) A level set method for structural topology optimization, Computer Methods in Applied Mechanics and Engineering 192:227–246.

Wang S, Chen NF, Chen C-S, Zhu XX (2009) Finite element-based approach to modeling heterogeneous objects, Finite Elements in Analysis and Design 45:592-596.

Wang SY, Lim KM, Khoo BC, Wang MY (2007) An extended level set method for shape and topology optimization, Journal of Computational Physics 221:395-421.

Wang SY, Wang MY (2006) Radial basis functions and level set method for structural topology optimization, International Journal for Numerical Methods in Engineering 65:2060-2090.

Wang YQ, Luo Z, Kang Z, Zhang N (2015) A multi-material level set-based topology and shape optimization method, Computer Methods in Applied Mechanics and Engineering 283:1570-1586.

Wei P, Wang MY, Xing XH (2010) A study on X-FEM in continuum structural optimization using a level set model, Computer-Aided Design 42:708-719.

Wu XJ, Liu WJ, Wang MY (2008) A CAD modeling system for heterogeneous object, Advances in Engineering Software 39:444-453.

Xia L, Zhu JH, Zhang WH, Breitkopf P (2013) An implicit model for the integrated optimization of component layout and structure topology, Computer Methods in Applied Mechanics and Engineering 257:87-102.

Xia Q, Shi TL, Wang MY (2010b) A level set based method for topology optimization of continuum structures with stress constraint, 6th China-Japan-Korea Joint Symposium on Optimization of Structural and Mechanical Systems, Kyoto, Japan.

Xia Q, Shi TL, Wang MY, Liu SY (2010a) A level set based method for the optimization of cast part, Structural and Multidisciplinary Optimization 41:735-747.

Xia Q, Wang MY (2008) Simultaneous optimization of the material properties and the topology of functionally graded structures, Computer-Aided Design 40:660-675.

Xia ZH, Wang QF, Wang YJ, Chen Y (2015) A CAD/CAE incorporate software framework using a unified representation architecture, Advances in Engineering Software 87:68-85.

Xie YM, Steven GP (1993) A simple evolutionary procedure for structural optimization, Computers & Structures 49:885-896.

Xu D, Ananthasuresh GK (2003) Freeform skeletal shape optimization of compliant mechanism, Journal of Mechanical Design 125:253-261.

Xu SR, Jahn W, Muller JD (2014) CAD-based shape optimization with CFD using a discrete adjoint, International Journal for Numerical Methods in Fluids 74:153-168.

Yamada T, Izui K, Nishiwaki S (2011) A level set-based topology optimization method for maximizing thermal diffusivity in problems including design-dependent effects, Journal of Mechanical Design 133:031011-1-9.

Yang PH, Qian XP (2007) A B-spline-based approach to heterogeneous objects design and analysis, , Computer-Aided Design 39:95-111.

Yashiro S, Okabe T, Matsushima K (2011) A numerical approach for injection molding of short-fiber-reinforced plastics using a particle method, Advanced Composite Materials 20:503-517.

Yoo D-J (2013) Heterogeneous object modeling using radial basis functions, International Journal of Precision Engineering and Manufacturing 14:1133-1140.

Younis A, Dong ZM (2010) Trends, features, and tests of common and recently introduced global optimization methods, Engineering Optimization 42:691-718.

Yu GX, Muller JD, Jones D, Christakopoulos F (2011) CAD-based shape optimization using adjoint sensitivities, Computers & Fluids 46:512-516.

Zhandarov S, Mader E (2005) Characterization of fiber/matrix interface strength: applicability of different tests, approaches and parameters, Composites Science and Technology 65:149-160.

Zhang WS, Zhong WL, Guo X (2014) An explicit length scale control in SIMP-based topology optimization, Computer Methods in Applied Mechanics Engineering 282:71-86.

Zhou HM, Liu ZG, Lu BH (2009) Heterogeneous object modeling based on multi-color distance field, Materials & Design 30:939-946.

Zhou M, Fleury R, Patten S, Stannard N, Mylett D, Gardner S (2011) Topology optimization – practical aspects for industrial applications. 9th world congress on structural and multidisciplinary optimization, Shizuoka, Japan.

Zhou M, Fleury R, Shyy YK, Thomas HL (2002) Progress in topology optimization with manufacturing constratins, Proceedings of 9th AIAA/ISSMO symposium on multidisciplinary analysis and optimization, Atlanta, GA, USA.

Zhou MD, Lazarov BS, Wang FW, Sigmund O (2015) Minimum length scale in topology optimization by geometric constraints, Computer Methods in Applied Mechanics Engineering 293:266-282.

Zhou MD, Wang MY (2013) Engineering feature design for level set based structural optimization, Computer-Aided Design 45:1524-1537.

Zhou SW, Li Q (2008) A variational level set method for the topology optimization of steady-state Navier-Stokes flow, Journal of Computational Physics 227:10178-10195.

Zhuang CG, Xiong ZH, Ding H (2007) A level set method for topology optimization of heat conduction problem under multiple load cases, Computer Methods in Applied Mechanics and Engineering 196:1074-1084.

Zhuang CG, Xiong ZH, Ding H (2010a) Topology optimization of multi-material for the heat conduction problem based on the level set method, Engineering Optimization 42:811-831.

Zhuang CG, Xiong ZH, Ding H (2010b) High speed machining tool path generation for pockets using level sets, International Journal of Production Research 48:5749-5766.

Zuo KT, Chen LP, Zhang YQ, Yang JZ (2006) Manufacturing- and machining-based topology optimization, International Journal of Advanced Manufacturing Technology 27:531-536.